Efficient Random Set Uncertainty Quantification by means of Advanced Sampling Techniques

Thesis submitted in accordance with the requirements of
the University of Liverpool for the degree of Doctor in Philosophy
by

Marco De Angelis (BSc and MSc cum laude, Structural Engineering)

July 2015

Acknowledgements

My first greatest acknowledgements go to my supervisors Michael Beer and Edoardo Patelli. Michael Beer's guidance and support have been crucial to make my work visible on a global scale and for developing key academic partnership. Also, his personality and sense of humour made my doctoral experience rather unique and entertaining. I am very grateful to him.

Edoardo Patelli has been more than just a supervisor, he has given me fraternal support, constant guidance, and has taken me on a fantastic journey to the summit of software development. Long, intense and sometimes heated discussions of sparkling imagination on advanced research topics have made my doctorate very prolific, enjoyable and unique. I am very grateful to him for having taken me on board.

I very much acknowledge Matteo Broggi's help, as his understanding of computational analysis and his programming abilities considerably helped me in gaining familiarity with OpenCossan.

I would like to thank Diego Alvarez, for sharing with me his experience and deep insight on Random Set theory. Without his help and guidance the theoretical background of this work would have certainly been incomplete.

The Engineering and Physical Sciences Research Council (EPSRC) and the Institute for Risk and Uncertainty are also greatly acknowledged for having funded my studies. Over the years, the Institute has been a pole of attraction for many excellent researchers from many different parts of the world, and has provided the perfect ambience for the growth of ideas and collaborations.

I am also very grateful to Adam Mannis, who proof-read and significantly improved the presentation of the manuscript.

My special thanks go to my parents, who have been always on my side sustaining my decisions, despite their sorrow of having me fourteen hundred miles away.

Abstract

In this dissertation, Random Sets and Advanced Sampling techniques are combined for general and efficient uncertainty quantification. Random Sets extend the traditional probabilistic framework, as they also comprise imprecision to account for scarce data, lack of knowledge, vagueness, subjectivity, etc. The general attitude of Random Sets to include different kinds of uncertainty is paid to a very high computational price. In fact, Random Sets requires a min-max convolution for each sample picked by the Monte Carlo method. The speed of the min-max convolution can be sensibly increased when the system response relationship is known in analytical form. However, in a general multidisciplinary design context, the system response is very often treated as a "black box"; thus, the convolution requires the adoption of evolutionary or stochastic algorithms, which need to be deployed for each Monte Carlo sample. Therefore, the availability of very efficient sampling techniques is paramount to allow Random Sets to be applied to engineering problems.

In this dissertation, Advanced Line Sampling methods have been generalised and extended to include Random Sets. Advanced Sampling techniques make the estimation of quantiles on relevant probabilities extremely efficient, by requiring significantly fewer numbers of samples compared to standard Monte Carlo methods. In particular, the Line Sampling method has been enhanced to link well to the Random Set representation. These developments comprise line search, line selection, direction adaptation, and data buffering. The enhanced efficiency of Line Sampling is demonstrated by means of numerical and large scale finite element examples. With the enhanced algorithm, the connection between Line Sampling and the generalised uncertainty model has been possible, both in a Double Loop and in a Random Set approach. The presented computational strategies have been implemented in the open source general purpose software for uncertainty quantification, OpenCossan.

The general reach of the proposed strategy is demonstrated by means of applications to structural reliability of a finite element model, to preventive maintenance, and to the NASA Langley multidisciplinary uncertainty quantification challenge.

Declaration

I hereby confirm that the results presented in this dissertation are from my own work and that I have not presented anyone else's work and that full and appropriate acknowledgements have been given where references have been made to the work of others.

This dissertation has 127 pages, 49 figures, 28 tables and 51610 words.

Marco De Angelis
July 2015

List of Publications

Journal Papers:

1. M. de Angelis, E. Patelli, M. Beer, (2014). "Advanced line sampling for efficient robust reliability analysis." *Structural Safety* 52 (2015): 170-182.

2. E. Patelli, D. Alvarez, M. Broggi, M. de Angelis, (2014). "Uncertainty management in multidisciplinary design of critical safety systems." *Journal of Aerospace Information Systems* (2014): 1-30.

3. M. de Angelis, E. Patelli, M. Beer, (2015). "A forced Monte Carlo simulation strategy for the design of maintenance plans with multiple inspections." *ASCE-ASME Journal of Risk and Uncertainty in Engineering Systems* (accepted).

Conference Papers:

1. M. de Angelis, E. Patelli, and M. Beer (2015). "Robust Design of Inspection Schedules by means of Probability Boxes for Structural Systems Prone to Damage Accumulation." *The annual European Safety and Reliability Conference* (ESREL), September, 2015.

2. M. de Angelis, and E. Patelli, (2015). "Advanced Monte Carlo Simulation for the Robust Design and Maintenance of Fatigue-prone Metallic Components." *23rd Conference on Structural Mechanics in Reactor Technology* (SMIRT23), August, 2015.

3. M. de Angelis, E. Patelli, M. Beer, (2015). "Uncertainty management of safety-critical systems: a solution to the back-propagation problem." Proceedings of the 12th International Conference on Applications of Statistics and Probability in Civil Engineering (ICASP12), Vancouver, Canada, July 12-15.

4. L.A. Comerford, M. de Angelis, A. Mannis, M. Beer, and I.A. Kougioumtzoglou, (2014). "An open approach to educational resource development, with a specific example from structural engineering." 42nd Annual Conference of the European Society for Engineering Education (SEFI).

5. E. Patelli, M. Broggi, M. de Angelis, D. Alvarez, (2014). "An integrated and efficient numerical framework for uncertainty quantification: application to the NASA Langley multidisciplinary Uncertainty Quantification Challenge." doi:10.2514/6.2014-1501, AIAA SciTech 2014, American Institute of Aeronautics and Astronautics.

6. E. Patelli, M. Broggi, M. de Angelis and M. Beer, (2014). "OpenCossan: An Efficient Open Tool for Dealing with Epistemic and Aleatory Uncertainties" Vulnerability, Uncertainty and Risk, doi:10.1061/9780784413609.258, pages 320-329, ASCE.

7. E. Tubaldi, A. Dall'Asta, M. Broggi, E. Patelli and M. De Angelis, (2014). "Reliability-Based Design of Fluid Viscous Damper for Seismic Protection of Building Frames" Vulnerability, Uncertainty and Risk, doi:10.1061/9780784413609.177, pages 320-329, ASCE.

8. M. Beer, M. de Angelis, V. Kreinovich, (2014). "Towards efficient ways of estimating failure probability of mechanical structures under interval uncertainty." Vulnerability, Uncertainty and Risk, doi:10.1061/9780784413609.033, pages 320-329, ASCE.

9. M. de Angelis, E. Patelli, M. Beer, (2014). "Line sampling for assessing structural reliability with imprecise probabilities." Vulnerability, Uncertainty and Risk, doi:10.1061/9780784413609.093, pages 915-924, ASCE.

10. M. de Angelis, E. Patelli, and M. Beer (2014). "A generalized numerical framework of imprecise probability to propagate epistemic uncertainty." In *6th Conference on Reliable Engineering Computing* (REC2014), May, pp. 25-28. 2014.

11. M. de Angelis, S. Gabriele, C. Valente, (2013). "Interval solution and robust validation of uncertain elastic beams." Taylor & Francis Group, London, ISBN 978-1-138-00086-5, ICOSSAR proceedings (2013).

12. M. de Angelis, E. Patelli, M. Beer, (2013). "An efficient strategy for computing interval expectation of risk." Taylor & Francis Group, London, ISBN 978-1-138-00086-5, ICOSSAR proceedings (2013).

13. E. Patelli, M. A. Valdebenito, M. de Angelis, (2013). "On robust maintenance scheduling of fatigue-prone structural systems considering imprecise probability." doi: 10.3303/CET1333181, *Chemical Engineering Transactions.* VOL.33, 2013.

14. E. Patelli and M. de Angelis, (2012). "An open computational framework for reliability based optimization." Civili-Comp Press, Stirlingshire, UK, paper 203,2012. Doi:10.4203/ccp99.203

Contents

Acknowledgements i

Abstract iii

Declaration v

List of Publications vii

List of Figures xiii

List of Tables xv

1 Introduction 1

1.1 Problem statement 1
1.2 Reliability analyses of engineering structures 2
1.2.1 Estimation of reliability by means of Monte Carlo simulation . . 3
1.3 Uncertainties in engineering modelling and design 5
1.4 Modelling of epistemic uncertainty and subjectivity 5
1.4.1 Imprecise probability 6
1.5 Numerical implementation 8
1.6 Structure of thesis 8

2 Introduction to Random Sets 11

2.1 Definition of a Random Set 11
2.2 Random Sets: CDFs, Intervals and Probability Boxes 12
2.2.1 Cumulative Distribution Functions 12
2.2.2 Intervals 13
2.2.3 Probability boxes 13
2.2.3.1 Distribution-free p-boxes 13
2.2.3.2 Parametric p-boxes 14
2.3 Copulas 15
2.4 The Aleatory and Epistemic Spaces 15
2.5 System function as image of a Random Set 16

2.5.1 Propagation of focal elements: the extension principle of random sets . . . 16
2.5.2 Sampling of a Random Set . . . 17
2.5.3 Combination of focal elements . . . 17
2.6 Double Loop and Random Set approaches . . . 18
2.7 Chapter summary . . . 19

3 Enhancing the Efficiency of Line Sampling 21
3.1 Advanced Line Sampling . . . 21
3.1.1 Concept of Line Sampling . . . 21
3.1.2 Adaptive algorithm . . . 23
3.1.3 Adaptation of the important direction . . . 24
3.1.4 Efficiency and accuracy . . . 25
3.2 Chapter summary . . . 27

4 Efficient Double Loop Approach for Reliability Estimation: Application to Finite Element Model 29
4.1 Introduction . . . 29
4.2 Credal Sets and Epistemic Domain . . . 30
4.2.1 Reliability assessment of engineering systems . . . 30
4.2.2 Failure probability for generalized uncertainty models . . . 31
4.2.2.1 Conjugate relationship between lower and upper bounds of probability . . . 31
4.3 Sampling-based estimation of set-valued reliability . . . 32
4.3.1 The global search for lower and upper failure probabilities . . . 32
4.3.1.1 The search in the bounded domain of hyper-parameters $\boldsymbol{\Theta}_h$ . . . 32
4.3.1.2 The search in the bounded domain of structural parameters $\boldsymbol{\Theta}_x$ . . . 34
4.3.2 Applicability of the strategy . . . 35
4.4 Examples and applications . . . 35
4.4.1 Illustrative example . . . 35
4.4.2 Large scale finite element model of a six-storey building . . . 38
4.5 Chapter summary . . . 45

5 Efficient Random Set Propagation by means of Line Sampling 47
5.1 Forward Propagation of Random Sets . . . 47
5.1.1 Propagation of focal elements . . . 48
5.1.2 Efficient Propagation with Line Sampling . . . 49
5.2 Forward propagation example . . . 51
5.2.1 Random Set approach . . . 51

5.2.2 Double Loop approach 53
5.3 Backward propagation of Random Sets 54
5.3.1 Solution to the tracking problem based on K-S test 55
5.3.2 Numerical example 56
5.3.2.1 The Double Loop approach 56
5.3.3 The Random Set approach 58
5.3.3.1 The min-max propagation 59
5.3.3.2 Solution to the back-propagation problem 59
5.3.4 Final classification 61
5.4 Chapter summary 61

6 Forced Monte Carlo Strategy for the Robust Scheduling of Multiple Inspections with Random Sets 63
6.1 Introduction 64
6.1.1 Advantages of the proposed methodology 65
6.2 Optimisation of maintenance costs 65
6.2.1 Costs due to inspections and repair 65
6.2.2 Costs of failure 66
6.2.3 Total costs 67
6.2.4 Formulation of the optimisation problem 67
6.3 Efficient forced Monte Carlo for the estimation of time-variant reliability conditional to inspection 67
6.3.1 Time-variant reliability and failure probability estimation 68
6.3.2 Formulation of the maintenance problem 68
6.3.2.1 Assumptions 69
6.3.2.2 Classification of events and total failure probability . . 70
6.3.3 The direct Monte Carlo approach 71
6.3.3.1 The direct MC approach with one inspection (N=1) . . 71
6.3.3.2 The direct MC approach with multiple inspections (N>1) 71
6.3.4 The forced MC simulation approach 72
6.3.4.1 The forced approach with one inspection (N=1) 74
6.3.4.2 The forced approach with multiple inspections (N>1) . 74
6.3.5 Total and partial probability of repair 75
6.4 Chapter summary 76

7 Robust Scheduling of Multiple Inspections: Application to a Fatigue-prone Metallic Structure 77
7.1 Estimation of total failure probability with one inspection 78
7.2 Design of maintenance strategies with one and two inspections 80
7.3 Optimal inspection schedule without imprecision 81
7.3.1 Definition of uncertainties 81

7.3.2 Definition of constraint and cost function . . . 81
7.3.3 Solution to the constrained optimization with N inspections . . . 83
7.4 Optimal inspection schedule considering imprecision . . . 84
7.4.1 Definition of uncertainties . . . 84
7.4.2 Failure probability sensitivity . . . 85
7.4.3 Definition of constraint and cost function . . . 85
7.4.4 Time variant failure probability . . . 86
7.4.5 Optimal inspection schedule . . . 87
7.5 Chapter summary . . . 88

8 The NASA Langley Multidisciplinary UQ Challenge 89
8.1 Introduction . . . 89
8.2 Proposed approach for uncertainty management and quantification . . . 92
8.2.1 Model updating . . . 92
8.2.1.1 Non-parametric statistic method based on Kolmogorov-Smirnov test . . . 93
8.2.1.2 Bayesian updating in the epistemic space . . . 94
8.2.2 Uncertainty Propagation . . . 97
8.2.2.1 Optimisation in the epistemic space (Double Loop approach) . . . 97
8.2.2.2 Propagation of focal sets (Random Set approach) . . . 98
8.3 Subproblem A . . . 100
8.3.1 Non-parametric statistic method based on the Kolmogorov-Smirnov test . . . 101
8.3.2 Bayesian updating in the epistemic space . . . 103
8.4 Subproblem C . . . 105
8.4.1 Optimisation in the epistemic space (Double Loop approach) . . . 106
8.4.2 Propagation of focal sets (Random Set approach) . . . 108
8.5 Subproblem D . . . 109
8.5.1 Extreme values of J_1 (task D1) . . . 110
8.5.2 Extreme values of J_2 (task D2) . . . 114
8.5.3 Solution of task D3 . . . 115
8.6 Chapter summary . . . 115

9 Conclusions and Recommendations 117
9.1 Concluding remarks and summary . . . 117
9.2 Recommendations . . . 119

List of Tables

3.1 Advanced Line Sampling efficiency tests run on the performance function $g(\boldsymbol{x}) = -\sqrt{x_1^2 + x_2^2} + a$, reference solution is obtained via MC (10^6 samples). 26
3.2 Adaptive Line Sampling efficiency tests run on the performance function $g(\boldsymbol{x}) = -\sqrt{\boldsymbol{x}^T\boldsymbol{x}} + a$. and reference solution obtained via MC (10^6 samples). 26

4.1 Results from case (a), argument optima and associated failure probabilities obtained by means of ALS and Global Optimisation. 36
4.2 Results from case (b), interval failure probability obtained by means of ALS and Global Optimisation. 37
4.3 Precise distribution models for the input structural parameters. 39
4.4 Results of the robust reliability analysis of the multi-storey building using distributional p-boxes, obtained as of lower and upper bounds of the failure probability. 42
4.5 Inputs definition of distributional p-boxes; the relative radius of imprecision for this model is set as $\epsilon = \{0, 0.005, 0.0.01, 0.025, 0.05, 0.075\}$. . . 43
4.6 Inputs definition for intervals and parametric p-boxes; the relative radius of imprecision for this model is set as $\epsilon = \{0, 0.01, 0.015, 0.020, 0.025, 0.03\}$. 44
4.7 Lower and upper failure probability bounds resulting from the reliability analysis 44

5.1 Survival, Plausibililty and Belief regions 50
5.2 Mean values and standard deviations for the definition of the p-box bounds 51
5.3 Results obtained with direct Monte Carlo and Line Sampling for the Random Set forward propagation 52
5.4 Results with a Double Loop approach 54
5.5 Mean values and standard deviations for the definition of the p-box bounds 56
5.6 Failure probability bounds with Line Sampling and corresponding extreme normal distributions 58
5.7 Failure probability bounds and corresponding extreme normal distributions obtained with the non-parametric approach 60

7.1 Mission time and annual frequency 78

7.2 Probability distributions for the input quantities of the structural example 82
7.3 Unit costs used for the structural example 82
7.4 Minimum cost, failure probability and corresponding optimum inspection times 83
7.5 Central values and bounded intervals for the mean and standard deviation of the input p-boxes 84
7.6 Minimum total costs and corresponding candidate optimum as the number of inspections increases for the case $p_F^{\text{thres}=10^{-3}}$ 88

8.1 Aleatory and epistemic components of the input variables p_i. 91
8.2 Reduced uncertainty model using the non-parametric approach ($c = 0.547$) or 25 observations and $c = 0.803$ for 50 observations and the Bayesian inference, respectively. The double dash – means that the method could not reduce the epistemic uncertainty for the referred variable. 105
8.3 Bounds of the statistics J_1 and J_2 for the reduced and improved uncertainty model 109
8.4 Epistemic realisations of p_4 and p_5 leading to the maximum of J_1 . . . 112
8.5 Epistemic realisations of p_1, p_{14}, p_{15} and p_{21} leading to the maximum of J_1 112
8.6 Epistemic realisation that are very likely to produce the maximum of J_1. The realisation has been identified maximizing the probability ν_c. 114

List of Figures

1.1 Thesis outline and chapter organisation 9

2.1 Aleatory and epistemic spaces and propagation through the system function 17
2.2 Sample of a 2-dimensional focal set 18

3.1 Pseudocode of the Adaptive Line Sampling algorithm 24
3.2 Directional change in the (original) state space obtained by means of ALS on the limit state defined by the performance function: $g(\boldsymbol{x}) = -(x_1 + x_2) + d^2\ (1 + a\ \sin(b\ \tan^{-1}(x_1, x_2)))$, where $x_1 \sim N(5, 2^2)$, $x_2 \sim N(2, 2^2)$, $d = 10$, $a = 0.2$ and $b = 20$. 25
3.3 Number of samples required from ALS and LS compared to direct MC (a) for decreasing probability target, and (b) for increasing dimension. Here results from direct MC are obtained fixing the $CoV = 0.01$. 27

4.1 Forward propagation with the Double Loop approach 30
4.2 Cantilever beam subject to point load and thermal gradient 37
4.3 FE-model of the six-storey building. 39
4.4 Values of the 244 coordinates of the initial important direction in SNS. . 40
4.5 Values of the performance function along lines in SNS. Figure (a) shows values of the performance g against the L-2 norm of the standard normal points $||\tilde{\boldsymbol{u}}||$, and Figure (b) shows values of the performance g aginst the distance from the hyperplane c. 40
4.6 (a) Fuzzy parameters $\tilde{p} = \{p_c\ [1 - \epsilon_j,\ 1 + \epsilon_j]\}_{j=1}^{6}$ and (b) fuzzy failure probability obtained as set of results for different levels of imprecision. . 42
4.7 (a) Fuzzy distribution parameters (input) $\tilde{p} = \{p_c\ [1 - \epsilon_j,\ 1 + \epsilon_j]\}_{j=1}^{6}$ and (b) fuzzy failure probability (output) obtained with different levels of imprecision 44

5.1 Forward propagation with the Random Set approach 48
5.2 Realisations in the Aleatory and Standard Normal Space in the survival, plausibility and belief regions 52

5.3 Standard implementation of Line sampling operating in a transformed aleatory Standard Normal Space, superimposed to 5000 focal sets obtained with Monte Carlo 53
5.4 Failure probability values with Line Sampling fixing the mean value μ_y to $\mu_y = -1.5$ (a) and to $\mu_y = -1$ (b) 54
5.5 Bounding normal CDFs for x (a), bounding normal CDFs for y (b). . . . 56
5.6 Limit state surface and box of mean values 57
5.7 Failure probability values with Line Sampling fixing the mean value μ_y to $\mu_y = -2$ (a) and to $\mu_y = -0.5$ (b) 57
5.8 Extreme realisations for the failure probability upper bound corresponding to Table 5.6 (Double Loop approach) and collected argument minima (Random Set approach) 60
5.9 Extreme distributions for the failure probability upper bound obtained by fitting normal distributions to the collected minima 61

6.1 Pseudocode for the failure probability estimator of Eq. (6.22), case with N=1 72
6.2 Pseudocode for the failure probability estimator of Eq. (6.22), for the case of multiple inspections (N>1). 73

7.1 Illustration of structural detail and crack 78
7.2 Diagram for the calculation of weights and failure probability conditional to the outcome of one inspection 79
7.3 Tree chart for the calculation of the failure probability conditional to the outcome of one inspection 79
7.4 Curves of costs with one inspection (N=1) 80
7.5 Total costs surface with two inspections (N=2) 81
7.6 Repair cost surface with two inspections (N=2) 82
7.7 Global sensitivity on the failure probability is obtained pinching one input at a time 86
7.8 Upper and lower bounds define the set of possible states and candidate solutions 86
7.9 Failure probability curves obtained performing 0, 2, 5 and 7 inspections with fixed quality 87

8.1 Relationship between the variables and functions of the NASA Langley multidisciplinary uncertainty quantification challenge problem [45]. . . . 90
8.2 Empirical CDF, $\hat{F}$, of the two set of observation points and CDF obtained adopting the Gaussian kernel density of Eq. (8.4), $\tilde{F}$. The dots and squares show the two datasets $\mathcal{D}_e$, respectively. 100

8.3 Histogram of the measure of similarity, D_i, between the CDF calculated sampling randomly in the epistemic space and the observations, for 25 (top panel) and 50 (bottom panel) observations ($\mathcal{D}_e$) 101
8.4 Parallel coordinates plot of the 8 category II and III parameters of the input factors of h_1 (i.e. $p_i, i = 1, \cdots, 5$) for 25 (top panel) and 50 (bottom panel) observations ($\mathcal{D}_e$) 103
8.6 P-boxes of x_1 and the empirical CDFs of the experimental data. The p-boxes have been obtained using the full range of the posterior parameters and using the range that excludes the outliers, respectively. 105
8.5 Normalised histogram of $p(\boldsymbol{\theta}|\mathcal{D}_e)$ obtained using Approximate Bayesian Computational method with (a) 25 experimental observations and (b) 50 experimental observations (b) of x_1, respectively. The normalization assigns a value of 1 to the bin with the highest number of counts. The red line represent the cut-off value to determine the updated range. . . . 106
8.7 Effect of the number of samples generated in the aleatory space for the inner loop estimation of J_1 and J_2. 107
8.8 Convergence of the objective function, w, to the *minimum* and *maximum* for a representative focal element. Genetic Algorithms have been used with a population of 1000 individuals converging after 53 iterations. 109
8.9 Analysis of the performance function $\boldsymbol{g}$ with respect to the output of the subdisciplines, $\boldsymbol{x}$. In the plot the ranges of $x_{i=1:5}$ leading to large positive values of $g_{i=1:8}$ are shown using coloured bars. Grey bars (and dashed lines) indicate variables that are not important for the maximum of the corresponding performance g_i) 110
8.10 Parallel coordinates of $x_{i=1:5}$ leading to the outliers of w. The plot shows also the bounds of the variables $x_{i=1:5}$ identified for the improved uncertainty model. 111
8.11 Parallel coordinates of the inputs $p_{i=1:21}$ leading to values of $w > 1000$ and $J_1 > 1.0$. The y-axis has been normalised between the lower and upper bound of the inputs $p_{i=1:3,6:21}$. p_4 while p_5 have been normalised to the interval $[-5,\ 5]$. 111
8.12 P-box representation of parameter p_1 . The grey area shows the range of p_1 that produces critical values of $\boldsymbol{x}$ and in turn large values of w 113
8.13 P-box representation of parameter p_{21}, respectively. The grey area shows the range of $p_2 1$ that produces critical values of $\boldsymbol{x}$ and in turn large values of w 113
8.14 Extreme case analysis of J_1: parallel plot of the epistemic parameters. The y-axis represents normalised values of the epistemic variables. . . . 114

8.15 Extreme case analysis of J_2: parallel plot of the epistemic parameters. The y-axis represents normalised values of the epistemic variables. . . . 115
8.16 Evolution of the objective function g_5 and search variables x_i 116

Chapter 1

Introduction

"[...] In order to progress we must recognize our ignorance and leave room for doubt. Scientific knowledge is a body of statements of varying degrees of certainty, some most unsure, some nearly sure, but none absolutely certain."

Richard Feynman, 1918-1988

1.1 Problem statement

Complex engineering systems, such as aircraft, offshore platforms, bridges and nuclear power plants, are designed to meet specific requirements and operate in safety for their entire lifetime; thus, they must be able to deal with changes of loads and conditions. For example, aerospace, automotive or structural engineering systems often involve the development of new vehicles, constructions and devices that must be designed to function in harsh domains involving a diverse range of operating conditions.

Engineering problems are formulated and solved using a set of physical and extended probabilistic models, that are mathematical idealisation of reality. The construction of these models involves a significant amount of subjectivity, which leads to separate the aleatory from the epistemic uncertainty. Aleatory uncertainty (from Latin *alea*, rolling of dice), also called variability, refers to the intrinsic randomness of a natural phenomenon, which cannot be reduced by acquiring more data, and is described using probabilistic models. Epistemic uncertainty (from Greek *episteme*, knowledge), or simply uncertainty, refers to the lack of knowledge or data, originating from the fact that it is not possible to perfectly model or predict real world situations due to scarce and limited data; although, this kind of uncertainty can be reduced, better characterised and quantified using available information.

In multidisciplinary design of complex systems, ignoring the effect of uncertainty is unacceptable, as it may lead to catastrophic consequences. In addition, safety-critical systems involve high-consequence decisions often made on the basis of quantitative data that is very scarce or prohibitively expensive to collect. Despite the availability of

detailed high fidelity physical models, analysts still need to make clear decisions based on available information. Thus, they must be able to trust the methodology adopted to analyse the system, in order to quantify the risk with the available level of information, and so avoid wrong decisions due to artificial restrictions introduced at the modelling stage. Comprehensive modelling of uncertainty that accounts for imprecision, provides new insight into engineering problems, for example, helping to identify robust optimal solutions and decisions.

Risk is conventionally understood as the product between the failure probability of the system and the expected loss (or consequence) caused by the system failure. While the expected loss is quantified in monetary units, the failure probability is calculated, by means of reliability methods, within a rigorous mathematical framework. Commonly, this requires the specification of precise distribution models (of probability), including dependencies for the input variables.

The uncertainty management requires the uncertainty to be propagated, quantified and the risk to be assessed and subsequently minimised. Engineering models are often quite detailed and may require many hours to run on last generation processors. In order to quantify the effect of uncertainty on critical systems, models need to be combined and run several times with different initial and boundary conditions. Clearly, this leads to a time problem, as a single uncertainty analysis may take too long to be completed. Therefore, the development of novel numerical strategies is key to make the uncertainty quantification ever closer to the community of practitioners.

1.2 Reliability analyses of engineering structures

Reliability analyses and methods are powerful tools used in structural and system engineering to assess the level of safety both at the stage of design and operation. The aim of reliability methods is producing a design that meets some predefined performance objectives. Structures, during lifetime, undergo a series of conditions that depends on actions, such as loadings, thermal gradients, displacements, accelerations, etc., and on material strengths or thresholds, such as yielding stress, compressive strength, crack depth and so on. Both actions and material thresholds are random processes in space and time. Structural analyses turn the actions into structural responses, for example by means of finite elements models, which are subsequently compared against the material thresholds.

The structural responses are commonly referred to as demands, the material thresholds are called capacities and the space of all demands and capacities is referred to as state space. In the state space, the collection of varying demands and capacities identifies as many limit state surfaces as the number of capacities. The intersection and union of this limit state surfaces define two mutually exclusive domains: the failure domain, $\mathcal{X}_F$, and the survival domain, $\mathcal{X}_S$. A random state, $\boldsymbol{x}$, of the structural system, which

includes both demands and capacities, can be represented as a point in the state space, where the structure is in a "safe" state if the point is strictly contained in the survival domain, $\boldsymbol{x} \in \mathcal{X}_S$, whereas it is in an "unsafe" state if contained in the failure domain, $\boldsymbol{x} \in \mathcal{X}_F$.

The reliability, p_R, is formulated as the probability of a random state to be in the survival domain, whereas, the failure probability, p_F, where $p_R + p_F = 1$, is the probability of a random state to be in the failure domain. In the state space, some reliability metrics can be defined to assess to what extent the structure can be considered safe. For example, it is common to refer to the smallest distance between a random state and the limiting surface as the safety margin, M. When a probability space is superimposed to the system state space other metrics can be also defined, such as the reliability index, the design point, etc.

Reliability analyses provide the practical mean for evaluating the risk and the level of safety of the structural system. For time-invariant problems, assessing reliability involves the calculation of a multinomial integral. Failure occurs if the state is "unsafe", i.e. if the random state, $\boldsymbol{x}$, which is a vector of random variables, happens to be in the failure domain. Thus, the failure probability is the integral:

$$p_F = \int \cdots \int_{\mathcal{X}_F} f_X\left(x_1, ..., x_d\right) \mathrm{d}x_1 ... \mathrm{d}x_d; \tag{1.1}$$

where, f_X is the joint density function, and d is the number of state variables. In general, the integral of Eq. (1.1) is difficult to calculate, as the failure domain, $\mathcal{X}_F$ is seldom explicitly defined; thus, its computation can be prohibitive, especially for complex systems. Some of the main reasons why reliability is so difficult to calculate are listed in [61], and are here briefly recalled:

- The complexity of the structural systems often requires the numerical solution of nonlinear equations with multiple unknowns;
- A high number of random parameters has to be considered to accurately represent the uncertainties;
- The probabilistic definitions may go beyond common stationary Gaussian random processes.

1.2.1 Estimation of reliability by means of Monte Carlo simulation

Several methods have been proposed to assess reliability in recent and past literature. First attempts were oriented towards analytical methods [30], subsequently, numerical methods based on the calculation of the performance function Hessian [65] or based on asymptotic approximation [15] became more popular. However, these methods are increasingly inefficient with the number of random variables thus, increasingly difficult to

apply to problems of growing complexity. For these reasons, simulation methods based on Monte Carlo analysis have been proposed [52, 60]. Direct Monte Carlo simulation is independent of the problem complexity and is the most generally applicable method to estimate the reliability [53]. In practice, Monte Carlo simulation is performed by means of sampling a large number of random states, $\boldsymbol{x}$, from given probability distributions, and subsequently counting the number of "safe" states over the total. An indicator function, $\mathcal{I}_F$, is used in the direct method to label the states, with a *zero* if "safe" and with a *one* if "unsafe". The failure probability can be estimated by means of

$$p_F = \int_{-\infty}^{\infty} \cdots \int_{-\infty}^{\infty} \mathcal{I}_F[\boldsymbol{x} \in \mathcal{X}_F] \; f_X\left(x_1, ..., x_d\right) \mathrm{d}x_1 ... \mathrm{d}x_d. \tag{1.2}$$

If samples, $\boldsymbol{x}^{\{s\}}$, $s = 1, ..., N_S$, are generated according to the distribution f_X, there is no need to calculate the integral of Eq. (1.2); as the failure probability can be approximated by means of

$$\hat{p}_F = \frac{1}{N_S} \sum_{s=1}^{N_S} \mathcal{I}_F[\boldsymbol{x}^{\{s\}} \in \mathcal{X}_F]; \tag{1.3}$$

by generating a large number of samples, N_S, which provides an unbiased estimation of the failure probability. Clearly, the accuracy of the estimation of Eq. (1.3) depends on the number of samples and can be assessed computing the coefficient of variation, CoV, of the estimator, $\hat{p}_F$. The coefficient of variation of the failure probability estimator is

$$CoV[\hat{p}_F] = \sqrt{\frac{1 - p_F}{p_F \; N_S}}; \tag{1.4}$$

which implies that a sample size $N_S > 1/p_F$ is required for $CoV[\hat{p}_F] < 1$ and acceptable values, where $CoV[\hat{p}_F] < 0.3$, can be obtained for $N_S > 10/p_F$. Hence, a very large number of independent calls of the structural model are required by the method in order to assess the indicator function, $\mathcal{I}_F$, which can be infeasible in engineering practice, as the time for an individual model call can be quite long. The limitations of direct Monte Carlo can be resolved using Advanced Sampling methods, such as Importance Sampling [38], Line Sampling [21, 62], Directional Sampling [26], Subset Simulation [9], etc. Each individual method carries special performance features to target different classes of problems; for example Line Sampling is specially suited to estimate small failure probabilities in high dimensional spaces, provided that the limit state surface displays a single failure mode; whereas Subset Simulation estimates small failure probabilities despite the complexity of the limit state surface, although it may be affected by the curse of dimensionality.

1.3 Uncertainties in engineering modelling and design

Common sources of uncertainty often encountered in the engineering modelling can be listed as follows (see e.g. [25]):

- Inherent uncertainty in the material properties and load values, which can be classified as coming from natural phenomenon;
- Model uncertainty resulting from the selection of a (non-)probabilistic model form used to describe the uncertainty;
- Model uncertainty resulting from the selection of the physical model used to describe the derived (output) variables;
- Estimation uncertainty in the parameters of the (non-)probabilistic models;
- Estimation uncertainty of the parameters of the physical models;
- Errors in producing measurements from observations, based on which of the parameters are estimated. For example, errors involved in indirect measurements and non-destructive testing;
- Computational errors, numerical approximation and truncation errors in the derived (output) variables. For example, computation of effects of loading in a non-linear structure by finite element procedure, involves convergence tolerances and truncation errors;
- Errors arising from human activity and decisions, such as unintentional errors made in the modelling, design, construction and operation of a system.

1.4 Modelling of epistemic uncertainty and subjectivity

Although the majority of scientists agree about the existence of different kinds of uncertainty, many are still divided on how to model epistemic uncertainty. Two opposite schools of thought can still be identified: one is the Bayesian school, where subjectivity and more generally epistemic uncertainty is modelled within a pure probabilistic framework, and the other is the Set-theoretic school, in which different kinds of uncertainty are modelled with tailored mathematical representation based on set-valued descriptors. The Bayesian argument follows from the acceptance that probability can be given a subjective interpretation. In this view, the probability of an event A represents the degree of belief with respect to its occurrence. Often subjective probabilities are linked to betting, for example, the probability $\mathrm{P}(A)$ of the event A, is seen as the equilibrium price for which one is willing to buy (or sell) a gamble in exchange of 1, if the event does (or does not) occur. Subjective probabilities are always seen conditioned to the

background knowledge, K, and it is common to refer to the event probability as the conditional probability $\mathrm{P}(A|K)$. In risk and reliability analyses, the background knowledge is often represented by the data at analysts disposal, and the probability $\mathrm{P}(A|K)$ is referred to as posterior probability, which is calculated using the Bayesian formula

$$\mathrm{P}(A|K) = \frac{\mathrm{P}(A)\ \mathrm{P}(K|A)}{\mathrm{P}(K)},$$

where, in order to calculate the posterior probability it is necessary to formulate a likelihood function, $\mathrm{P}(K|A)$, and a prior probability, $\mathrm{P}(A)$. The element of subjectivity of the Bayesian approach is concentrated into the prior probability which represents the experts degree of belief about that particular event. Therefore, a Bayesian analysis requires an analyst to have prior information on the probability of all events. This constitutes a limitation, as it is not always possible to have prior knowledge on all the events especially when a complex system is under assessment. When prior knowledge is not available, the uniform distribution function is often used, justified by Laplace Principle of Insufficient Reason [58], which can be interpreted as follows: all events for which a probability distribution is not known in a given sample space are equally likely. Clearly, this leads to a paradox, as, in situations of complete lack of knowledge, assigning uniform mass to all events is a quite strong assumption [63].

1.4.1 Imprecise probability

A great effort has been made within the Set-theoretic community to explicitly account for epistemic uncertainty avoiding subjective probabilities. For example, Ben-Haim [13, 14] developed info-gap decision theory which has been applied to solving structural reliability problems using real-valued measure functions. In [40], Moens and Vandepitte showed how finite element analysis can be embedded into a non-probabilistic framework. In [41], Möller, Graf and Beer, used fuzzy numbers to quantify uncertainty in structural analysis, while in [79], Zhang, Beer and Koh used interval analysis for system identification of linear structures to account for model uncertainties. However, non-probabilistic approaches may be limited to only specific problems and may be difficult to generalise to include aleatory uncertainty. In this direction, several approaches have been proposed towards more general uncertainty quantification, and have also been developed for reliability problems. For example in [33], Cai introduced fuzzy reliability theory, while in [27, 28], Dubois and Prade translated the recent possibility theory based on Dempster-Shafer measures of plausibility and belief [23, 64] to reliability problems using the Zadeh [76] extension principle. In the same way, Tonon [67], Oberguggenberger [47] and Alvarez [3, 4] used possibility measures on problems of engineering interest.

Imprecise probability represents the natural meeting point between Bayesian and Set-theoretic views, as it extends classical probability theory, without any more complication of interpretation. The theory of imprecise probability, also known as theory of interval probability [73], generalises the probability by using the interval $[\underline{\mathrm{P}}(A),\ \overline{\mathrm{P}}(A)]$ to quantify uncertainty on A, with lower probability $\underline{\mathrm{P}}(A)$ and upper probability $\overline{\mathrm{P}}(A)$, such that $0 < \underline{\mathrm{P}}(A) < \overline{\mathrm{P}}(A) < 1$. The classical 'precise probability' occurs if $\underline{\mathrm{P}}(A) = \overline{\mathrm{P}}(A)$, whereas the extreme 'uninformative' situation occurs if $[\underline{\mathrm{P}}(A),\ \overline{\mathrm{P}}(A)] = [0,\ 1]$, which is used to express complete lack of knowledge about the event A. The difference $\overline{\mathrm{P}}(A) - \underline{\mathrm{P}}(A)$ is used as a measure to quantify indeterminacy or imprecision. Again, the probability interval can be interpreted in different ways. It can be interpreted as the relative frequency of the event A, given the limited amount of information about A. Alternatively, within the subjective argument, the lower probability can be seen as the maximum price for which one would buy a gamble that pays 1 if A occurs and 0 otherwise, and the upper probability as the minimum price for which one would sell the gamble.

In [18, 19, 68], Coolen and Utkin contribute to reliability theory and methods using lower and upper (imprecise) probabilities, as "it is widely accepted that, by generalizing classical precise probability theory in a mathematically sound manner, with clear axioms and interpretations, this theory provides an attractive approach to generalized uncertainty quantification". In [34], Klir points out that the theory of imprecise probability is the most general, as it includes fuzzy probability, random set theory, evidence theory and possibility theory.

In risk analysis, Sentz and Ferson [63] identify three major frameworks to characterise the interval-based representation of uncertainty which are: imprecise probability [22,72], possibility theory [27] and Dempster-Shafer theory of evidence [23,64]. In the same paper, the authors point out three important implications of using interval or set measures of probability: (i) it is not necessary to elicit a precise or exact measurement from an expert or an experiment; (ii) there is no need to use the Principle of Insufficient Reason, in case of complete lack of knowledge about the likelihood of multiple events; (iii) the Kolmogorov axiom of additivity is not imposed, meaning that probability measures can add up to a number smaller than one to account for conflicting evidence, or greater than one in case of cooperative multiple sources of uncertainty. For more details on how imprecise probability deals with conflicting evidence and cooperative sources of information see Ref. [63].

1.5 Numerical implementation

The uncertainty quantification and management require the availability of flexible numerical tools able to deal with the aforementioned different uncertainty representations. Since a single non-deterministic analysis is, in general, computationally quite demanding, such numerical tools need to be very efficient and scalable. The computational cost of the uncertainty analysis could be excessive even when the solver is reasonably fast (e.g. a single call of the performance function of the challenge problem described in Chapter 8 requires 2 seconds on a common desktop computer). For these reasons, the proposed approach has been developed and integrated into the OpenCossan framework [54].

OpenCossan OpenCossan is a collection of open source algorithms, methods and tools released under the LGPL licence, and under continuous development at the Institute for Risk and Uncertainty at the University of Liverpool, UK. The source code is available upon request at the web address in Ref. [1].

OpenCossan is also the computational core of a general purpose software, namely COSSAN-X, originally developed by the research group of Prof. G.I. Schuëller at the University of Innsbruck, Austria [53]. As a general purpose software, it means that a reasonably wide range of engineering and scientific problems can be treated by the software.

This computational core, developed in MATLAB® using an object-oriented programming paradigm, includes several predefined solution sequences to solve a number of different problems. The framework is organized in classes, i.e. data structures consisting of data fields and methods together with their interactions and interfaces. Thanks to the modular nature of OpenCossan, it is possible to define specialized solution sequences including reliability methods, optimisation strategies and surrogate modelling or parallel computing strategies to reduce the overall cost of the computation.

OpenCossan provides intuitive, clear, well documented and human readable interfaces to the classes. Furthermore, the developed numerical methods are highly scalable and parallelisable, thanks to its integration with distributed resource management, such as openlava and GridEngine. These job management tools allow taking advantage of high performance computing.

1.6 Structure of thesis

Organisation of chapters in this thesis follows a simple structure, which is schematically depicted in Figure 1.1. The theoretical background of the thesis and a brief introduction to Random Sets is provided in Chapter 2. Subsequently, Chapter 3 describes the enhanced Advanced Sampling technique and Chapter 4 makes use of its developments

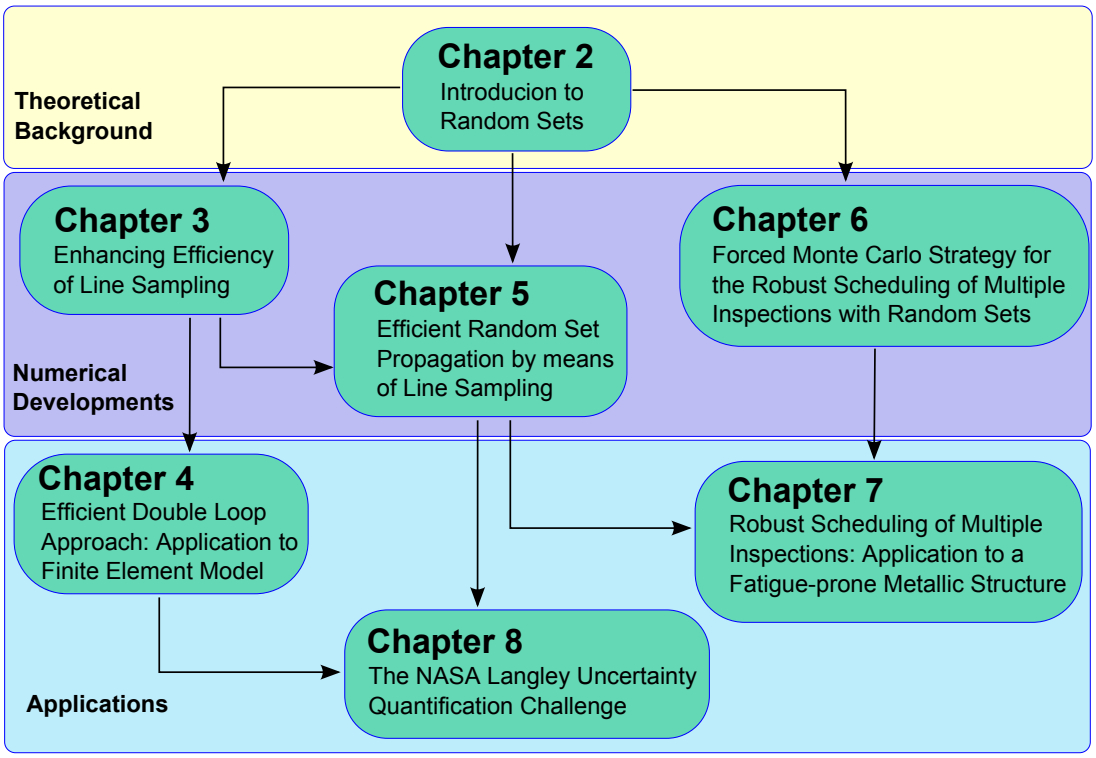

Figure 1.1: Thesis outline and chapter organisation

to introduce imprecision within a Double Loop approach. Applications to a finite element model are also shown in Chapter 4. Chapter 5, combines the developments of Chapter 3 with Random Sets, and applies the Random Set approach to a synthetic numerical example. Chapter 6 introduces another Advanced Sampling strategy, called forced Monte Carlo simulation, which is developed to allow for uncertainty separation and thus to include the Random Set approach. The novelty of Chapter 6 is the application of such strategy to the scheduling of maintenance activities to a fatigue-prone metallic component of a bridge girder. Chapter 7 is very much linked to Chapter 6, as it shows how the strategy developed in Chapter 6 can be applied to the numerical example of fatigue-prone metallic components. Chapter 8 describes in detail most of the NASA Langley Multidisciplinary Uncertainty Quantification challenge, to demonstrate capabilities and limitations of the developed methods when applied to a real case study. Lastly, some conclusions and recommendations are provided in Chapter 9, to summarise the presented work and indicate directions for potential future developments.

Chapter 2

Introduction to Random Sets

Random sets are specially suited to model, under the same numerical framework, uncertainty represented as cumulative distribution functions, intervals [42], distribution-free p-boxes [29], parametric p-boxes [77], possibility distributions [28] and Dempster-Shafer structures [23, 64] without making any assumptions at all [3, 4]. In other words, Random Sets allow the modelling of the aforementioned representations of uncertainty in a unified framework. Random Sets can be seen as random variables that sample sets (called focal elements) as realizations, instead of real numbers.

In this dissertation, many of the proposed solutions make strong use of this kind of representation. Therefore, in this chapter, a brief review of the main concepts of random set theory, required for the subsequent discussion, is provided.

2.1 Definition of a Random Set

Let $(\mathbf{\Omega}, \sigma_\Omega, P_\Omega)$ be a probability space, and $(\mathcal{F}, \sigma_\mathcal{F})$ be a measurable space such that the *focal set*, $\mathcal{F}$, is $\mathcal{F} \subseteq \mathcal{P}(\mathcal{X})$, where, $\mathcal{X} \neq \varnothing$ is the universal set of events and $\mathcal{P}(\mathcal{X})$ is its power set. A *random set*, Γ, is the measurable mapping

$$\Gamma : \mathbf{\Omega} \to \mathcal{F}. \tag{2.1}$$

The general definition of Eq. (2.1) can be particularised, as shown in Alvarez [4], for the application of random sets to problems involving general uncertainty models. Alvarez [4] proposed to set $\mathbf{\Omega} := (0, 1]^d$ and restrict σ_Ω to the Borel σ-field $\sigma_\Omega := (0, 1]^d \cap \mathscr{B}^d$, in order to use d-dimensional boxes as elements of $\mathcal{F}$. In this way, a *copula* function, C, can be defined to hold the dependence information on the joint distribution of the random set. This implies, for example in a one-dimensional space, $d = 1$, that the probability measure, P_Ω, corresponds to the CDF of a random variable, $\tilde{\alpha}$, uniformly distributed in $(0, 1]$, i.e. $F_{\tilde{\alpha}}(\alpha) := P_\Omega[\tilde{\alpha} \leqslant \alpha] = \alpha$. This makes sampling from a random set a very straightforward numerical operation.

A *focal element*, $\gamma := \Gamma(\alpha) \in \mathcal{F}$, with $\alpha \in \boldsymbol{\Omega}$ is an individual realization of the focal set, $\mathcal{F}$. The mapping of Eq. (2.1), after the particularisation, becomes $\Gamma : \ \alpha \mapsto \Gamma(\alpha)$ and can be used to define the probability, $P_\Gamma := P_\Omega \circ \Gamma^{-1}$, of any event, $F \in \sigma_\mathcal{F}$, as

$$P_\Gamma(F) = (P_\Omega \circ \Gamma^{-1})(F) = P_\Omega \left\{\alpha \in \boldsymbol{\Omega} : \Gamma(\alpha) \in F\right\}. \tag{2.2}$$

In the same way, lower and upper probability bounds, as originally proposed in Dempster, can be defined as

$$\underline{P}_\Gamma(F) = \mathrm{LP}_\Gamma(F) := P_\Omega \left\{\alpha \in \boldsymbol{\Omega} : \Gamma(\alpha) \subseteq F, \Gamma(\alpha) \neq \varnothing\right\}; \tag{2.3}$$

and

$$\overline{P}_\Gamma(F) = \mathrm{UP}_\Gamma(F) := P_\Omega \left\{\alpha \in \boldsymbol{\Omega} : \Gamma(\alpha) \cap F \neq \varnothing\right\}. \tag{2.4}$$

When all focal elements are singletons, Γ becomes a random variable, X, hence $\Gamma(\alpha) = X(\alpha)$, and the probability of the event, F, is

$$P_X(F) := (P_\Omega \circ X^{-1})(F) = P_\Omega \left\{\alpha : X(\alpha) \in F\right\}. \tag{2.5}$$

where, $\underline{P}_\Gamma(F) \leqslant \mathrm{P}_X(F) \leqslant \overline{P}_\Gamma(F)$. The definition of lower and upper probability bounds of Eqs. (2.3) and (2.4) allows to describe different models of uncertainty, as it separates the aleatory component, fully represented by the random vector $\boldsymbol{\alpha} \in \boldsymbol{\Omega} \equiv (0,1]^d$, from the epistemic component, which is usually obtained as a collection of intervals.

2.2 Random Sets: CDFs, Intervals and Probability Boxes

Random Sets can be used to model the uncertainty by means of cumulative distribution functions, intervals, probability boxes, normalised fuzzy sets and Dempster-Shafer structures. In this work, CDFs, intervals and probability boxes are considered as uncertainty representations.

2.2.1 Cumulative Distribution Functions

A CDF, F_X, is used to express the probability distribution of a random variable, X, as already shown in Eq. (2.5), where $F_X(x) = P_X(X \leqslant x)$ for $x \in \mathcal{X} \subseteq \mathbb{R}$, and fully characterises the random variable, X. CDFs can be represented as random sets $\Gamma : \Omega \to \mathcal{F}$ where $\mathcal{F}$ is the collection of focal elements $\Gamma(\alpha) := F_X^{-1}(\alpha), \ \forall \alpha \in \boldsymbol{\Omega}$. The *inverse* of the CDF, F_X, is defined by $F_X^{-1}(\alpha) := \inf\{x : F_X(x) \geqslant \alpha, \alpha \in (0,1]\}$. Note that the representation of the CDF as a random set only contains the aleatory component, which is given either by α, or by its corresponding sample $x = F_X^{-1}(\alpha)$.

2.2.2 Intervals

An *interval*, $\overline{\underline{x}} = [\underline{x},\ \overline{x}]$, can be represented as the random set $\Gamma : \mathbf{\Omega} \to \mathcal{F},\ \alpha \mapsto \overline{\underline{x}}$ defined on $\mathbb{R}$ where the focal set contains the unique focal element $[\underline{x},\ \overline{x}]$, that is, $\mathcal{F} = \overline{\underline{x}}$ and $\alpha \in (0, 1] \equiv \mathbf{\Omega}$; in this case, P_Γ is specified by Eq. (2.2). In other words, all the samplings of $\alpha \in \mathbf{\Omega}$ draw the same interval $\overline{\underline{x}}$. Note that the interval representation as a random set does not contain an aleatory component, as all α-s map to the same focal element $\overline{\underline{x}}$. In this case, the epistemic component is given by the interval itself. An alternative equivalent way to denote an interval is by means of the symbol $I_x = [l_x,\ u_x] = [\underline{x},\ \overline{x}]$.

2.2.3 Probability boxes

A *probability box* or *p-box* (term coined by Ferson et al. [29]), $\left[\overline{F}, \underline{F}\right]$, is the set of CDFs $F : \underline{F}(x) \leqslant F_X(x) \leqslant \overline{F}(x), \forall\ x \in \mathbb{R}$, delimited by a lower CDF bound $\underline{F}$ and an upper CDF bound $\overline{F}$. Lower and upper CDF bounds define the set of distribution functions that collectively represents the epistemic uncertainty about the variable. Note that left bound $\overline{F}$ is an upper bound on the probabilities and a lower bound on quantiles (i.e. the x-values), while the right bound $\underline{F}$ is a lower bound on the probabilities and an upper bound on quantiles. The class of functions contained in the p-box may not have additional restrictions or alternatively may belong to a reduced class of CDFs; using this distinction, probability boxes can naturally be grouped into distribution-free and parametric p-boxes.

2.2.3.1 Distribution-free p-boxes

Distribution-free p-boxes (also known as *non-parametric* p-boxes, free p-box or simply p-boxes) appear when the CDF of a random variable cannot be precisely specified, given that the CDF family is unknown; nonetheless it is possible to define the upper, $\overline{F}$, and lower, $\underline{F}$, CDF bounds. These bounds can either be defined in advance or can be estimated using for example the methods listed in Zhang et. al. [78]. Note that distribution-free p-boxes do not make any assumption about the family or shape of the CDFs that belong to the p-box.

Since only upper and lower CDF bounds are concerned in a free p-box, two different ways to define a p-box can be identified. One way consists in specifying the upper and lower CDFs, which may have unknown or inhomogeneous parental distribution models. In this case, the random set $\Gamma : \mathbf{\Omega} \to \mathcal{F},\ \alpha \mapsto \Gamma(\alpha)$, on $\mathbb{R}$, is the ensemble of focal elements, $\Gamma(\alpha) := \left[\overline{F}(\alpha)^{-1},\ \underline{F}(\alpha)^{-1}\right]$, for $\alpha \in (0, 1] \equiv \mathbf{\Omega}$, with $\overline{F}^{-1}$ and $\underline{F}^{-1}$ denoting the inverse upper and lower CDFs bounds, respectively. With this representation, a focal element can be obtained as

$$\gamma(\alpha) = \left[\underline{F}, \overline{F}\right]^{-1}(\alpha) = \left\{x : F(x) = \alpha, F \in \left[\underline{F}, \overline{F}\right]\right\}. \tag{2.6}$$

An alternative definition, widely used in this work, consists in defining upper and lower CDFs by means of interval (or set-valued) hyperparameters. As a result the bounding CDFs are obtained from the envelope of known distribution functions. So, for example, a p-box can be defined as the collection of all distribution functions which CDFs are bounded by normal distributions, $F \sim \mathcal{N}(\underline{\mu}, \overline{\sigma})$, which mean and standard deviation belong to the intervals, $\underline{\mu} = [\underline{\mu},\ \overline{\mu}]$ and $\overline{\sigma} = [\underline{\sigma},\ \overline{\sigma}]$. In general, a CDF with interval hyper-parameters, $\overline{\underline{\theta}}_i,\ i = 1, \ldots, m$, denoted by $F(\cdot; \overline{\underline{\theta}}_1, \ldots, \overline{\underline{\theta}}_m)$, can be given a random set representation as the image through the function, F^{-1}, of the input intervals $\left\{\overline{\underline{\theta}}_i : i = 1, \ldots, m\right\}$ together with the uniform α-sample obtained from $\mathbf{\Omega}$. In consequence, it can be represented as the random set $\Gamma : \mathbf{\Omega} \to \mathscr{F}, \alpha \mapsto \Gamma(\alpha)$ defined on $\mathbb{R}$, where $\mathcal{F}$ is the collection of focal elements $\mathcal{F} = \left\{F^{-1}(\alpha; \overline{\underline{\theta}}_1, \cdots,\ \overline{\underline{\theta}}_m) : \alpha \in \mathbf{\Omega}\right\}$. In this way, the focal element aleatory component, α, can be separated from the epistemic component, which is obtained as the Cartesian product, $\overline{\underline{\boldsymbol{\theta}}} = \times_{i=1}^{m} \overline{\underline{\theta}}_i := \overline{\underline{\theta}}_1 \times \cdots \times \overline{\underline{\theta}}_m$. This representation of distribution-free p-boxes shows that for a single realization of the aleatory component, α, a focal element contains the image through F^{-1} of all the possible combinations of values within the intervals of the hyperparameters of the parental CDF, F. Provided this definition, the upper and lower CDFs are

$$\overline{F}^{-1}(\alpha) = \inf_{\boldsymbol{\theta} \in \overline{\underline{\boldsymbol{\theta}}}} F^{-1}(\alpha; \theta_1, \ldots, \theta_m); \qquad \underline{F}^{-1}(\alpha) = \sup_{\boldsymbol{\theta} \in \overline{\underline{\boldsymbol{\theta}}}} F^{-1}(\alpha; \theta_1, \ldots, \theta_m). \tag{2.7}$$

Note that with this definition, the bounding CDFs may not entirely belong to the same parental distribution function, as they are often the envelope of two or more parental distributions.

2.2.3.2 Parametric p-boxes

Parametric p-boxes (also known as *distributional* p-boxes) appear when there is uncertainty in the hyperparameters of a given distribution function, which are provided as intervals. For instance, let again $F \sim \mathcal{N}(\underline{\mu}, \overline{\sigma})$ be a Normal distribution function with interval mean, $\underline{\mu}$, and interval standard deviation, $\overline{\sigma}$. All Normal distribution functions that have mean and standard deviation inside the specified intervals belong to the probability box. Despite the lower and upper CDF bounds enclosing infinite non-normal distributions, only distributions from the original normal parental model are considered. This constraints the parametric p-boxes to a smaller set of distributions compared to the distribution-free ones. This representation does not look at the CDF bounds, but is only concerned with the distributions responsible for the lower and upper probability bounds.

Parametric p-boxes cannot be treated using a random set representation, because only one distribution at a time is selected and therefore, it is not possible to separate the aleatory from the epistemic component. Distributional p-boxes can be treated using

a double loop Monte Carlo-optimisation strategy, in which the inner loop samples α-s from a Copula function, in $(0, 1]$, and the outer loop picks $\boldsymbol{\theta}$-s to search for the extrema in $\overline{\underline{\boldsymbol{\theta}}} = \times_{i=1}^{m} \overline{\underline{\theta}}_i$. If the dimension of the epistemic space, $\boldsymbol{\Theta} \equiv \overline{\underline{\boldsymbol{\theta}}}$ is not too high (indicatively $\leqslant 5$), a double loop Monte Carlo strategy can be adopted, where the outer Monte Carlo is used to perform a heuristic search in the epistemic space, $\boldsymbol{\Theta}$.

Note that the use of parametric p-boxes always results in narrower intervals of probability compared to the distribution-free case, as a consequence of searching within a smaller set of distribution functions.

2.3 Copulas

A *copula* is a function $C : [0, 1]^d \to [0, 1]$ that relates a joint cumulative density functions to its marginals, carrying in this way the dependence information in the joint CDF such that each of its marginal CDFs is uniform on the interval $[0, 1]$. According to Sklar's theorem (see Ref [**?**]), a multivariate CDF $F_{X_1,\ldots,X_d}(x_1, \ldots, x_d) = P[X_1 \leqslant x_1, \ldots, X_d \leqslant x_d]$ of a random vector $(X_1, X_2, \ldots, X_d)$ with marginals $F_{X_i}(x_i) = P[X_i \leqslant x_i]$ can be given as $F_{X_1,X_2,\ldots,X_d}(x_1, \ldots, x_d) = C\left(F_{X_1}(x_1), \ldots, F_{X_d}(x_d)\right)$, where C is a copula function. The copula C is itself a CDF and it contains all information on the dependence structure between the variables $(X_1, X_2, \ldots, X_d)$, whereas the marginal cumulative distribution functions F_{X_i} contain all information on the marginal distributions. The reader is referred to Ref. [46] for an exhaustive introduction to copulas.

2.4 The Aleatory and Epistemic Spaces

The random set representation allows it to explicitly separate the aleatory from the epistemic component; thus, an *aleatory space*, $\boldsymbol{\Omega}$, and an *epistemic space*, $\boldsymbol{\Theta}$ are defined.

The aleatory space, $\boldsymbol{\Omega}$, holds all the aleatory components of the uncertainty model and it is used to produce samples from joint random sets. A sample can be obtained by drawing a random vector, $\boldsymbol{\alpha} \in (0, 1]^d$ from the copula function, C, that defines the dependence between marginal distributions. This space contains only probabilistic information about the variables. Without loss of generality, all copulas in our discussion will be defined on $\boldsymbol{\Omega}$, and subsequent discussion will assume that the set $\boldsymbol{\Omega}$ includes copula information.

The epistemic space, $\boldsymbol{\Theta}$, is obtained, without limiting generality, making the Cartesian product of all intervals, $\overline{\underline{\theta}}_i,\ i = 1, \ldots, q$, that define the epistemic uncertainty, that is $\boldsymbol{\Theta} = \times_{i=1}^{q} \overline{\underline{\theta}}_i$. A *reduced epistemic space* can be obtained when additional information is available and the *true uncertainty model*, denoted by the point $\boldsymbol{\theta}^* \in \boldsymbol{\Theta}$, will result once all epistemic uncertainty is removed from $\boldsymbol{\Theta}$. Note that, using the random set representation, the epistemic space, $\boldsymbol{\Theta}$, does not make a distinction between inter-

val parameters and interval hyperparameters, which is particularly convenient from a notational viewpoint.

2.5 System function as image of a Random Set

Let $\mathcal{G} : \mathcal{X} \to \mathbb{R}$ denote a function that represents the system performance, where $\mathcal{X} \subseteq \mathbb{R}^d$, and let $\mathcal{W} : \mathbf{\Omega} \times \mathbf{\Theta} \to \mathscr{X}$ be a function which returns a point in $\Gamma(\boldsymbol{\alpha}) \subseteq \mathcal{X}$. Note that, one hand, the image of $\mathbf{\Theta}$ through $\mathcal{W}(\boldsymbol{\alpha}; \cdot)$ is the focal element $\Gamma(\boldsymbol{\alpha})$; on the other hand, the image of $\mathbf{\Omega}$ through $\mathcal{W}(\cdot; \boldsymbol{\theta})$ can be modelled as a CDF with parameter vector $\boldsymbol{\theta}$, that is, $F(\cdot; \boldsymbol{\theta})$.

It is convenient to introduce the composite function $\mathcal{H} : \mathbf{\Omega} \times \mathbf{\Theta} \to \mathbb{R}$, where $\mathcal{H} = \mathcal{G} \circ \mathcal{W}$, in fact, $\mathcal{H}$ represents the system as well, but its domain is the Cartesian product, $\mathbf{\Omega} \times \mathbf{\Theta}$ of the aleatory and epistemic spaces (see Figure 2.1).

2.5.1 Propagation of focal elements: the extension principle of random sets

The capability to propagate intervals, CDFs, p-boxes, and their combination through a system represents the core of the Random Set computational framework. In order to find the image of a focal element, $\gamma_i \subseteq \mathcal{X}$, through the function $\mathcal{G} : \mathcal{X} \to \mathbb{R}$, the extension principle of random sets is used (see Ref. [28]). This can be done by means of optimisation [7], sampling [21], vertex methods [74], or interval arithmetic [43, 80]. Among these methods, optimisation seems to be the most generally applicable, although not always the easiest to use.

With the optimisation method, the image of the set γ_i through $\mathcal{G}$, can be calculated as

$$\mathcal{G}(\gamma_i) = \mathcal{G}(\Gamma(\boldsymbol{\alpha}_i)) = \left[\underline{\mathcal{G}},\ \overline{\mathcal{G}}\right] \tag{2.8}$$

where,

$$\underline{\mathcal{G}} := \min_{\boldsymbol{x}_i \in \Gamma(\boldsymbol{\alpha}_i)} \mathcal{G}(\boldsymbol{x}_i) \qquad\qquad \overline{\mathcal{G}} := \max_{\boldsymbol{x}_i \in \Gamma(\boldsymbol{\alpha}_i)} \mathcal{G}(\boldsymbol{x}_i)\,; \tag{2.9}$$

are limit state functions defined in $\mathbf{\Omega}$. Using the function $\mathcal{H}$ defined in the above Section, Eqs. 2.9 can be written as an optimisation over the epistemic space as

$$\underline{\mathcal{G}} := \min_{\boldsymbol{\theta} \in \mathbf{\Theta}} \mathcal{H}(\boldsymbol{\alpha}_i, \boldsymbol{\theta}) \qquad\qquad \overline{\mathcal{G}} := \max_{\boldsymbol{\theta} \in \mathbf{\Theta}} \mathcal{H}(\boldsymbol{\alpha}_i, \boldsymbol{\theta})\,. \tag{2.10}$$

This approach is usually employed when $\mathcal{G}$ is a nonlinear function of the system parameters. The main drawback of this method is that it requires a high computational effort.

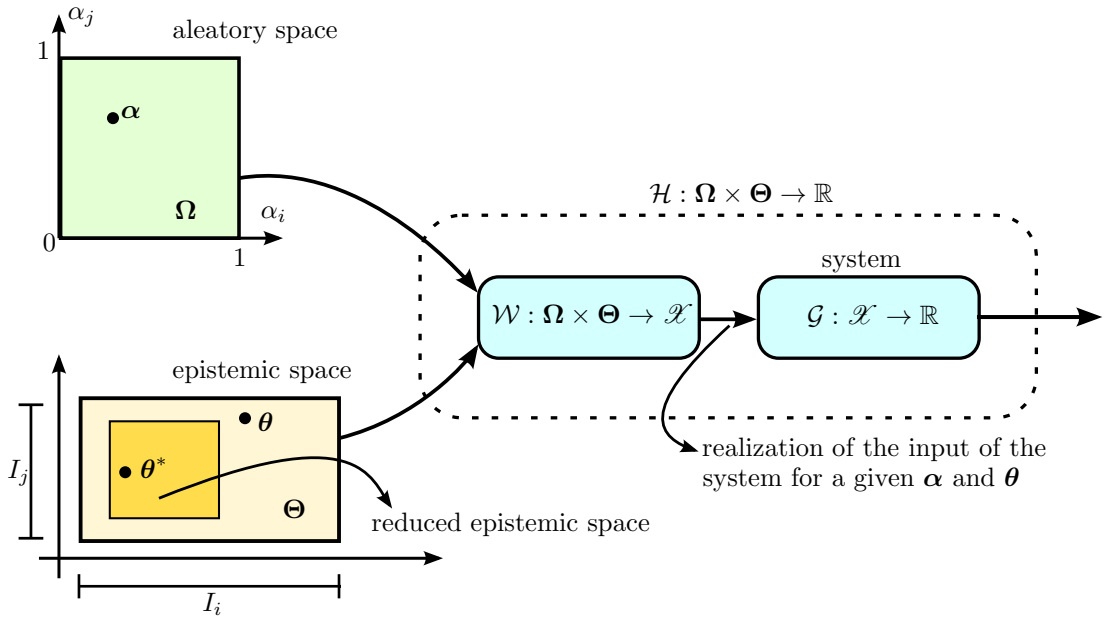

Figure 2.1: Aleatory and epistemic spaces and propagation through the system function

2.5.2 Sampling of a Random Set

A sample from a random set is obtained by generating a number, α, in the unit interval $(0, 1]$ and then, retrieving the corresponding focal element $\Gamma(\alpha)$. A 2-d sample from a probability box is obtained drawing an $\boldsymbol{\alpha}$ uniformly distributed in $(0, 1]^2$, and then its corresponding "α-cut" $\underline{\boldsymbol{x}} = \overline{F}^{-1}(\boldsymbol{\alpha})$, $\overline{\boldsymbol{x}} = \underline{F}^{-1}(\boldsymbol{\alpha})$ is obtained, as shown in Figure 2.2.

In the case of multivariate random sets, a sample $\boldsymbol{\alpha} \in \Omega$ is drawn from the copula C that models the dependence between the input variables. Then, the corresponding marginal focal elements are obtained and combined as explained in the next subsection. Take into account that n samples of a random set form the Dempster-Shafer structure $(\mathcal{F}_n, m)$, where $\mathcal{F}_n$ denotes the set of all sampled focal elements, the basic mass assignment m associated to each focal element is equal to $1/n$. Note that a Dempster-Shafer structure is itself a finite random set [3, 4].

2.5.3 Combination of focal elements

After sampling each input variable, a combination of the sampled focal elements is carried out. Usually, the joint focal elements are given by the Cartesian product $\times_{i=1}^{d} \gamma_i \subseteq \mathcal{X}$ where d is the number of input variables, $\gamma_i := \Gamma(\alpha_i)$ are the sampled focal elements from every input variable (that is, γ_i represents a sampled marginal focal element). Some of these γ_i are intervals, some other, points. As long as every sample of an input variable can be represented by γ_i or by the corresponding α_i, the joint focal element can be represented either by the d-dimensional box $\boldsymbol{\gamma} := \times_{i=1}^{d} \gamma_i \subseteq \mathcal{X}$ or by the point $\boldsymbol{\alpha} := [\alpha_1, \alpha_2, \ldots, \alpha_d] \in \boldsymbol{\Omega}$ (see Figure 2.1).

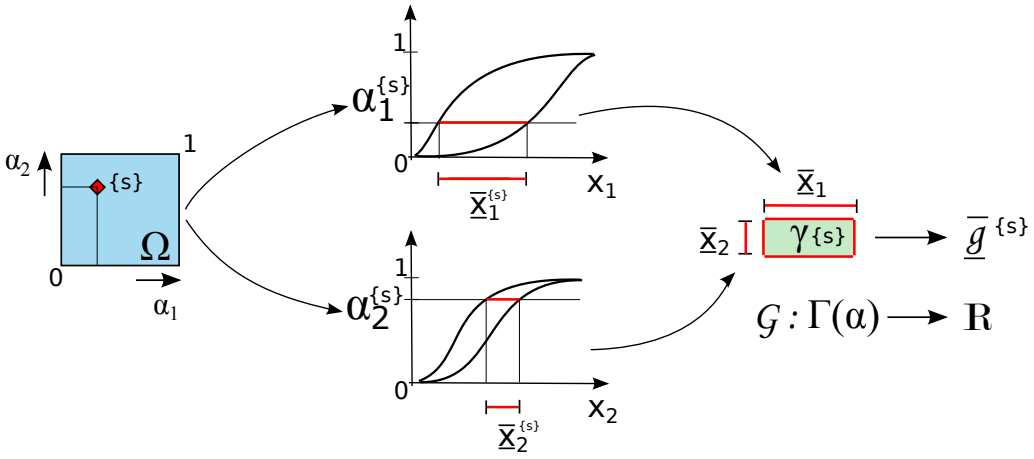

Figure 2.2: Sample of a 2-dimensional focal set

2.6 Double Loop and Random Set approaches

In this work, a distinction is made between two independent approaches. In essence, this distinction is made because the Random Set approach cannot capture uncertainties in the form of parametric p-boxes. Being able to handle parametric p-boxes may be necessary in applications where the distribution model type is known with certainty. The Double Loop approach allows for using parametric p-boxes with all the consequent advantages, such as narrower probability intervals and one-to-one link between input and output extremes. As prompted by the name, a Double Loop approach consists in running two nested loops, where the inner loop is responsible for sampling an aleatory component while the outer loop selects an epistemic component. In this way, every instance of the outer loop simulates a distribution function with as many samples as specified by the inner loop. Eventually, all the outer loop instances are collected and only the ones corresponding the bounds of the statistics of interest are kept. This approach can be very expensive, essentially because the objective of the search (outer loop) is an estimate obtained from a Monte Carlo simulation, which requires either stochastic or evolutionary optimisation algorithms to be solved. However, the sampling procedure can be enhanced by means of importance sampling methods, which reduce the noise associated with the estimation and require significantly fewer samples. Also, the optimisation can be simplified if something is known about the underlying model, as will be shown in Chapter 4.

On the other hand, the Random Set approach does not require the p-box to be parametric, and it can deal with any random set representation of uncertainty. This approach separates the aleatory from the epistemic component, making it possible to decouple the optimisation from the sampling procedures. This comes with the advantage of running optimisation on deterministic objective functions (provided that the system performance is deterministic), but still with the limitation of calling as many

optimisations as the number of samples, which can be quite large for small probabilities. This limitation can be resolved by developing importance sampling strategies to deploy within the aleatory space $\mathbf{\Omega}$, as will be shown in Chapter 5. Note that the Random Set approach treats any p-box as a distribution-free p-box, even if the distribution model type is specified.

2.7 Chapter summary

In this chapter an overview of the use of Random Sets has been presented. Random Sets can be used to model aleatory and epistemic uncertainty at the same time, as they combine randomness and imprecision within the same numerical framework. The advantage of using Random Sets derives from the fact that many different uncertainty representations can be modelled, such as intervals, p-boxes, Dempster-Shafer structures, fuzzy variables and fuzzy p-boxes. Therefore, Random Sets represent a unifying numerical tool to deal with general uncertainty quantification. Another advantage of using Random Sets consists in keeping the aleatory and epistemic uncertainty separated, as this helps in identifying where and to what extent the epistemic uncertainty can be reduced. Random Sets are generalised set-valued random variables which samples can be generated according to well-known sampling schemes already in place for the random variables. Once instances (focal elements) of a Random Set are generated, their combination requires specific min-max propagation techniques. Within the Random Set approach, min-max propagation techniques include interval arithmetic, interval analysis, sensitivity analysis (monotonicity check), global optimisation methods, Latin Hypercube sampling, etc. The propagation of a single focal element can be quite expensive if the system behaves like a black-box as the search for a minimum and a maximum has to be performed by means of blind sampling or global optimization algorithms. Alternative to the Random Set approach, in this chapter the Double Loop approach is also presented. However, the Double Loop approach is capable of replacing the Random Set approach only if the probability distribution type is specified. A typical example of the use of the Double Loop approach is when the probability distributions type is fixed and the moments or the hyper-parameters are set-valued. In this situation the two propagation approaches are expected to provide different responses, as differently from the Double Loop approach, the Random Set approach searches an infinite number of probability distribution types. In other words, in a scenario where the sampling uncertainty can be neglected, the Random Set approach is always going to provide wider ranges than the Double Loop approach.

Chapter 3

Enhancing the Efficiency of Line Sampling

3.1 Advanced Line Sampling

The computation of failure probabilities can be associated with a quite significant numerical effort. In cases where the number of random variables is high and the limit state surface is nonlinear, methods based on the computation of the Hessian become impractical. In these cases, advanced simulation methods represent a useful alternative. Here, a new method that extends the concept of Line Sampling is presented. The method, Advanced Line Sampling (ALS), increases the efficiency of performing reliability analyses [21]. In addition the method implements important features to increment the efficiency to estimate failure probability bounds in presence of imprecision.

3.1.1 Concept of Line Sampling

Line Sampling, introduced in [36], and recently applied in [53], is an advanced simulation method developed to efficiently compute small failure probabilities for high dimensional problems. The method exploits the metric of the Standard Normal Space (SNS) and requires the knowledge of the so-called "important direction", which is defined as the vector $\boldsymbol{a} \in \mathbb{R}^d$ pointing towards the failure region. An initial approximation for the important direction is commonly obtained by computing the gradient of the performance function, $\nabla\mathcal{G}$, at the origin of the SNS (see e.g. [51]). Simulation methods estimate the failure probability by computing the integral in the transformed SNS

$$p_F = \int_{\mathbb{R}^{d-1}} \mathcal{I}_F(\boldsymbol{u})\ \mathrm{d}\Phi(\boldsymbol{u}); \tag{3.1}$$

where, $\mathcal{I}_F : \mathbb{R}^d \to \{0, 1\}$ is the indicator function, which is 1 if $\mathcal{G} \leqslant 0$ and 0 otherwise, $\boldsymbol{u} = T(\boldsymbol{x})$ are standard normal variables, $T : \mathbb{R}^d \mapsto \mathbb{R}^d$ maps variables $\boldsymbol{x}$ from the

original state space to the SNS, and $\Phi(\boldsymbol{u})$ is the standard normal CDF. Note that all the variables have to be transformed into the SNS, via $T : \mathbb{R}^d \mapsto \mathbb{R}^d$, in order for the method to function, as the method makes use of the geometric feature of the SNS. For example, in this space the norm of a point represents the so-called reliability index, which quantifies how many standard deviations that point is away from the median state in the original space. Eq. (3.1) can be written in the form

$$p_F = \int_{\mathbb{R}^{d-1}} \left(\int_{-\infty}^{\infty} \mathcal{I}_F(\boldsymbol{u}) \phi(u_1) du_1 \right) \prod_{i=2}^{d} \phi(u_i) du_i; \tag{3.2}$$

for convenient evaluations. With u_1 pointing orthogonally towards the failure domain, the expansion $w(\boldsymbol{u}_{2:d}) = \int_{-\infty}^{\infty} \mathcal{I}_F(\boldsymbol{u})\ \phi(u_1)\ du_1$ of Eq. (3.2) is a function of the $d-1$ remaining standard normal variables $\boldsymbol{u}_{2:d} \in \mathbb{R}^{d-1}$ and provides a measure of likelihood for the variable $\boldsymbol{u}_{2:d}$ to be in the failure domain. All the points with coordinates $\boldsymbol{u}^{\perp} = \{0, \boldsymbol{u}_{2:d}\}$ lie on the hyperplane orthogonal to the first coordinate u_1. Variable w can be calculated as $w\left(\boldsymbol{u}_{2:d}\right) = \Psi(F_1)$, where $F_1 = \{u_1 \in \mathbb{R} \mid \mathcal{G} \leqslant 0\}$, and $\Psi(A) = \int_{-\infty}^{\infty} \mathcal{I}_A(u)\phi(u)du$ is the Gaussian measure of any subset $A \subset \mathbb{R}$. Let the scalar c^* be the smallest (in magnitude) value of the coordinate u_1 such that

$$c^* = \min\left\{u_1 \in \mathbb{R} |\ \mathcal{I}_F(\boldsymbol{u}) = 1\right\}; \tag{3.3}$$

then, w can be approximately calculated as $w\left(\boldsymbol{u}_{2:d}\right) = \Phi(-|c^*|)$. Therefore, the failure probability can be obtained as the expected value

$$p_F = E[w\left(\boldsymbol{u}_{2:d}\right)] = \int_{\mathbb{R}^{d-1}} w\left(\boldsymbol{u}_{2:d}\right) \prod_{i=2}^{d} \phi(u_i) du_i. \tag{3.4}$$

Note that considering the standard normal CDF, $\Phi(-|c^*|)$, in place of the Gaussian measure, $\Psi(F_1)$, the probability, w, can only be overestimated, because it assumes that no further *survival* regions can be found on the line beyond c^*. LS provides an estimation of $E[w]$ by repeatedly generating points $\boldsymbol{u}_{2:d}$ from the standard normal PDF in $\mathbb{R}^{d-1}$, and computing the respective partial probabilities $w\left(\boldsymbol{u}_{2:d}\right)$. For example, generating N_L points (lines) $\boldsymbol{u}_{2:d}^{\{j\}},\ j = 1, 2, .., N_L$, an estimate of the failure probability is obtained computing the average

$$\hat{p}_F = \frac{1}{N_L} \sum_{j}^{N_L} w(\boldsymbol{u}_{2:d}^{\{j\}}). \tag{3.5}$$

The above approach, can be applied by orienting the important direction $\boldsymbol{a}$ as the coordinate u_1. The integral of Eq. (3.4) is calculated, in practice, by exploiting the geometric features of the SNS. Standard normal points on the hyperplane orthogonal to $\boldsymbol{a}$ can be obtained from any generated standard normal point $\boldsymbol{u}$ as follows $\boldsymbol{u}_a^{\perp} = \boldsymbol{u} - (\boldsymbol{u} \cdot \boldsymbol{a})\boldsymbol{a}$. This is equivalent to operating in a rotated space, where the first coordinate

is oriented as the important direction. In this way, the search for the limit state, for each random point (line) $\{j\}$, can be set as $\boldsymbol{u}_a^{\{j\}}(c) = \boldsymbol{u}_a^{\perp\{j\}} + c\ \boldsymbol{a}$, where the scalar c controls the location of the points along the line $\{j\}$.

Standard implementation of LS operates with a fixed, initially determined important direction $\boldsymbol{a}$. For each random point $\boldsymbol{u}^{\{j\}}$, the distance from the hyperplane to the performance function in the direction of $\boldsymbol{a}$ is identified searching along the lines $\boldsymbol{u}_a^{\{j\}}(c)$. Moreover, in standard LS the line search is conducted evaluating the performance function $\mathcal{G}$ on the support sequence $\boldsymbol{c} = \{c_1, ..., c_{N_c}\}$, to find the value c^* by means of interpolation, usually requiring from 6 to 8 model evaluations per line.

3.1.2 Adaptive algorithm

An adaptive version of Line Sampling is developed in OpenCossan to further improve the numerical efficiency of LS [1]. The improvement concerns the efficiency for evaluating Eq. (3.5). The adaptive algorithm uses a support sequence $\boldsymbol{c}$ that is dynamically generated to adapt to the shape of the limit state surface. This makes the algorithm capable of recognizing the level of non-linearity of the performance function. Moreover, it allows for variations in the limit state, being capable of identifying new important directions. Hence, only a very rough estimation of the important direction is required at the start of the simulation.

The main features of the algorithm are: (i) minimise the number of samples along the lines $\{j\}$ to identify $c^{*\{j\}}$; (ii) adapt the important direction to the shape of the limit state surface. The first feature is achieved developing an efficient line search and selection procedures. The second feature is achieved computing weights to each working direction. The algorithm operates setting an (initial) important direction $\boldsymbol{a}$ and generating a number, N_L, of points $\boldsymbol{u}_a^{\{j\}}$. Form each of the points, $\boldsymbol{u}_a^{\{j\}}$, a line is constructed. The first line j is deployed from the origin as $\boldsymbol{u}_a^{\{0\}}(c) = c\ \boldsymbol{a}$. A line search procedure, based on a Newton-Raphson iterative procedure, is applied to identify the root $c^{*\{j\}}$, which is then used to compute the partial probability $p_F^{\{j\}} = w(\boldsymbol{u}_a^{\{j\}}) = \Phi(-|c^{*\{j\}}|)$. Using the identified root, the procedure is repeated as $\boldsymbol{u}_a^{\{j\}}(c_0) = \boldsymbol{u}^{\perp\{j\}} + c^{*\{j-1\}}\ \boldsymbol{a}$, until every line is processed. To increase the efficiency, the algorithm does not process the lines randomly as they are generated. The lines are selected according to a criterion based on the metric space that recognizes the nearest line to one being currently processed. Hence, in case of slightly non-linear limit state surface, the distances $c^{*\{j\}}$ and $c^{*\{j-1\}}$, for lines j and $j-1$ respectively, are expected to have approximately the same value. To identify the nearest line, the index of the line closest to the origin is computed as $k_1 = \arg\min_j \left\|\boldsymbol{u}^{\perp\{j\}} - 0\right\|$. Subsequently, all the other indexes are calculated as $k_{i+1} = \arg\min_{j \neq k_i} \left\|\boldsymbol{u}^{\perp\{j\}} - \boldsymbol{u}^{\perp\{k_i\}}\right\|$, as also illustrated in the pseudo code of the algorithm in Figure 3.1.

begin
$\alpha = \alpha_1$; % set initial direction
$u^{\{j\}_1^N} \sim \mathcal{N}(0,1)$;
$u^{\perp\{j\}_1^N} = u^{\{j\}_1^N} - (u^{\{j\}_1^N} \cdot \alpha)\ \alpha$;
$k_1 = \min_j \left\| u^{\perp\{j\}} - 0 \right\|$ % get the first line index
find c° such that $\mathcal{G}(T(c^\circ\ \alpha)) = 0$;
$c_0 = c^\circ$; % initialize distance from hyperplane
for $i = 1 \rightarrow N$ **do**
  $u_\alpha^{\{k_i\}}(c_0) = u^{\perp\{k_i\}} + c_0\ \alpha$;
  find c^* such that $\mathcal{G}(T(u_\alpha^{\{k_i\}}(c^*)) = 0$;
  $k_{i+1} = \min_{j \neq k_{1,\ldots,i}} \left\| u^{\perp\{j\}} - u^{\perp\{k_i\}} \right\|$; % get the next line index
  $c_0 = c^*$;
  $p_F^{\{i\}} = \Phi(-|c^*|)$; % compute partial probability
  if $||u_\alpha^{\{k_i\}}(c^*)|| < c^\circ$ **then**
    $c^\circ = ||u_\alpha^{\{k_i\}}(c^*)||$;
    $\alpha = u_\alpha^{\{k_i\}}(c^*)/c^\circ$; % update direction
  end if
end for
$\hat{p}_F = \frac{1}{N} \sum_j^N p_F^{\{j\}}$; % failure probability
end

Figure 3.1: Pseudocode of the Adaptive Line Sampling algorithm

3.1.3 Adaptation of the important direction

The adaptive Line Sampling algorithm allows it to change the important direction without re-evaluating the performance function along the processed lines. This feature is useful when there is only little evidence of the optimal important direction, so that an approximate direction can be set at the beginning of the simulation and a better direction can be obtained during the simulation. An optimal important direction generally provides a more accurate estimate of the failure probability and it is usually associated with the design point $\tilde{\boldsymbol{u}}^* = \min\left\{||\boldsymbol{u}|| : \boldsymbol{u} \in \mathbb{R}^d\ \ \mathcal{I}_F(\boldsymbol{u}) > 0\right\}$, i.e. the point on the limit state that carries the highest probability density. A new important direction can be obtained as soon as a more probable point is identified on the limit state $\tilde{\boldsymbol{u}}_a^{\{j\}}$, such that $||\tilde{\boldsymbol{u}}_a^{\{j-1\}}|| > ||\tilde{\boldsymbol{u}}_a^{\{j\}}||$, where the new direction is set as $\boldsymbol{\alpha}_{new} = \tilde{\boldsymbol{u}}_a^{\{j\}}/||\tilde{\boldsymbol{u}}_a^{\{j\}}||$. Note that changing the important direction does not affect the expected value of the failure probability, however, an improvement of the important direction reduces the variance of the estimation. An insight on how the adaptation of direction works is provided in Figure 3.2, where directional updates are represented in the original state space $\mathcal{X}$. In the example of Figure 3.2 an approximate direction is set to start the simulation. In Figure 3.2 it can also be appreciated how the algorithm converges toward the optimal direction after only 4 updates, requiring 5 lines for the first and second update, 2 lines

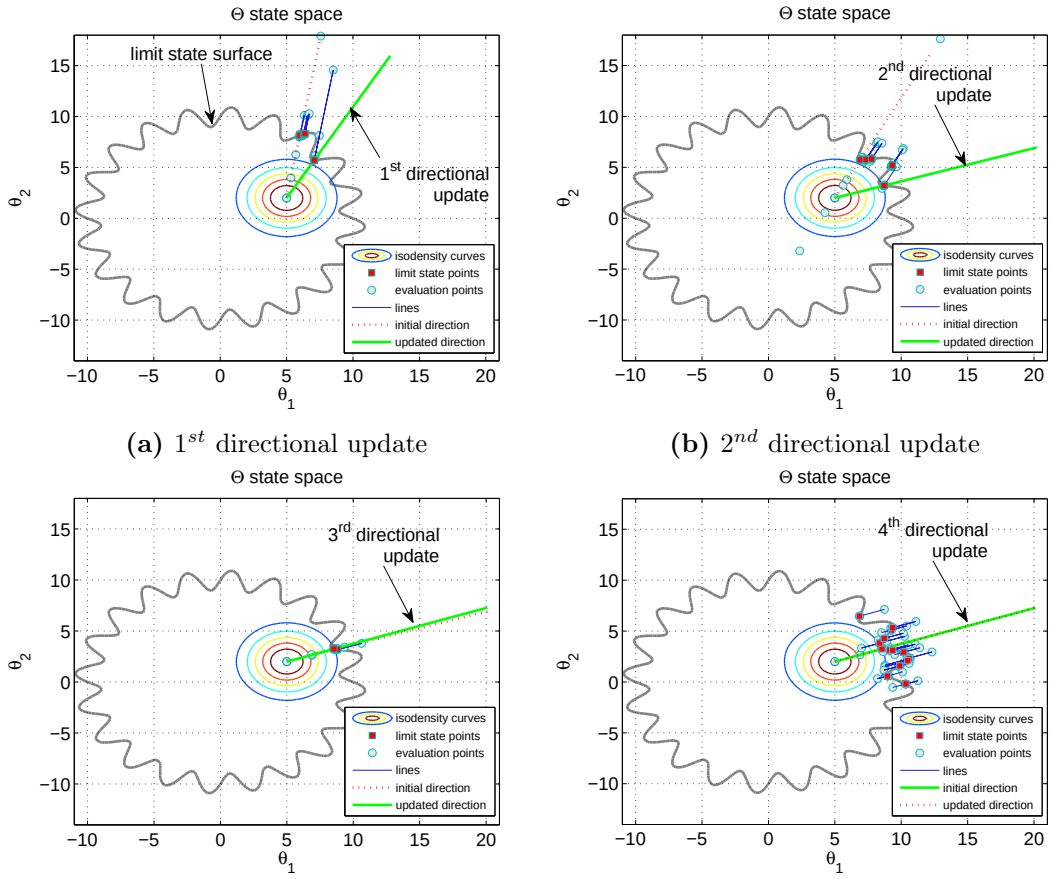

(a) 1^{st} directional update

(b) 2^{nd} directional update

(c) 3^{rd} directional update

(d) 4^{th} directional update

Figure 3.2: Directional change in the (original) state space obtained by means of ALS on the limit state defined by the performance function: $g(\boldsymbol{x}) = -(x_1 + x_2) + d^2\ (1 + a\ \sin(b\ \tan^{-1}(x_1, x_2)))$, where $x_1 \sim N(5, 2^2)$, $x_2 \sim N(2, 2^2)$, $d = 10$, $a = 0.2$ and $b = 20$.

for the third update and 15 lines for the last update.

3.1.4 Efficiency and accuracy

Adaptive Line Sampling shows an improvement in efficiency and accuracy superior to the standard version. This is elucidated in a comparative study with a reference solution obtained by direct Monte Carlo simulation. An explicit performance function is used to test the methods, which is expressed as $g(\boldsymbol{x}) = -\sqrt{\boldsymbol{x}^T\boldsymbol{x}} + a$, where $\boldsymbol{x}$ are N_{RV} independent normal random variables and a is a constant. First, the test is run with just two random variables, but with decreasing probability targets, by selecting different values of a in the performance function g, as shown in Table 3.1.

Note that, in this case, the values of probability $p_F = \Phi(-\beta)$ obtained by First Order Reliability Method [15] are not trustworthy because of the concave shape of the limit state surface. An illustration of the performance of the methods is shown in Figure 3.3a, where the number of required samples from LS and ALS is compared

Table 3.1: Advanced Line Sampling efficiency tests run on the performance function $g(\boldsymbol{x}) = -\sqrt{x_1^2 + x_2^2} + a$, reference solution is obtained via MC (10^6 samples).

$g(\boldsymbol{x}) = -\sqrt{x_1^2 + x_2^2} + a$; $x_1 \sim N(5, 2^2)$, $x_2 \sim N(2, 2^2)$; $a = \{10, 10.2, 10.5, 12, 14, 16\}$								
	Direct Monte Carlo		Adaptive Line Sampling			Line Sampling		
β (c°)	$\hat{p}_F$	CoV (10^{-2})	$\hat{p}_F$	CoV (10^{-2})	Ns	$\hat{p}_F$	CoV	Ns
2.307	$1.49\ 10^{-2}$	$0.8\ 10^{-2}$	$1.35\ 10^{-2}$	6.0	63	$1.32\ 10^{-2}$	5.5	210
2.407	$1.16\ 10^{-2}$	$0.9\ 10^{-2}$	$1.08\ 10^{-2}$	10.8	66	$9.75\ 10^{-3}$	5.4	210
2.557	$7.40\ 10^{-3}$	$1.1\ 10^{-2}$	$6.60\ 10^{-3}$	4.5	67	$7.00\ 10^{-3}$	5.8	210
3.304	$7.06\ 10^{-4}$	$3.8\ 10^{-2}$	$6.58\ 10^{-4}$	9.2	65	$6.69\ 10^{-4}$	13.6	210
4.307	$1.42\ 10^{-5}$	$26.5\ 10^{-2}$	$1.23\ 10^{-5}$	13.9	59	$1.18\ 10^{-5}$	8.3	210
5.307	–	–	$9.18\ 10^{-8}$	12.4	64	$10.14\ 10^{-8}$	14.0	210

Table 3.2: Adaptive Line Sampling efficiency tests run on the performance function $g(\boldsymbol{x}) = -\sqrt{\boldsymbol{x}^T\boldsymbol{x}} + a$. and reference solution obtained via MC (10^6 samples).

$g(\boldsymbol{x}) = -\sqrt{\boldsymbol{x}^T\boldsymbol{x}} + a$; $x_i \sim N(2, 1)$; $a = \{7.0, 9.3, 14.7, 18.1, 24.8, 34.0, 52.5\}$									
		Direct Monte Carlo		Adaptive Line Sampling			Line Sampling		
N_{RV}	β (c°)	$\hat{p}_F$	CoV (10^{-2})	$\hat{p}_F$	CoV (10^{-2})	Ns	$\hat{p}_F$	CoV (10^{-2})	Ns
4	3.000	$3.27\ 10^{-3}$	1.75	$3.52\ 10^{-3}$	19.7	94	$2.75\ 10^{-3}$	7.2	215
10	2.975	$8.37\ 10^{-3}$	1.10	$6.97\ 10^{-3}$	11.1	102	$8.57\ 10^{-3}$	16.9	221
30	3.745	$4.56\ 10^{-3}$	1.48	$4.13\ 10^{-3}$	12.9	120	$4.27\ 10^{-3}$	15.6	241
50	3.958	$7.44\ 10^{-3}$	1.15	$7.87\ 10^{-3}$	17.8	144	$7.59\ 10^{-3}$	16.5	261
100	4.800	$4.87\ 10^{-3}$	1.43	$5.27\ 10^{-3}$	17.5	222	$5.92\ 10^{-3}$	19.7	311
200	5.716	$5.85\ 10^{-3}$	1.30	$5.20\ 10^{-3}$	18.3	323	$6.16\ 10^{-3}$	17.0	411
500	7.778	$4.15\ 10^{-3}$	1.55	$3.44\ 10^{-3}$	21.4	619	$3.56\ 10^{-3}$	17.8	711

to direct MC obtained analytically using a fixed value of $CoV = 10^{-2}$. The analytic number of samples required by direct MC, denoted by N_{MC}, can be obtained as $N_{MC} = (1 - p_F)/(CoV^2 \cdot p_F)$, where p_F is the target failure probability. A satisfactory level of accuracy (CoV = $5 \cdot 10^{-2}$) is achieved with just 65 samples using ALS, compared to a necessary sample size of 210 samples using LS. The second test is run fixing the probability targets (approximately to 10^{-3}), while progressively increasing the number of random variables, as shown in Table 3.2. The results of the second test, as illustrated in Figure 3.3b, show that Monte Carlo is, as expected, insensitive to the number of variables. Line Sampling methods require significantly fewer samples to achieve the same level of accuracy of MC. The slight increase in samples number with the number of variables in Figure 3.3b is due to the calculation of gradient used to initialise the important direction. As expected, in this second test, the probability of failure computed with the First Order Reliability Method is inaccurate, as also shown in Table 3.2. In both cases, Adaptive Line Sampling has shown not only to be accurate but also to be 3 or 4 times more efficient than Line Sampling.

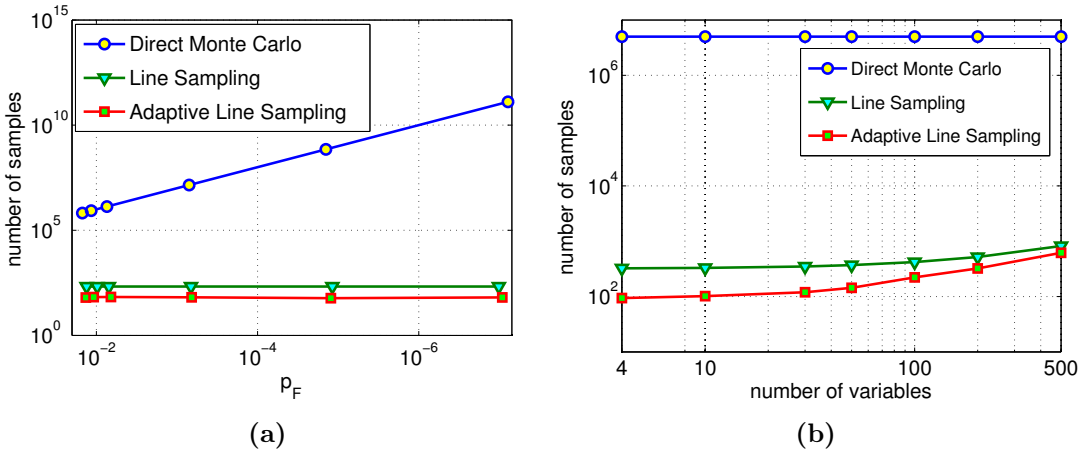

Figure 3.3: Number of samples required from ALS and LS compared to direct MC (a) for decreasing probability target, and (b) for increasing dimension. Here results from direct MC are obtained fixing the $CoV = 0.01$.

3.2 Chapter summary

In this chapter, both standard and adaptive implementation of Line Sampling have been presented. The advantage of using the adaptive implementation, in terms of efficiency and accuracy, has been shown by means of a numerical example. The need for an adaptive version of the algorithm is motivated by the fact that the accuracy of the estimation is quite sensitive to the chosen direction. With the added feature of direction adaptation the algorithm selects better directions as the simulation proceeds, converging to a better accuracy, which is quantified by means of the estimator variance. The developed adaptive algorithm has also the additional feature of adapting to the shape of the limit state surface, so that if the surface is approximately a plane, within a sufficiently small neighbour of a point, the algorithm requires very few samples (from 2 to 4) per line to complete the analysis. With the latter feature if the limit state surface is a hyperplane only one sample per line is required and the estimation is exact. However, it has to be noted that in order for the estimation to be exact the limit state surface has to be a hyperplane in the Standard Normal Space, which is the case only for Gaussian distributions. The adaptive feature of Line Sampling makes it particularly suited to cope with situations involving Random Sets and imprecise probabilities. Directional changes are required to switch from a distribution function to another, as required by imprecise probability, thus, the adaptive feature adds continuity to the process of assessing lower and upper probability bounds. The advantage of using Adaptive Line Sampling within the confines of imprecise probability will be shown in the next two chapters.

Chapter 4

Efficient Double Loop Approach for Reliability Estimation: Application to Finite Element Model

A numerical strategy for the efficient estimation of set-valued failure probabilities, coupling Advanced Line Sampling with optimisation methods, is presented in this chapter. The Double Loop approach is implemented in opposition to the Random Set approach, where the inner loop estimates the failure probability by means of Line Sampling, and the outer loop selects two candidates in the epistemic space corresponding to the lower and upper probability bounds, as depicted in Figure 4.1. The proposed strategy knocks down the computational barrier of computing interval failure probabilities, and reduces the cost of a robust reliability analysis by orders of magnitude. The efficiency and applicability of the developed method is demonstrated via numerical examples. The solution strategy is integrated into the open-source software for uncertainty quantification and risk analysis OpenCossan [1], allowing its application on large-scale engineering problems (see also [21]).

4.1 Introduction

The proposed strategy implements a double loop approach, thus, the generalised model includes *parametric* p-boxes, intervals and CDFs. This comes with the only limitation that a parental distribution model has to be defined for the probability distributions. Dependency among variables are accounted for by means of a *copula* function $C : [0,1]^d \rightarrow [0,1]$.

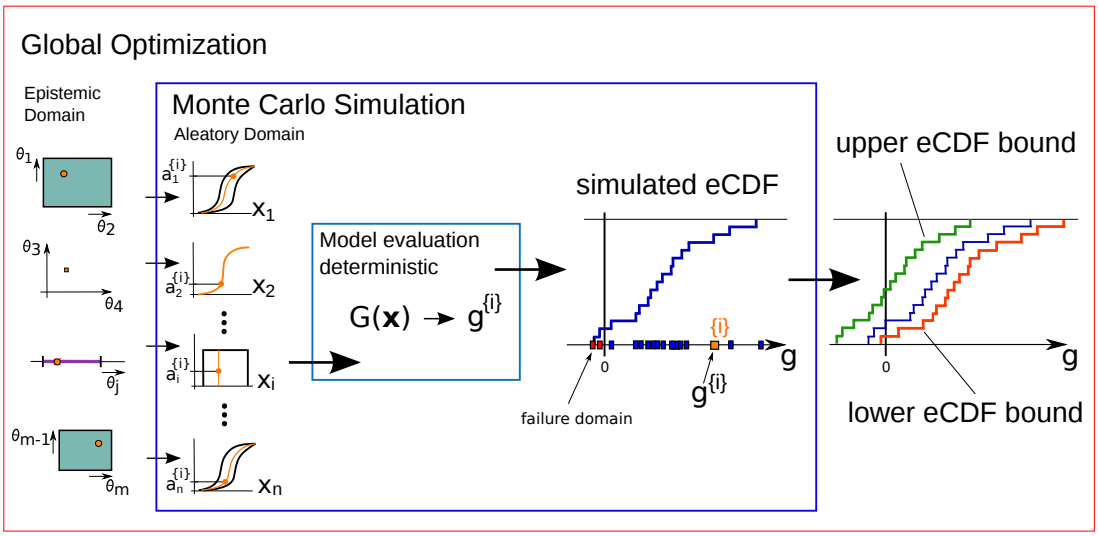

Figure 4.1: Forward propagation with the Double Loop approach

4.2 Credal Sets and Epistemic Domain

Within the epistemic domain, $\boldsymbol{\Theta}$, the interval hyper-parameters, $\underline{\overline{\boldsymbol{\theta}}}$, are responsible for the imprecision in the p-boxes as they produce the set of distribution functions

$$\mathcal{C} = \left\{ C\left(F_{X_1}(x_1;\boldsymbol{\theta}_1), \ldots, F_{X_d}(x_d;\boldsymbol{\theta}_d)\right) : \underline{\boldsymbol{\theta}}_i \leqslant \boldsymbol{\theta}_i \leqslant \overline{\boldsymbol{\theta}}_i,\ i = 1, \ldots, d \right\}; \tag{4.1}$$

where, C is a copula function, and $F_{X_i}(x_i;\boldsymbol{\theta}_i)$ is a cumulative distribution function of variable x_i, which hyper-parameters are $\boldsymbol{\theta}_i \in \times_{i=1}^{d} \underline{\overline{\boldsymbol{\theta}}}_i \equiv \boldsymbol{\Theta}$. The set of Eq. (4.1) is referred to as Credal set [77].

For convenience, the epistemic domain, $\boldsymbol{\Theta}$ is split into two, to distinguish between interval hyper-parameters, $\boldsymbol{\Theta}_h$ and interval system parameters $\boldsymbol{\Theta}_x$, thus, the epistemic space is the product space $\boldsymbol{\Theta} \equiv \boldsymbol{\Theta}_h \times \boldsymbol{\Theta}_x$.

4.2.1 Reliability assessment of engineering systems

In performance-based engineering the system is considered as a collection of performance variables $g_i, i = 1, 2, ..., N_g$, which are functions of the state variables $\boldsymbol{x} \in \mathcal{X} \subseteq \mathbb{R}^d$ only (see e.g. [69]). For instance, the state variables $\boldsymbol{x}$ are the inputs that define a structural system, such as material properties, shape and size of structural elements, load magnitudes, etc., whereas the performances express specific structural responses, such as amplitude or frequency of vibrations, stress, deflection and so forth.

The performance function $\mathcal{G} : \mathcal{X} \mapsto g_i \in \mathbb{R}$ maps values from the state space $\mathcal{X}$ to the performance variables of interest. For given criteria on the performance variables, $\mathcal{G}$ defines the *failure* domain as

$$\mathcal{X}_F = \left\{ \boldsymbol{x} \in \mathcal{X} \subseteq \mathbb{R}^d \mid \mathcal{G}(\boldsymbol{x}) \leqslant 0 \right\}; \tag{4.2}$$

which is featured by the limit state surface $\tilde{\mathcal{X}} = \{\boldsymbol{x} \mid \mathcal{G}(\boldsymbol{\theta}) = 0\}$. Note that the definition of Eq. (4.2) implies that the performance function is defined as the difference between *capacity* and *demand*, where the capacity is typically the structural quantity threshold while the demand is the response of the system. Failure happens if the structural response is beyond the threshold, as the difference between capacity and demand will be less than zero. Note that both capacity and demand can be state (uncertain) variables of the system.

Reliability is assessed as $R = 1 - \mathrm{P}_X[\boldsymbol{x} \in \mathcal{X}_F]$, where its complement $\mathrm{P}_X[\boldsymbol{x} \in \mathcal{X}_F]$ is the failure probability. Points $\tilde{\boldsymbol{x}} \in \tilde{\mathcal{X}}$ on the limit state hyper-surface are also called (limit) state points. An important feature for subsequent development is that the limit state $\tilde{\mathcal{X}}$ is invariant to the Credal Set $\mathcal{C}$, because $\tilde{\mathcal{X}}$ is intrinsic in the structural system, i.e. depends solely on the performance function $\mathcal{G}$. The uncertainty model only determines the probability over the state space, but does not influence location of the state points $\tilde{\boldsymbol{x}}$.

4.2.2 Failure probability for generalized uncertainty models

When the uncertainty model includes only precisely defined probability distributions, thus, the true uncertainty model is known, as $\boldsymbol{\theta}^* \equiv \boldsymbol{\Theta}$, structural reliability is assessed in terms of *precise* failure probability, obtained as

$$p_F = \int_{\mathcal{H} \leqslant 0} \mathcal{H}(\boldsymbol{\alpha}; \boldsymbol{\theta}^*) \ \mathrm{d} \ \ (\boldsymbol{\alpha}); \tag{4.3}$$

where $\mathrm{C}(\boldsymbol{\alpha})$ is the Stieltjes-Lebesgue measure corresponding to the *copula* C, and $\mathcal{H} : \boldsymbol{\Omega} \times \boldsymbol{\Theta} \mapsto \mathbb{R}$ is the system function $\mathcal{H} = \mathcal{W} \circ \mathcal{G}$. When the epistemic space is not a singleton, i.e. for example $\overline{\underline{\boldsymbol{\theta}}} \equiv \boldsymbol{\Theta}$, lower and upper failure probability bounds are obtained as

$$\overline{p}_F = \sup_{\boldsymbol{\theta} \in \boldsymbol{\Theta}} \int_{\mathcal{H} \leqslant 0} \mathcal{H}(\boldsymbol{\alpha}; \boldsymbol{\theta}) \ \mathrm{d} \ \mathrm{C}(\boldsymbol{\alpha}); \tag{4.4}$$

$$\underline{p}_F = \inf_{\boldsymbol{\theta} \in \boldsymbol{\Theta}} \int_{\mathcal{H} \leqslant 0} \mathcal{H}(\boldsymbol{\alpha}; \boldsymbol{\theta}) \ \mathrm{d} \ \ \mathrm{C}(\boldsymbol{\alpha}). \tag{4.5}$$

From Eq. (4.4) and (4.5) of lower and upper probability, it follows that $\underline{p}_F \leqslant \overline{p}_F$. When the Credal set $\mathcal{C}$ degenerates into a single probability distribution function, precise probabilities $p_F = \underline{p}_F = \overline{p}_F$ are obtained.

4.2.2.1 Conjugate relationship between lower and upper bounds of probability

Upper and lower bounds of failure and survival probabilities show a dual relationship. This can be seen clearly in the special case that the uncertainty model is restricted to a Credal set only, where the variables are independent. The optimal probability

distribution $F^{\mathrm{L}}_{\boldsymbol{x}}(\boldsymbol{x}) = F^{\mathrm{L}}_{X_1,\ldots,X_d}(x_1,\ldots,x_d)$, that yields the lower bound $\underline{p}_f$, satisfies the equation

$$\int_{\mathcal{X}_F} \mathcal{H}(\boldsymbol{\alpha};\boldsymbol{\theta}^{\mathrm{L}})\ \mathrm{d}F^{\mathrm{L}}(\boldsymbol{x}) + \int_{\mathcal{X}_S} \mathcal{H}(\boldsymbol{\alpha};\boldsymbol{\theta}^{\mathrm{L}})\ \mathrm{d}F^{\mathrm{L}}(\boldsymbol{x}) = 1; \tag{4.6}$$

where, $\mathcal{X}_S$, is the *survival* domain such that $\mathcal{X}_S \cup \mathcal{X}_F = \mathcal{X}$ and $\mathcal{X}_S \cap \mathcal{X}_F = \varnothing$. Note that from Eq. (4.6) follows that a *conjugate* (or dual) relationship between lower and upper probability functions can be established, as $F^{\mathrm{L}}_{\boldsymbol{x}}(\boldsymbol{x})$ is also the distribution function for which the upper bound, $\overline{p}_S$, is obtained being

$$\overline{p}_S = \int_{\mathcal{X}_S} \mathcal{H}(\boldsymbol{\alpha};\boldsymbol{\theta}^{\mathrm{L}})\ \mathrm{d}F^{\mathrm{L}}(\boldsymbol{x}). \tag{4.7}$$

However, the complete function, $F^{\mathrm{L}}_{\boldsymbol{x}}(\boldsymbol{x})$, which may also have an infinite support, is needed in order for the relationship to be used.

4.3 Sampling-based estimation of set-valued reliability

To calculate the bounds of the failure probability, a global search in the epistemic domains $\boldsymbol{\Theta}_h$ and $\boldsymbol{\Theta}_x$ is required. A naive approach to the problem is prohibitive in the majority of cases due to the high numerical effort. In fact, a double loop approach has to be adopted, where the inner loop estimates the failure probability and the outer loop searches for the bounds of the probability. The ALS method is utilized to speed up the computation of (precise) failure probabilities, and to ease the search procedure for lower and upper failure probabilities.

4.3.1 The global search for lower and upper failure probabilities

The objective function for the global search in $\boldsymbol{\Theta}_h$ and $\boldsymbol{\Theta}_x$ is the failure probability estimate $\hat{p}_F$. The search can be seen as an iterative procedure that, after some steps, converges towards the sought lower and upper failure probability bounds.

4.3.1.1 The search in the bounded domain of hyper-parameters $\boldsymbol{\Theta}_h$

Let the search for the failure probability bounds be restricted to the domain $\boldsymbol{\Theta}_h$ only. Hence, $\boldsymbol{\Theta}_h$, defines the set of all probability distributions functions to be considered in the analysis. Although any element of $\boldsymbol{\Theta}_h$ is associated with a different value of failure probability, the limit state does not change as we search in $\boldsymbol{\Theta}_h$. This is because the limit state depends upon the structural system and not upon the uncertainty model (Credal set), $\mathcal{C}$, that defines the probability distributions over the state variables.

Since the important direction is defined as any direction pointing towards the failure domain, during the search in $\boldsymbol{\Theta}_h$, an approximate $\boldsymbol{a}$ can be set for the entire analysis, independently from the distribution functions of the random variables. However, chang-

ing the distribution functions modifies the location of the most probable point on the limit state surface. Hence, the direction $\boldsymbol{a}$, set at beginning of the analysis, might not be the optimal one for all the distributions analysed. This motivates the implementation of an adaptive algorithm capable of searching and updating new optimal directions, as shown in Section 3.1.

Each step of the search procedure requires the estimation of a failure probability. Using conventional sampling approaches a new (independent) simulation must be performed to estimate each of these failure probabilities. However, the proposed strategy allows it to combine results from different simulations to increase the efficiency of the procedure. This is possible noting that points in the SNS, $\boldsymbol{u}$, depend on $\boldsymbol{\Theta}_h$ through the transformation T only, and therefore the corresponding points $\boldsymbol{x}$ in the original state space are independent of $\boldsymbol{\Theta}_h$.

Since the limit state does not change as we search in $\boldsymbol{\Theta}_h$, any point $\tilde{\boldsymbol{u}}$ on the limit state can be transformed back onto the original space, and then re-mapped to the SNS for the next simulation. When a new simulation is deployed, the standard points on the limit state $\tilde{\boldsymbol{u}}$, previously found, can be used (i) to determine an accurate initial important direction and (ii) to compute an approximate estimation of the failure probability bounds. Making use of the state points collected during previous simulations, an accurate initial direction can be obtained orienting $\boldsymbol{a}$ towards the region of the space with the highest probability density. On the other side, an approximation of the failure probability bounds can be obtained processing the collected state points. Let $\boldsymbol{a}_i$ denote the direction of the current simulation and $\boldsymbol{a}_{i-1}$ the direction of the previous simulation. Let T_i and T_{i-1} be the transformation functions of simulation i and $i-1$ respectively. Standard points from simulation i can be obtained mapping standard points from simulation $i-1$ onto the original space, as $\boldsymbol{x} = T_{i-1}(\boldsymbol{u})$, and then re-mapping them back onto the standard space of the next simulation as $\boldsymbol{u}^{remap} = T_i^{-1}(T_{i-1}(\boldsymbol{u}))$, where T^{-1} denotes the inverse transformation, T. At the current simulation, the failure probability

$$p_{F(i)} = \int_{\mathbb{R}^{d-1}} w(\boldsymbol{u}_{a_i}^{\perp})\ f_U(\boldsymbol{u}_{\alpha_i}^{\perp})\ du^{d-1} \tag{4.8}$$

can be computed using the limit state points $\tilde{\boldsymbol{u}}^{remap}$ obtained from previous simulations. However, these points are no longer drawn from a probability distribution. Therefore, in order to be able to compute the failure probability, an *importance* probability density function h_U is built to model the re-mapped state points. The density function h_U has a multi-modal distribution with density peaks centred on the re-mapped points and weighed using the metric properties of the SNS. An approximation of the failure probability can then be obtained as

$$p_{F(i)} = \int_{\mathbb{R}^{d-1}} w(\boldsymbol{u}_{a_i}^{\perp\text{remap}})\ h_U(\boldsymbol{u}_{a_{i-1}}^{\perp}) \frac{f_U(\boldsymbol{u}_{a_i}^{\perp\text{remap}})}{h_U(\boldsymbol{u}_{a_{i-1}}^{\perp})}\ du^{d-1}. \tag{4.9}$$

By means of the importance sampling ratio $q = f_U(\boldsymbol{u}_{a_i}^{\perp\text{remap}})/h_U(\boldsymbol{u}_{a_{i-1}}^{\perp})$, the probability $p_{F(i)}$ can now be computed using the points from (previous) simulation $i-1$ as

$$\tilde{p}_{F(i)} = \frac{1}{N_L}\sum_{j}^{N_L} q^{\{j\}}\ w(\boldsymbol{u}_{a_i}^{\perp\text{remap}\{j\}}) = \frac{1}{N_L}\sum_{j}^{N_L} q^{\{j\}}\ w(T_i^{-1}(T_{i-1}(\boldsymbol{u}_{\alpha_{i-1}}^{\perp\{j\}}))), \tag{4.10}$$

where, $q^{\{j\}}$ denotes the weighing ratio obtained on line j, and N_L is the number of simulated lines.

4.3.1.2 The search in the bounded domain of structural parameters $\boldsymbol{\Theta}_x$

Imprecision of structural parameters, characterized by $\boldsymbol{\Theta}_x$, requires an extension of the procedure developed so far. In fact, the bounded variables, $\boldsymbol{x} \in \boldsymbol{\Theta}_x$, change the shape of the limit state boundary, which needs to be addressed with a simultaneous second search, tied to the search in $\boldsymbol{\Theta}_h$. The proposed strategy takes advantage of an augmented probability space, where the interval variables are transformed into dummy normal random variables having an interval mean value and a fixed arbitrary standard deviation. In simple terms, this permits a combined consideration of the bounded domain $\boldsymbol{\Theta}_x$ together with $\boldsymbol{\Theta}_h$. Each dummy imprecise random variable is defined with an interval mean value $\underline{\overline{\mu_x}} = \overline{\underline{x}}$, and a real-valued standard deviation σ_x to be fixed with some convenient value. The only requirement for the value of σ_x is that it should neither be too large nor be too small, to avoid numerical issues in computing the failure probability. The standard deviation σ_x can be set, for example, as a fraction of the interval radius $\sigma_x = \frac{1}{k}\ (\overline{x} - \underline{x})/2$, where, $k \in \mathbb{N}$ can be any positive integer. By defining these dummy imprecise random variables, a thorough search can be performed in both domains $\boldsymbol{\Theta}_h$ and $\boldsymbol{\Theta}_x$ simultaneously. The failure probability bounds are computed on the found argument optima. Note that during the global search, sampling outside the intervals may occur. However, points outside the intervals are solely used to drive the search process. In cases where the physical model restricts the evaluation to the range of the intervals, truncated normal random variables can be used, where lower and upper limits are equal to the endpoints of the intervals. Two additional reliability analyses at the end of the search, run on the argument optima, are needed to estimate the failure probability bounds.

When the limit state surface is only slightly non-linear the search procedure can be far more efficient. In fact, in this case the important directions in the original space are all oriented towards the same region of the state space. This implies that, as we search in $\boldsymbol{\Theta}_h$ and $\boldsymbol{\Theta}_x$, the coordinates of the important directions do not significantly change. Therefore, the important direction in the original space can be used to identify those (conjugate) states in the SNS that are the nearest and furthest from the limit state surface. Here, the state that is the nearest to the limit state surface (also called upper

conjugate state), is also where the failure probability has its maximum; whereas the furthest state from the limit state surface (also called lower conjugate state), is where the failure probability has its minimum.

4.3.2 Applicability of the strategy

The proposed strategy is generally applicable. It enables computation of the failure probability in high dimensional spaces, i.e. when a large, albeit finite, number of random variables are present. Moreover, the efficiency of the strategy is independent of the magnitude of the failure probability, as shown in Figure 3.3a, which makes it particularly suitable for the reliability assessment of large safety-critical systems. Although the approach is applicable to estimate the failure probability of any system, it is particularly efficient when the limit state surface is moderately non-linear (i.e. the performance functions do not show repetitive narrow spikes). In engineering practice, this applies to the majority of problems, as shown in [24], hence the proposed approach seems particularly promising to solve real-case examples.

In case of systems characterized by a large number of failure modes, the algorithm can be adopted to efficiently estimate the failure probability associated to each failure mode. Then, the individual failure probabilities can be combined to calculate the probability of failure of the entire system (i.e. calculating the conditional failure probability).

The approach is particularly efficient to support the estimation of the probability bounds associated to the representation of the uncertainty as intervals or fuzzy variables with no restrictions in terms of dimension. In fact, the method is able to deal with any finite number of intervals and fuzzy variables, as also shown in the example "Large scale finite element model" presented in Section 4.4.2.

4.4 Examples and applications

4.4.1 Illustrative example

To demonstrate the capabilities of the proposed method, a synthetic example is presented. The ALS method is compared to a solution obtained via global optimisation. Both approaches are applied to calculate the interval failure probability $\overline{p}_F$. With ALS the argument optima are detected using the information of the important direction as explained in Section 4.3.1.2. The sign of the important direction in the original space identifies the conjugate states where the extrema of the failure probability are located.

With the global optimisation approach, the search is conducted as an iterative procedure. The examples are solved using both Genetic Algorithm (GA) [31] and BOBYQA (Bounded Optimization BY Quadratic Approximation) [56], as global and local searchers, respectively. With this approach, a thorough search in the sets $\boldsymbol{\Theta}_h$ and $\boldsymbol{\Theta}_x$ is performed. The objective function is defined as the failure probability; thus, at

Table 4.1: Results from case (a), argument optima and associated failure probabilities obtained by means of ALS and Global Optimisation.

$g = 7 + \xi - 2x$;			
	ALS	Global Opt. (GA)	(BOBYQA)
$(\mu_{\min},\ \mu_{\max})$	$(2,\ 0)$	$(2,\ 0.04)$	$(2,\ 0.12)$
$(\sigma_{\min},\ \sigma_{\max})$	$(1.2,\ 2.3)$	$(1.28,\ 2.3)$	$(1.32,\ 2.3)$
$(x_{\min},\ x_{\max})$	$(1,\ 3)$	$(1,\ 3)$	$(1,\ 2.92)$
$\underline{\overline{p_F}}$	$[2.717\ 10^{-9},\ 0.332]$	$[2.702\ 10^{-8},\ 0.322]$	$[4.371\ 10^{-7},\ 0.134]$

any iteration of GA/BOBYQA, a reliability analysis with ALS is performed. This approach can be performed in reasonable time, because adaptive algorithm requires just a few evaluations of the performance function to complete an iteration. Replacing ALS with direct Monte Carlo would lead to thousands of evaluations of the performance function for each iteration, making the approach via global optimisation intractable.

Two cases are considered in this study, i.e. case (a) and case (b).

Case (a): The considered performance function $g(\xi, x) = 7 + \xi - 2x$, includes the parametric p-box, $\xi \in \mathcal{C}$, where

$$\mathcal{C} = \{f_\Xi(\xi; \mu, \sigma) \mid \mu \in [0.9, 1.3],\ \sigma \in [0.7, 2.1]\},$$

and the interval variable $\overline{\underline{x}} = [1,\ 3]$. In this illustrative case the gradient $\nabla g = (1, -2)$, provides an initial guess for the important direction as $\boldsymbol{a} = (1, -2)/\sqrt{5}$. ALS leads to the bounds of the failure probability and the associated argument optima $(x_{\min}, x_{\max}) = (\underline{x}, \overline{x})$, and $\boldsymbol{p}_{\min} = (\overline{\mu}, \underline{\sigma})$, $\boldsymbol{p}_{\max} = (\underline{\mu}, \overline{\sigma})$, as shown in Table 4.1. With the global optimisation approach, using GA with a population size of 50 individuals, an approximation of the of lower and upper bound was obtained after 52 iterations, while BOBYQA provided a slightly less accurate estimate. In this case ALS coincides with the closed-form solution and it is preferable above the global optimisation approach.

Case (b): The multidimensional performance function $g(\boldsymbol{\xi}, \boldsymbol{x}) = 9 + \boldsymbol{\xi}^T \boldsymbol{b}_1 - \boldsymbol{x}^T \boldsymbol{b}_2$ is considered, where $\boldsymbol{b}_1 \in \mathbb{R}^{14}$, and $\boldsymbol{b}_2 \in \mathbb{R}^3$. The parametric p-boxes $\boldsymbol{\xi} \in \mathbb{R}^{14}$ are defined by the Credal set

$$\mathcal{C} = \left\{f_\Xi(\boldsymbol{\xi}; \boldsymbol{\mu}, \boldsymbol{\sigma}) \mid \boldsymbol{\mu} \in \overline{\underline{\boldsymbol{\mu}}}, \boldsymbol{\sigma} \in \overline{\underline{\boldsymbol{\sigma}}}\right\},$$

where $\overline{\underline{\boldsymbol{\mu}}} = [0.1,\ 1]^{14}$, and $\overline{\underline{\boldsymbol{\sigma}}} = [1.2,\ 2.3]^3$, while the interval variables $\boldsymbol{x} \in \mathbb{R}^{14}$ are defined by the bounded set $\overline{\underline{\boldsymbol{x}}} = [1,\ 3]^3$. Because of the monotonicity, the ALS approach provides numerically exact results for the failure probability (equal to the closed-form solution). As expected, the global optimisation approach provides only a rough approximation of the solution, as shown in Table 4.2, as it becomes inefficient when the dimensionality of the search domain is too large.

Table 4.2: Results from case (b), interval failure probability obtained by means of ALS and Global Optimisation.

$g = 9 + \boldsymbol{\xi}^T \boldsymbol{b}_1 - \boldsymbol{x}^T \boldsymbol{b}_2$; $\boldsymbol{b}_1 = (1, 4, 2, 0.1, 0.2, 0.6, 5, 0.01, 0.2, 0.3, 0.25, 0.14, 0.8, 3)$, $\boldsymbol{b}_2 = (-2, 0.1, 1)$			
	ALS	Global Opt. (GA)	(BOBYQA)
$\overline{\underline{p_F}}$	$[1.795\ 10^{-9},\ 0.1452]$	$[7.302\ 10^{-6},\ 0.0053]$	$[2.538\ 10^{-5},\ 0.0046]$

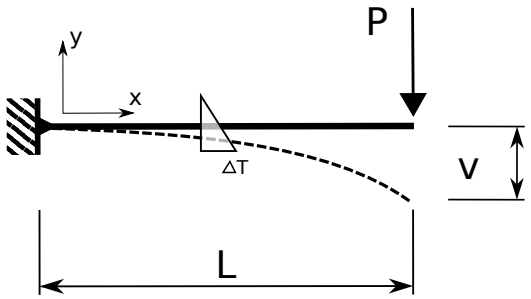

Figure 4.2: Cantilever beam subject to point load and thermal gradient

Note on the application of the approach The presented numerical example is meant to illustrate the performance of the methods without being bounded to any specific application. However, the functions presented in case (a) and (b) can be easily linked to an engineering problem. For example, in the context of structural engineering, the well-known problem of calculating the tip displacement of a cantilever beam (see Figure 4.2) with a tip point load and a thermal gradient resembles very much the function of case (a). The tip displacement v is obtained as a function of the point load P and the curvature of the beam $\chi(\Delta T)$, function of the temperature difference ΔT. v can be obtained as the sum of the displacement due to the point load v_P and the displacement due to the thermal gradient v_T, as $v = v_P - v_T$, as

$$v = v_P - v_T = \frac{PL^3}{48EI} - \frac{\alpha \Delta T}{h/2} L^2/2. \tag{4.11}$$

In Eq. (4.11) the curvature of the beam, $\chi(T) = \frac{\alpha \Delta T}{h/2}$ is proportional to the temperature difference T and the coefficient of thermal expansion α. By fixing a threshold on the tip displacement $\tilde{v}$, the following performance function can be defined

$$g(P, T) = \tilde{v} - v = \tilde{v} - \frac{PL^3}{48EI} + \frac{\alpha \Delta T}{h/2} L^2/2 = \tilde{v} - aP + bT; \tag{4.12}$$

where, the point load and the temperature are the state variables of the problem and can be modelled using p-boxes, as it has been done in the illustrative example.

4.4.2 Large scale finite element model of a six-storey building

In this example the reliability analysis of a six-storey building subject to wind loading is investigated. Three different models of uncertainty are considered with increasing level of generality. First, a standard reliability analysis, where the inputs are modelled by CDFs, is performed. Second, the structural parameters are provided as parametric p-boxes using a Credal set. In the third analysis, both parametric p-boxes and intervals are considered for the structural parameters of the building.

An ABAQUS finite element model (FEM) is built for the six-storey building, as illustrated in Figure (4.3), which includes beam, shell and solid elements. The load is considered as combination of a (simplified) lateral wind loading with the self-weight, which are both modelled by deterministic static forces acting at the nodes of each floor. The magnitude of the wind load increases with the height of the building. The FEM of the structure involves approximately 8200 elements and $66,300$ DOFs. A total of 244 independent variables are considered to account for the uncertainty of the structural parameters. The material strength (capacity) is represented by a normal distribution, while log-normal distributions are assigned to the Young's modulus, the density and the Poisson ratio. In addition, the cross-sectional width and height of the columns are modelled by independent uniform distributions. A summary of the distribution models is reported in Table 4.3.

The building is subject to lateral wind loading, which makes the top floor the critical part of the structure, where the columns experience a larger stress than in other parts of the building. Component failure for a representative column of the 6th floor is considered critical and addressed in terms of Tresca stress. Failure occurs when a critical level of Tresca stress in the selected representative column is triggered. Note that the Tresca stress is a common concept in solids of structures and refers to a combination of stresses in solids that if exceeds a given threshold may lead to a change in the material properties. Refer to Ref. [2] for more information about the Tresca stress. The performance function is defined as

$$f(\boldsymbol{x}) = |\sigma_I(\boldsymbol{x}) - \sigma_{III}(\boldsymbol{x})|/2 - \sigma_y, \tag{4.13}$$

i.e. as the difference between the maximum Tresca stress $|\sigma_I(\boldsymbol{x}) - \sigma_{III}(\boldsymbol{x})|/2$ and the yield stress, σ_y, where $\sigma_{III} \leqslant \sigma_I$ are the principal stresses, which in turns are functions of the state variables $\boldsymbol{x}$, such as material properties, members size, etc. (see Table 4.3).

Standard reliability analysis A reliability analysis is performed with the distribution models of Table 4.3, and using LS and ALS for comparison of efficiency. Note from Table 4.3 that this analysis does not consider imprecision. The initial important direction is selected based on the gradient at the origin of the SNS. The identified important direction is displayed in figure 4.4, where the first coordinate (the material's

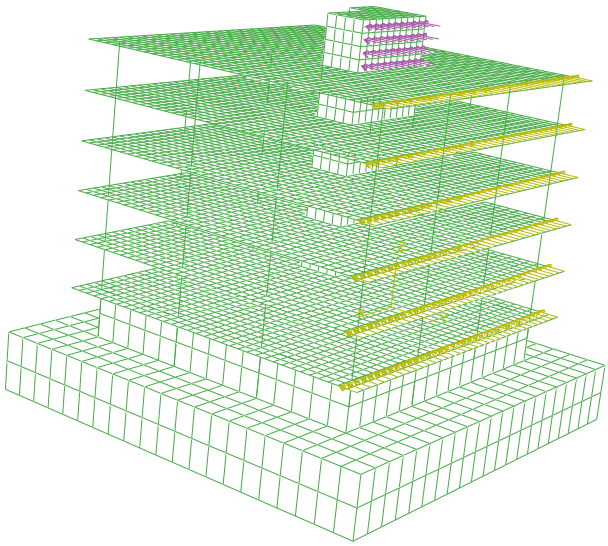

Figure 4.3: FE-model of the six-storey building.

Table 4.3: Precise distribution models for the input structural parameters.

Input #	Probability dist.	Distribution	Description	Units
1	N(0.1, 0.001)	Normal	Column's strength	GPa
$2-193$	Unif$(0.36, 0.44)$	Uniform	Sections size	m
$194-212$	LN(35.0, 12.25)	Log-normal	Young's modulus	GPa
$213-231$	LN(2.5, 0.0625)	Log-normal	Material's density	kg/dm^3
$232-244$	LN(0.25, 0.000625)	Log-normal	Poisson's ratio	-

strength) appears to be the most important one. The other coordinates refer to the size of the cross-sections, the Young's modulus, the density, and the Poisson's ratio, respectively (see Table 4.3). As illustrated in Figure (4.4), only a few state variables (S.V.) dominate the important direction; these are the Young's modulus of columns of floor 6 (S.V. #199) and the density of the columns of floors 5 and 6 (S.V. #223 and #224), along with the yield strength (S.V. #1). In this example, performing LS with 30 lines (180 samples) leads to the failure probability of $\hat{p}_F = 1.30 \cdot 10^{-4}$ and a coefficient of variation of $CoV = 0.076$. ALS leads to the probability of failure $\hat{p}_F = 1.42 \cdot 10^{-4}$ with a coefficient of variation of $CoV = 0.092$, but with only 62 samples. Both methods estimate approximately the same value of failure probability, but quite a smaller number of model evaluations were required by ALS. The efficiency of ALS can be appreciated from Figure 4.5, where it is shown that only few model evaluations per line are required to calculate the partial probabilities $w(\boldsymbol{u}^{\{j\}})$. In Figure 4.5, lines are represented in a reduced space obtained in SNS considering (a) the norm of the standard points, and (b) the distance of the points from the sampling hyper-plane. On the lines the small

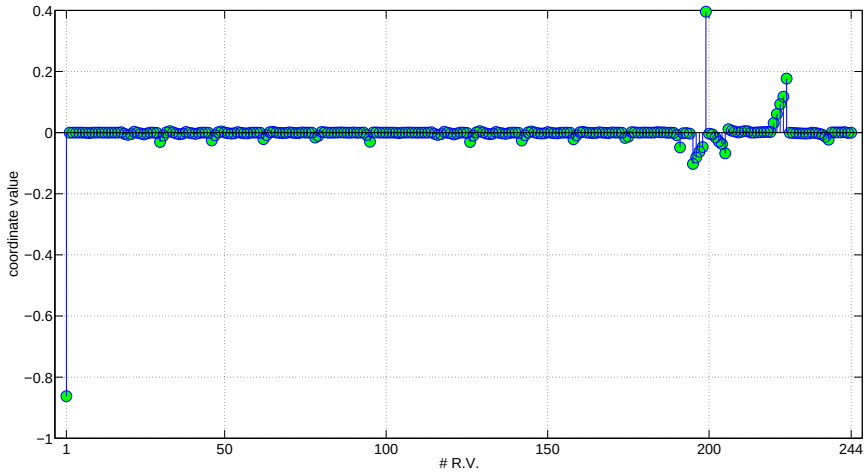

Figure 4.4: Values of the 244 coordinates of the initial important direction in SNS.

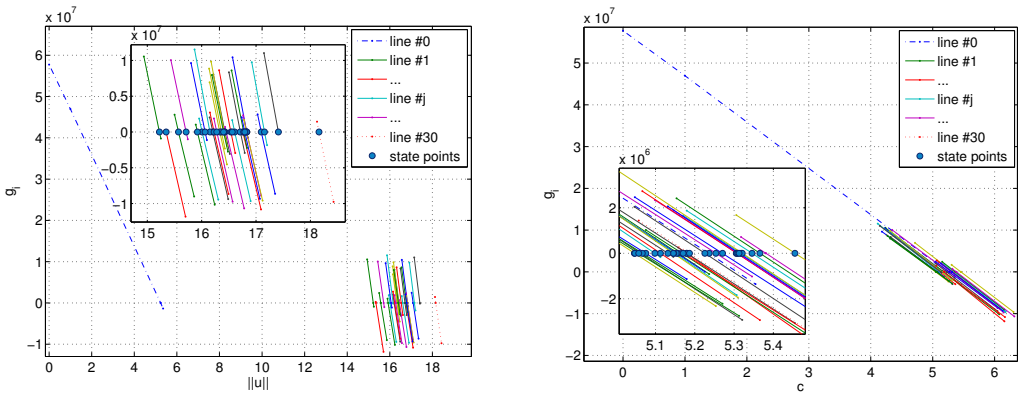

(a) **(b)**

Figure 4.5: Values of the performance function along lines in SNS. Figure (a) shows values of the performance g against the L-2 norm of the standard normal points $||\tilde{\boldsymbol{u}}||$, and Figure (b) shows values of the performance g aginst the distance from the hyperplane c.

round dots represent the number of model evaluations, whereas the big dot represents the state point $\tilde{\boldsymbol{u}}$. Moreover, the adaptive nature of the algorithm can be appreciated from Figure 4.5, where it is shown how lines stop as soon as the limit state surface is met.

Robust reliability analysis with parametric p-boxes The model of uncertainty is extended to include the Credal set

$$\mathcal{C} = \left\{ f_X\left(\boldsymbol{x}; \boldsymbol{p}\right) \mid \boldsymbol{p} \in \mathbb{R}^{488},\ \boldsymbol{p} \in \boldsymbol{\Theta}_h \right\},$$

where $f_X\left(\boldsymbol{x}; \boldsymbol{p}\right)$ is the probability density function of independent variables, $\boldsymbol{x}$, which hyper-parameters are $\boldsymbol{p} = (\mu_1,\ \sigma_1, ..., m_{244}, v_{244})$, and where $\Theta_h = \times_i^{488}\ \underline{\overline{p}}_i$ (see Table

4.3). The interval parameters are represented as $\underline{p}_\epsilon = p_c\,(1-\epsilon)$, $\overline{p}_\epsilon = p_c\,(1+\epsilon)$, using the interval center $p_c = (\overline{p} + \underline{p})/2$ and the relative radius of imprecision ϵ. These intervals $[\underline{\boldsymbol{p}}_\epsilon,\ \overline{\boldsymbol{p}}_\epsilon]$ are summarized in the bounded domain Θ_h. In the example, all interval parameters, are modelled with the same relative imprecision ϵ. In order to explore the effects of ϵ on the results, we use a fuzzy set to consider a nested set of intervals $\tilde{\boldsymbol{p}}_\epsilon = \left\{[\underline{\boldsymbol{p}}_\epsilon,\ \overline{\boldsymbol{p}}_\epsilon]\right\}$ for the parameters in one analysis. The amplitude (width) of the intervals is controlled by ϵ to obtain fuzzy sets $\tilde{\boldsymbol{p}}_\epsilon$ as shown in Figure 4.6. An upper limit for the relative uncertainty is set as $\bar{\epsilon} = 0.075$. Specifically, the intervals for $\epsilon = \{0, 0.005, 0.01, 0.025, 0.05, 0.075\}$ are considered. The reliability analysis with the generalized model of uncertainty is performed using the important direction determined in the original space.

Performing a random search in the set Θ_h, for example by means of a Latin Hypercube algorithm, it was found that the important direction did not significantly change in the original space. This permitted the identification of the argument optima in the bounded set Θ_h as combination of extreme moments as described in Section 4.3.1.2. These upper and lower conjugate states are also associated with the maximum and minimum of the failure probability, respectively. Results of the robust reliability analysis are shown in Figure 4.6b and in Table 4.4. From Table 4.4 it can be appreciated that the number of samples required by one robust reliability analysis, on average, is approximately 254, which is just the number of samples required by a standard reliability analysis using Line Sampling. Results from Table 4.4 show how a tolerable level of imprecision can be investigated. For example, a 5% level of imprecision, which means that all the inputs of Table 4.1 are intervals $\overline{\underline{\boldsymbol{p}}}_{0.05}$ obtained as $\overline{\underline{\boldsymbol{p}}}_{0.05} = \boldsymbol{p}_c\,[1-0.05,\ 1+0.05]$, leads to the upper bound $\overline{p}_F = 3.8\ 10^{-2}$, which is two orders of magnitude bigger than standard analysis. Also, the width of the interval $\overline{\underline{p}}_F$ demonstrates that a 5% level of imprecision propagates in a quite wide failure probability interval $\overline{\underline{p}}_F = [2.27\ 10^{-8},\ 3.88\ 10^{-2}]$, which in some cases may render the reliability analysis uninformative, forcing the analyst to collect more data. This shows how sensitive the reliability analysis is with respect to the imprecision of the inputs, especially if many variables are involved. The failure probability is obtained as a fuzzy set, which includes the standard reliability analysis as special case with $\epsilon = 0$. Each interval $\overline{\underline{p}}_F$ corresponds to the respective interval of input parameters $\overline{\underline{\boldsymbol{p}}}_\epsilon = [\underline{\boldsymbol{p}}_\epsilon,\ \overline{\boldsymbol{p}}_\epsilon]$ for the same membership level, and each membership level is associated with a different value ϵ, see Figure 4.6. In a design context, this result can be used to identify a tolerated level of imprecision for the inputs given a constraint on the failure probability. For example, fixing an allowable failure probability of 10^{-3}, the maximum level of imprecision for the distribution parameters is limited to 1%, as can be seen from Figure 4.6.

Robust reliability analysis with intervals and parametric p-boxes In this example the section sizes $\boldsymbol{x} \in \mathbb{R}^{192}$ are considered as interval variables, while the remaining

Table 4.4: Results of the robust reliability analysis of the multi-storey building using distributional p-boxes, obtained as of lower and upper bounds of the failure probability.

	Lower Bound		Upper Bound		
ϵ	$\underline{p}_F$	CoV	$\overline{p}_F$	CoV	Ns
0.000	$1.42\ 10^{-4}$	$9.2\ 10^{-2}$	$1.42\ 10^{-4}$	$9.2\ 10^{-2}$	126
0.005	$5.75\ 10^{-5}$	$8.7\ 10^{-2}$	$2.63\ 10^{-4}$	$7.1\ 10^{-2}$	257
0.010	$4.57\ 10^{-5}$	$33.6\ 10^{-2}$	$5.30\ 10^{-4}$	$11.5\ 10^{-2}$	250
0.025	$1.75\ 10^{-6}$	$8.8\ 10^{-2}$	$3.22\ 10^{-3}$	$5.3\ 10^{-2}$	253
0.050	$2.27\ 10^{-8}$	$57.0\ 10^{-2}$	$3.88\ 10^{-2}$	$5.4\ 10^{-2}$	255
0.075	$1.88\ 10^{-11}$	$12.2\ 10^{-2}$	$2.02\ 10^{-1}$	$3.5\ 10^{-2}$	254

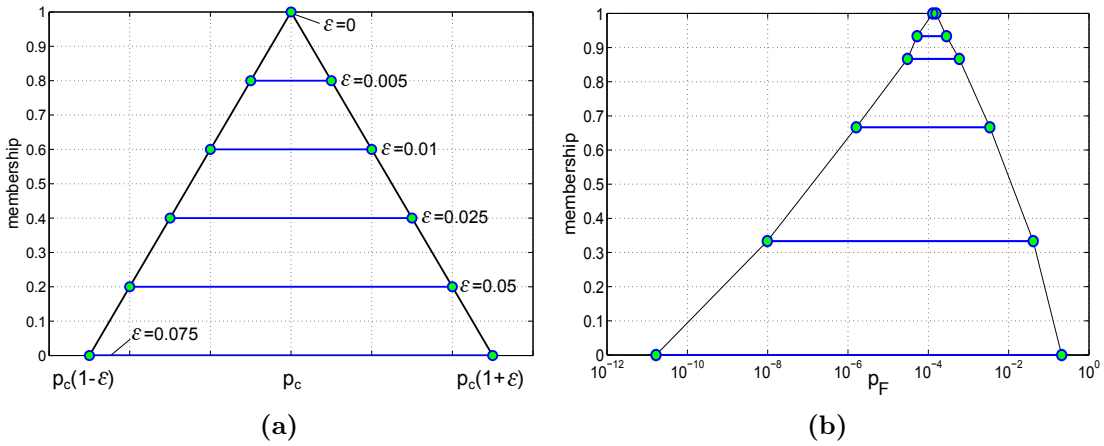

Figure 4.6: (a) Fuzzy parameters $\tilde{p} = \{p_c\ [1-\epsilon_j,\ 1+\epsilon_j]\}_{j=1}^{6}$ and (b) fuzzy failure probability obtained as set of results for different levels of imprecision.

Table 4.5: Inputs definition of distributional p-boxes; the relative radius of imprecision for this model is set as $\epsilon = \{0, 0.005, 0.0.01, 0.025, 0.05, 0.075\}$.

Input #	Prob. dist.	$\overline{p} = p_c\ [1-\epsilon,\ 1+\epsilon]$		Description	Units
1	N($\underline{\mu}$, $\overline{\sigma}$)	$\mu_c = 0.1$	$\sigma_c = 0.01$	Columns' strength	GPa
$2-193$	Unif($\underline{a}, \overline{b}$)	$a_c = 0.36$	$b_c = 0.44$	Sections' size	m
$194-212$	LN($\overline{m}$, $\underline{v}$)	$m_c = 35$	$v_c = 12.25$	Young's modulus	GPa
$213-231$	LN($\overline{m}$, $\underline{v}$)	$m_c = 2.5$	$v_c = 0.0625$	Material's density	kg/dm^3
$232-244$	LN($\overline{m}$, $\underline{v}$)	$m_c = 0.25$	$v_c = 0.000625$	Poisson's ratio	-

structural parameters $\boldsymbol{\zeta} \in \mathbb{R}^{52}$ are considered as distributional p-boxes. The model of uncertainty comprises the Credal set

$$\mathcal{C}\left\{h_Z\left(\boldsymbol{\zeta};\boldsymbol{p}\right)\ \mid \boldsymbol{p} \in \mathbb{R}^{104},\ \boldsymbol{p} \in \Theta_h\right\},$$

and the bounded set $\Theta_x = \times_i^{192} \overline{\underline{x}}_i$. The imprecision is modelled using the radius of imprecision ϵ, as in the previous case, see Table 4.6. An upper limit for the relative radius of imprecision is set to $\overline{\epsilon} = 0.03$. In the analysis, a rough search in the domains Θ_h and Θ_x permitted to identify a main important direction for determining the argument optima associated with the minimum and maximum value of failure probability. The result is shown in Table 4.7 and Figure 4.7b. From Table 4.7, it can be appreciated that the number of samples required by one robust reliability analysis, on average, is approximately 254. It is to point out that a direct Monte Carlo approach would have required several thousands of samples to compute the failure probability bounds, as a full reliability analysis is needed for every distribution function comprised within the input p-boxes.

To explore the sensitivity against imprecision of the uncertain parameters, the failure probability is obtained as a fuzzy set. The relative radii of imprecision $\epsilon = \{0, 0.01, 0.015, 0.020, 0.025, 0.03\}$ are considered to construct a fuzzy model for all parameters, see Figure 4.7a. The intervals for the structural parameters $\overline{\underline{x}}$ in Θ_x, describing the size of the cross-sections, are independent of ϵ, see Table 4.6. Once more, the analysis may serve as a design tool to determine the tolerable level of imprecision given a threshold of allowable probability.

Here, the uncertainty due to imprecision is larger, because the whole range of the intervals is taken into account for the cross-sections, as uniform distributions are replaced with intervals. As in the previous case, a rough search in the sets Θ_h and Θ_x has permitted to identify a main important direction for selecting the argument optima producing minimum and maximum value of the failure probability. Values of the failure probability, obtained with $\epsilon = \{0, 0.01, 0.015, 0.020, 0.025, 0.03\}$, are shown in Figure 4.7 (b).

Table 4.6: Inputs definition for intervals and parametric p-boxes; the relative radius of imprecision for this model is set as $\epsilon = \{0, 0.01, 0.015, 0.020, 0.025, 0.03\}$.

Input #	Uncertainties type		$\underline{p} = p_c\ [1-\epsilon,\ 1+\epsilon]$, $\overline{x} = [\underline{x},\ \overline{x}]$	
1	distribution	$\mathrm{N}(\underline{\mu},\ \overline{\sigma}^2)$	$\mu_c = 0.1$	$\sigma_c^2 = 0.001$
$2-193$	interval	$\overline{x}$	$\underline{x} = 0.36$	$\overline{x} = 0.44$
$194-212$	distribution	$\mathrm{LN}(\overline{m},\ \underline{v})$	$m_c = 35$	$v_c = 12.25$
$213-231$	distribution	$\mathrm{LN}(\overline{m},\ \underline{v})$	$m_c = 2.5$	$v_c = 0.0625$
$232-244$	distribution	$\mathrm{LN}(\overline{m},\ \underline{v})$	$m_c = 0.25$	$v_c = 0.000625$

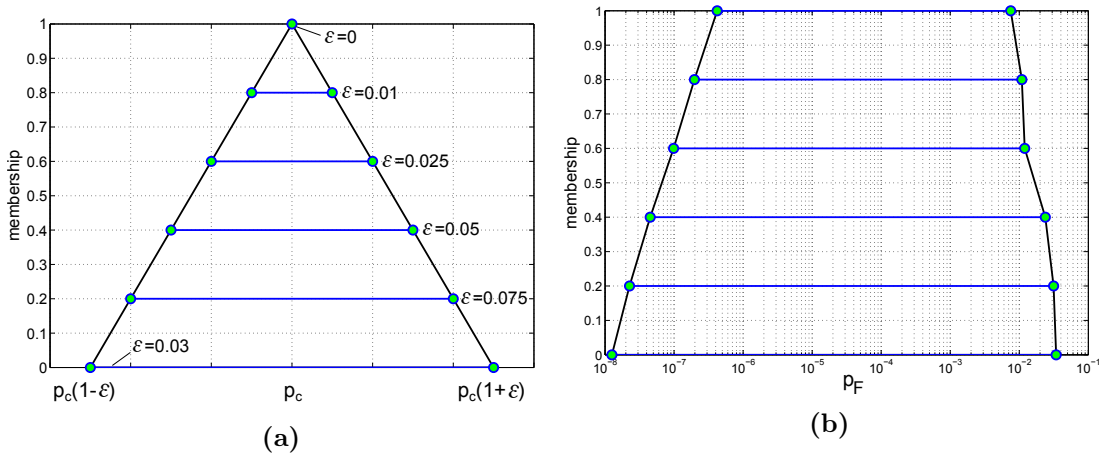

Figure 4.7: (a) Fuzzy distribution parameters (input) $\tilde{p} = \{p_c\ [1-\epsilon_j,\ 1+\epsilon_j]\}_{j=1}^{6}$ and (b) fuzzy failure probability (output) obtained with different levels of imprecision

Table 4.7: Lower and upper failure probability bounds resulting from the reliability analysis

	Lower Bound		Upper Bound		
ϵ	$\underline{p}_F$	CoV	$\overline{p}_F$	CoV	Ns
0.000	$4.70\ 10^{-7}$	$10.2\ 10^{-2}$	$6.73\ 10^{-3}$	$11.5\ 10^{-2}$	259
0.010	$2.28\ 10^{-7}$	$13.4\ 10^{-2}$	$9.71\ 10^{-3}$	$12.2\ 10^{-2}$	247
0.015	$1.10\ 10^{-7}$	$10.3\ 10^{-2}$	$1.11\ 10^{-2}$	$7.6\ 10^{-2}$	255
0.020	$5.19\ 10^{-8}$	$13.1\ 10^{-2}$	$2.08\ 10^{-2}$	$14.6\ 10^{-2}$	255
0.025	$2.51\ 10^{-8}$	$9.97\ 10^{-2}$	$2.72\ 10^{-2}$	$15.3\ 10^{-2}$	249
0.030	$1.40\ 10^{-8}$	$9.94\ 10^{-2}$	$3.21\ 10^{-2}$	$6.5\ 10^{-2}$	254

4.5 Chapter summary

In this chapter, a numerical strategy to estimate imprecise probabilities, based on Line Sampling, by means of a Double Loop approach has been presented.

Robust reliability analyses is capable of capturing both variability and imprecision in the inputs of the engineered system. The imprecision can significantly affect the outcome of a reliability analysis, and, depending on its extent, results can sensibly differ from the ones obtained with standard analysis. A novel numerical strategy for computing set-valued failure probabilities has been presented. An adaptive algorithm has been developed in Chapter 3 to better link the advanced sampling method to the Double Loop approach. The global search for lower and upper bounds of the failure probability is driven using an averaged important direction, obtained in the original state space of the input variables. As the conjugate states are identified lower and upper reliability bounds can be computed performing two standard reliability analyses.

The efficiency of the approach has been shown by means of real-scale application to a finite element model involving 244 variables. The results presented in this chapter have been peer-reviewed and published in Ref. [21] (see journal paper 1 from the List of Publications), and have been presented at the 6th International Conference on Reliable Engineering Computing, in May 2014, and at the Second International Conference on Vulnerability and Risk Analysis and Management, in July 2014.

Chapter 5

Efficient Random Set Propagation by means of Line Sampling

In this chapter, a novel Advanced Sampling strategy based on Line Sampling is presented to propagate the uncertainty using the Random Set approach. The advantage of implementing such a strategy is that the efficiency of Random Set propagation can be increased by orders of magnitude, and it may provide a means for estimating lower failure probability bounds. However, the strategy comes with the limitation that the extreme case realisations may be difficult to identify, once the bounds are computed. Extreme realisations are fully identified if they are associated with a single point in the epistemic domain, so they can be regenerated without calling the system performance function. In order to identify such realisations, a Random Set strategy that combines optimisation with direct Monte Carlo methods is presented, where the extreme realisations are obtained as empirical distributions coming from the solution of the min-max propagation problem.

5.1 Forward Propagation of Random Sets

The forward problem consists in propagating the input uncertainties through the system function, $\mathcal{G}$, that simulates the performance of the system. The ultimate goal of forward propagation is to quantify upper and lower failure probability bounds, as depicted in Figure 5.1. Within the Random Set approach, forward propagation can be performed by means of a number of different methods based on random sampling. For example Subset Simulation, Line Sampling and other importance sampling techniques can be used. These methods may also differentiate in the way the min-max optimisation (or bound propagation) is performed, which in turns depends on the system function.

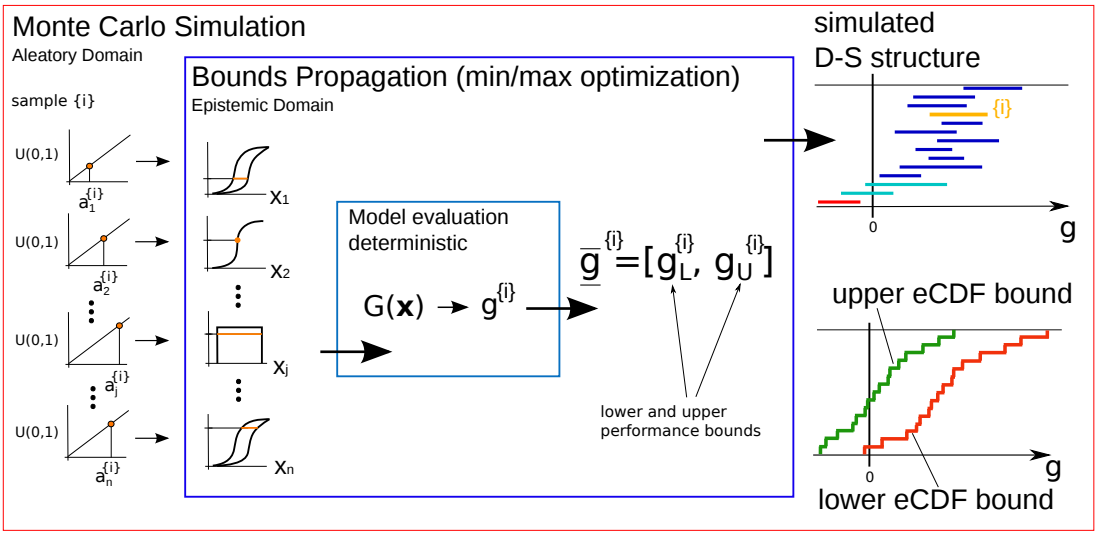

Figure 5.1: Forward propagation with the Random Set approach

5.1.1 Propagation of focal elements

In order to find the image of a focal element, $\gamma \subset \mathcal{X}$, through the system function, $\mathcal{G} : \mathcal{X} \mapsto \mathbb{R}$, the extension principle is applied [28]. The propagation can be done by means of optimisation methods or by means of sampling methods. In essence, this step is a min-max propagation on changing domains. The search domain is the focal set itself, $\gamma^{\{s\}} \subset \mathcal{R}^d$, which is defined by the aleatory component, $\boldsymbol{\alpha}^{\{s\}}$, at the current sample, s. The failure probability bounds are estimated by generating a large number of samples, N_S, drawing as many aleatory components, $\boldsymbol{\alpha}^{\{s\}}$, and corresponding focal elements, $\gamma^{\{s\}}$, and computing the image, $\mathcal{G}(\gamma^{\{s\}})$. Eventually, the associated Dempster-Shafer structures of the system performance are obtained. The procedure to perform focal elements propagation is:

- Draw a sample, $\boldsymbol{\alpha}^{\{s\}}$ from the copula function, C;
- Obtain the focal element $\gamma^{\{s\}} = \Gamma(\boldsymbol{\alpha}^{\{s\}})$;
- Obtain the image of the focal element through the system function as

$$\overline{\underline{\mathcal{G}}}^{\{s\}} = \mathcal{G}(\gamma^{\{s\}}) = \left[\underline{\mathcal{G}}^{\{s\}},\ \overline{\mathcal{G}}^{\{s\}}\right];$$

  this step is non-trivial as it requires a min-max propagation to be performed by means of global optimisation algorithms;
- Repeat the procedure for $s = 1, \ldots, N_S$;
- Estimate lower and upper failure probability as

$$\underline{\hat{p}}_F = \sum_{s=1}^{N_S} \mathcal{I}\left[\gamma^{\{s\}} \subseteq \mathcal{X}_F\right] \qquad \overline{\hat{p}}_F = \sum_{s=1}^{N_S} \mathcal{I}\left[\gamma^{\{s\}} \cap \mathcal{X}_F \neq \varnothing\right]. \tag{5.1}$$

where, the indicator function, $\mathcal{I} : \mathbb{R} \mapsto \{0, 1\}$ equals *one* if the statement is true and *zero* otherwise. The image of the focal element is obtained via min-max propagation as

$$\underline{\mathcal{G}}^{\{s\}} = \inf_{\boldsymbol{x} \in \gamma^{\{s\}}} \mathcal{G}(\boldsymbol{x}), \qquad \overline{\mathcal{G}}^{\{s\}} = \sup_{\boldsymbol{x} \in \gamma^{\{s\}}} \mathcal{G}(\boldsymbol{x}). \tag{5.2}$$

The propagation of focal elements is computationally very demanding, as a large number of samples, N_S, and one min-max propagation, for each sample, is required, which is usually completed invoking global optimisation (such as evolutionary or stochastic algorithms). Thus, efficient approaches are needed to reduce the number of samples and consequently the number of propagations. For example, Subset simulation can be used to efficiently produce samples in the aleatory space, $\boldsymbol{\Omega}$, as shown in [6]. Here, a novel approach based on Line Sampling is proposed to produce samples in the aleatory space, $\boldsymbol{\Omega}$, and to significantly reduce the number of focal elements required to estimate the failure probability bounds.

5.1.2 Efficient Propagation with Line Sampling

By means of Line Sampling, the number of required focal elements can be reduced by orders of magnitude. In order to exploit the feature of the advanced simulation method, points in the aleatory space $\boldsymbol{\alpha}$ have to be mapped to the Standard Normal Space and vice versa. In the latter space, lines can be generated as explained in Chapter 3 to look for points at the border between safe, plausibility and belief domains. The method generates normal random points $\boldsymbol{u}^{\{s\}}$ in the SNS, maps them to the aleatory space and computes the corresponding focal elements. The procedure to produce a focal element and its image through $\mathcal{G}$, starting from a point in the SNS, is

- Draw a sample, $\boldsymbol{u}^{\{s\}} \sim \mathcal{N}(0, 1)$, from the SNS;
- Map the sample back to the aleatory space as

$$\boldsymbol{\alpha}^{\{s\}} = C\left(\Phi(u_1^{\{s\}}), \ldots, \Phi(u_d^{\{s\}})\right); \tag{5.3}$$

- Obtain the focal element $\gamma^{\{s\}} = \Gamma(\boldsymbol{\alpha}^{\{s\}})$;
- Obtain the image of the focal element through the system function, $\overline{\underline{\mathcal{G}}}^{\{s\}}$;

The key feature about the aforementioned procedure is that each point in the SNS, $\boldsymbol{u}$, is associated with a unique focal element γ (see Figure 5.2). Therefore, in the SNS, as well as in the aleatory domain $\boldsymbol{\Omega}$, it possible to identify three different regions: a *survival* region where, $\gamma \cap \mathcal{X}_F = \varnothing$, a *plausibility* region where, $\gamma \cap \mathcal{X}_F \neq \varnothing$ and a *belief* region where, $\gamma \subseteq \mathcal{X}_F$. These regions are fully characterised by the performance function bounds, $\overline{\underline{\mathcal{G}}}$ as shown in Table 5.1. Two net boundaries can be identified both

Table 5.1: Survival, Plausibililty and Belief regions

Survival	$\gamma \cap \mathcal{X}_F = \varnothing$	$\underline{\mathcal{G}} > 0$
Plausibility	$\gamma \cap \mathcal{X}_F \neq \varnothing$	$\underline{\mathcal{G}} \leqslant 0$
Belief	$\gamma \subseteq \mathcal{X}_F$	$\overline{\mathcal{G}} \leqslant 0$

in the SNS and in the aleatory space, $\mathbf{\Omega}$, that separate these three regions (see e.g. Figure 5.2). In the SNS, these two boundaries provide information about the failure probability, as has been shown in Chapters 3 and 4. The procedure to compute lower and upper failure probability bounds using Line Sampling is:

- Set up an important direction, $\boldsymbol{a} \in \mathbb{R}^d$, in the SNS;
- Generate a number of lines, N_L, normally spaced that are orthogonal to the hyperplane identified by $\boldsymbol{a}$. Points on the generated line, l, can be parametrised via the scalar, $c \in \mathbb{R}$ making use of the coordinates $\boldsymbol{u}^*$ of the hyperplane orthogonal to the important direction, as

$$\boldsymbol{u}^{\{l\}}(c) = c \cdot \boldsymbol{a} + \boldsymbol{u}^{*\{l\}} - \left(\boldsymbol{u}^{*\{l\}} - \boldsymbol{a}\right) \cdot \boldsymbol{a}; \tag{5.4}$$

  where, $\boldsymbol{u}^{*\{l\}}$ are the coordinates of the point where the line l meets the orthogonal hyperplane.
- On each line, look for points at the border between survival, plausibility and belief regions. This step requires the point to be mapped back to the aleatory space, and subsequently requires the focal elements to be propagated through the system function, $\mathcal{G}$;
- Denote by $\boldsymbol{u}_P^{\{l\}}$ the point on line l at the border between survival and plausibility regions, and by $\boldsymbol{u}_B^{\{l\}}$ the point on line l at the border between plausibility and belief regions;
- Let c_P and c_B be the scalars, such that $\boldsymbol{u}^{\{l\}}(c_P) = \boldsymbol{u}_P^{\{l\}}$ and $\boldsymbol{u}^{\{l\}}(c_B) = \boldsymbol{u}_B^{\{l\}}$;
- Compute the probability lower and upper bounds on line l as

$$\underline{p}_F^{\{l\}} = \Phi\left(-|c_P|\right); \qquad \overline{p}_F^{\{l\}} = \Phi\left(-|c_B|\right); \tag{5.5}$$

- Estimate lower and upper probability bounds, making the average over the number of lines as

$$\underline{p}_F = \frac{1}{N_L} \sum_{j=1}^{N_L} \underline{p}_F^{\{l\}}, \qquad \overline{p}_F = \frac{1}{N_L} \sum_{j=1}^{N_L} \overline{p}_F^{\{l\}}. \tag{5.6}$$

The proposed strategy can be used for the estimation of very small probabilities without compromising the accuracy. It is therefore particularly suited either in problems with

Table 5.2: Mean values and standard deviations for the definition of the p-box bounds

P-box	$\overline{\mu}$	$\overline{\sigma}$	Distribution
x	$[2.0,\ 2.5]$	$[0.5,\ 0.6]$	Normal
y	$[-1.5,\ -1]$	$[0.5,\ 0.6]$	Normal

high levels of imprecision where the lower probability bound is quite small, or in problems involving safety-critical systems with strict failure probability requirements. With this strategy the amount of computations required is independent of the magnitude of the probability target. For example, with a probability target of 10^{-6}, more than ten million focal sets would be required using a plain Monte Carlo approach, which is clearly prohibitive. The efficiency of the strategy can be further enhanced by means of good programming, i.e. by selecting the lines to a specific order, and by efficiently searching for the bordering points.

5.2 Forward propagation example

In this section, a simple numerical example is presented to show limitations and advantages of the proposed strategy. The system performance function, $\mathcal{G} : \mathcal{X} \mapsto g$, has the expression

$$g = x^2\ y + e^x; \tag{5.7}$$

where, x and y are p-boxes obtained from a Normal distribution with interval hyperparameters, as shown in Table 5.2. The example function has been selected to simulate a common situation in systems analysis, where several disconnected failure regions may appear. The failure region is defined as $\mathcal{X}_F = \{x, y : \mathcal{G}(x, y) \leqslant 0\}$, and the failure probability is expressed as the interval $\underline{p}_F = P_\Gamma[g \leqslant 0]$.

5.2.1 Random Set approach

In this case, given that the performance is monotonic and increasing with respect to y, an initial important direction can be set as $\boldsymbol{a} = \{0,\ -1\}$. Realisations in the aleatory space, $\boldsymbol{\Omega}$, and in the SNS are shown in Figure 5.2a and in Figure 5.2b. A bundle of lines parallel to the set direction, $\boldsymbol{a}$, are, subsequently, generated in the SNS, as shown in Figure 5.3. On each line, the points $\boldsymbol{u}_P^{\{l\}}$ and $\boldsymbol{u}_B^{\{l\}}$ are identified using a Newton-Raphson algorithm for root finding. The scalars $c_P^{\{l\}}$ and $c_B^{\{l\}}$ are obtained on line l respectively as

$$c_P^{\{l\}} = \left\{c \in \mathbb{R} : \underline{\mathcal{G}}^{\{l\}} \leqslant 0\right\}, \qquad c_B^{\{l\}} = \left\{c \in \mathbb{R} : \overline{\mathcal{G}}^{\{l\}} \leqslant 0\right\}. \tag{5.8}$$

Each candidate solution selected by the root finder corresponds to one focal element propagation of Eq. (5.2). The fact that the performance function is monotonic, sensi-

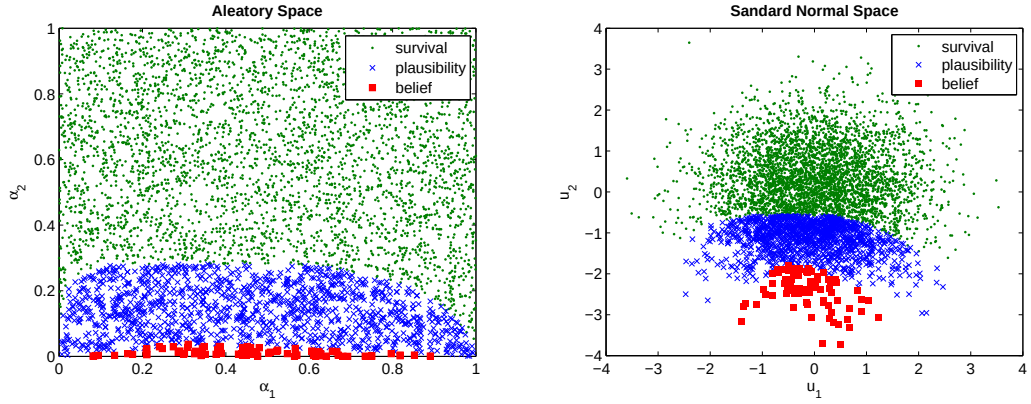

(a) 5000 focal elements in $\mathbf{\Omega}$ **(b)** 5000 focal elements in SNS

Figure 5.2: Realisations in the Aleatory and Standard Normal Space in the survival, plausibility and belief regions

RS approach	N_S	$\hat{\underline{p}}_F$	$\hat{\overline{p}}_F$	$CoV(\%)$
Monte Carlo	30985	0.016	0.250	4.4
Line Sampling	436	0.012	0.257	9.3

Table 5.3: Results obtained with direct Monte Carlo and Line Sampling for the Random Set forward propagation

bly eases the focal element propagation, as the search for minimum and maximum is restricted to the x-dimension only. Results from a direct Monte Carlo are compared to results obtained with the proposed strategy, as shown in Table **??**. The chance to hit the belief region is much smaller than the plausibility region, and may require several thousands of runs in a direct Monte Carlo approach. In this particular example, more than 10^4 samples are needed, as shown in Table **??**, to obtain an estimate of the lower probability bound. On the other hand, with the proposed approach, only a few samples are needed to estimate both probability bounds. Note that in Table **??**, the number of samples, N_S, coincides with the number of focal elements, and results are obtained setting the minimum hits in the belief region to 500. Line Sampling requires significantly fewer focal elements than Monte Carlo to achieve the same accuracy, as shown in Table **??**.

The successful implementation of Line Sampling, in problems involving Random Sets, follows from the flexibility of the adaptive algorithm described in Chapter 3. This would have not been possible in a standard implementation of Line Sampling. Accurate probability computations are achieved using Line Sampling with optimal direction, which can be achieved by means of the adaptive algorithm introduced in previous chapters. Moreover, on the same problem two optimal directions may be needed as there may be two optimal directions, one for the plausibility and one for the belief border. Figure 5.3 shows a standard implementation of Line Sampling where only one direction is used for the simulation. With the proposed strategy only a rough initial direction is

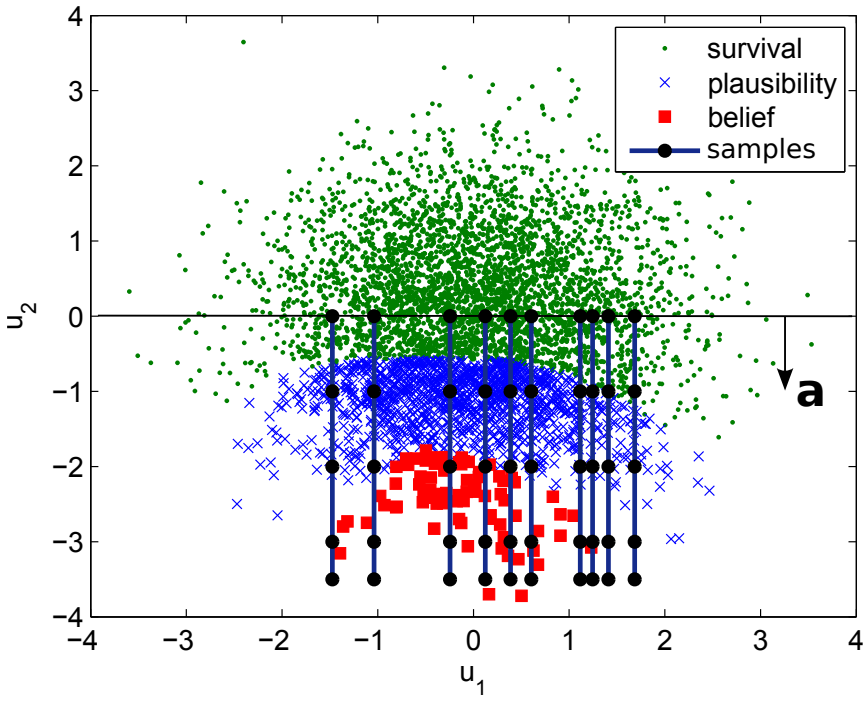

Figure 5.3: Standard implementation of Line sampling operating in a transformed aleatory Standard Normal Space, superimposed to 5000 focal sets obtained with Monte Carlo

needed to start the analysis, which is subsequently adapted as more points are collected near to the domains borders.

5.2.2 Double Loop approach

The Double Loop approach is performed searching for the probability bounds by picking one value in the intervals of Table 5.2 and considering the corresponding normal distributions. All the normal distributions of Table 5.2 should be searched for, however, in this case the system function is monotonic with respect to y, thus the search is restricted to the intervals $\underline{\mu}_x$ and $\overline{\sigma}_x$ only.

Line Sampling has been used to estimate the probability of failure for each candidate solution. Failure probability estimations are shown in Figure 5.4. The upper bound of the failure probability corresponds to the maximum value of σ_x and σ_y, to the minimum value of μ_y and to a value of $\mu_x = 2.05$, as shown in Figure 5.4a. The lower bound corresponds to the maximum value of μ_y and to the maximum value of σ_x, σ_y and to the maximum value $\mu_x = 2.5$, as shown in Figure 5.4b. The double loop approach enables the identification of the combinations of epistemic parameters that produce the extreme responses of the system. A summary of the obtained results is shown in Table **??**, where it can be appreciated that the obtained probability intervals are

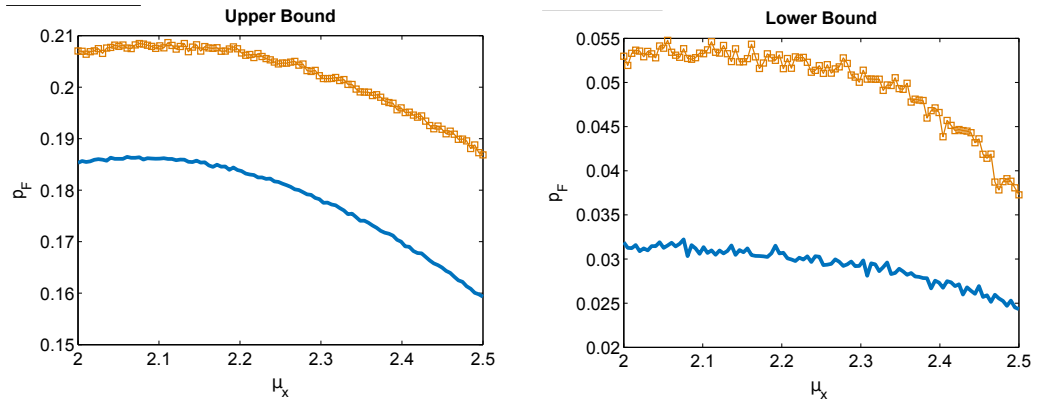

(a) Upper Bound: $\mu_y = \underline{\mu}_y = -1.5$ **(b)** Lower Bound: $\mu_y = \overline{\mu}_y = -1$

Figure 5.4: Failure probability values with Line Sampling fixing the mean value μ_y to $\mu_y = -1.5$ (a) and to $\mu_y = -1$ (b)

Double Loop approach	N_S	$\hat{p}_F^{\min}$	$\hat{p}_F^{\max}$	$CoV(\%)$
Monte Carlo	10^6	0.0245	0.187	14.2
Line Sampling	23943	0.0237	0.184	10.3

Table 5.4: Results with a Double Loop approach

narrower than in the Random Set approach, as the Double Loop approach only looks for distributions belonging to the parental probability model.

5.3 Backward propagation of Random Sets

The back propagation problem consists in identifying the distribution functions that lead to the failure probability bounds. The Random Set approach does not make any assumption on the distribution function within the input distribution bounds, therefore, a one-to-one relationship between the probability bounds and the corresponding distribution functions does not exist. It is even questionable whether there exists a distribution function in the input space capable of reproducing the probability bounds. Samples drawn from these distributions are referred to as *extreme case realisations*.

The procedure to perform back propagation is:

- Collect all the minima, $\underline{\mathcal{G}}^{\{l\}}$, and maxima, $\overline{\mathcal{G}}^{\{l\}}$ from the Dempster-Shafer structure of the system performance; this can be done keeping track of the minima (maxima) and corresponding argument minima (maxima) after the min-max propagation;

- Identify the corresponding argument minima and maxima for each sampled focal elements as

$$\tilde{\boldsymbol{x}}_{\min}^{\{s\}} = \arg\min_{x \in \gamma^{\{s\}}} \mathcal{G}(x), \qquad \tilde{\boldsymbol{x}}_{\max}^{\{s\}} = \arg\max_{x \in \gamma^{\{s\}}} \mathcal{G}(x);$$

- Use the collected data to make simulated empirical distributions of the argument minima, $\tilde{F}_{\min}$, and of the argument maxima, $\tilde{F}_{\max}$;

- Search in the epistemic space, $\boldsymbol{\Theta}$, for two candidates, $\boldsymbol{\theta}_{\min}$ and $\boldsymbol{\theta}_{\max}$, such that the following samples are obtained

$$\boldsymbol{x}_{\min}^{\{s\}} = \mathcal{W}(\boldsymbol{\alpha}^{\{s\}}; \boldsymbol{\theta}_{\min}^{*}) \sim \widetilde{F}_{\min};$$

and

$$\boldsymbol{x}_{\max}^{\{s\}} = \mathcal{W}(\boldsymbol{\alpha}^{\{s\}}; \boldsymbol{\theta}_{\max}^{*}) \sim \widetilde{F}_{\max}.$$

This can be done defining a metric of goodness of fit and seek the epistemic value that corresponds to the distribution function that best fit the distribution of argument minima (maxima) previously collected.

When the epistemic space is obtained as a space products of intervals, the problem of searching for the extreme realisations, $\boldsymbol{x}_{\min}^{\{s\}}$ and $\boldsymbol{x}_{\max}^{\{s\}}$, can be formulated as an optimisation problem, for example using a metric of goodness of fit, as it is explained in the coming section.

5.3.1 Solution to the tracking problem based on K-S test

A viable solution to the back propagation problem can be obtained when Random Sets are defined by means of interval hyper-parameters. This is the case where the bounding CDFs are obtained as the envelope of known distribution functions, and the epistemic space, $\boldsymbol{\Theta}$, is obtained as the space products of all intervals. The solution makes use of the Kolmogorov-Smirnov test to search for an epistemic component, $\theta^* \in \boldsymbol{\Theta}$, that best fits the extreme realisations $\boldsymbol{x}^{*\{s\}}$. The K-S metric defines the "distance" between two distribution functions, by means of

$$D_{KS} = \sup_{\boldsymbol{x}} \; |\tilde{F}(\boldsymbol{x}) - F(\mathcal{W}(\boldsymbol{\alpha}, \boldsymbol{\theta}))|; \tag{5.9}$$

where, $\tilde{F}(\boldsymbol{x})$ is the empirical cumulative distribution obtained from the extreme realisations, and $F(\mathcal{W}(\boldsymbol{\alpha}, \boldsymbol{\theta}))$ is the candidate cumulative distribution function selected among the available ones in the epistemic space. The epistemic component, $\boldsymbol{\theta}_{\min}^{*}$, responsible for the lower probability bound can be identified by solving the optimisation problem

$$\boldsymbol{\theta}_{\min}^{*} = \arg\min_{\boldsymbol{\theta} \in \boldsymbol{\Theta}} \; \sup_{\boldsymbol{x}} \left| \widetilde{F}(\boldsymbol{x}) - F(\mathcal{W}(\boldsymbol{\alpha}; \boldsymbol{\theta})) \right|. \tag{5.10}$$

In the same way, the epistemic component for the probability upper bound, $\boldsymbol{\theta}_{\max}^{*}$ can be identified.

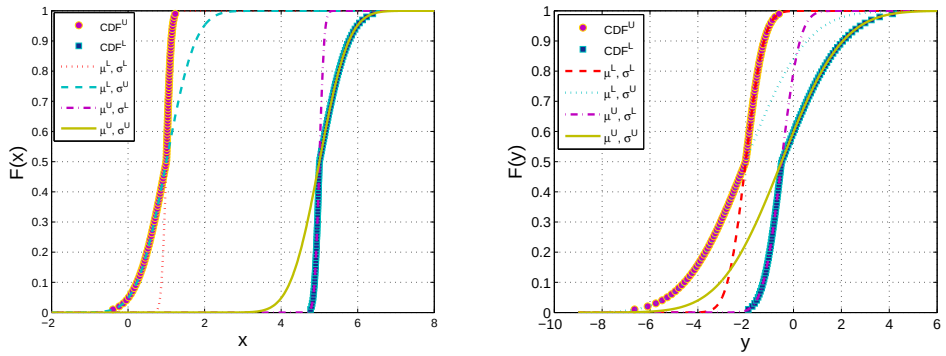

(a) **(b)**

Figure 5.5: Bounding normal CDFs for x (a), bounding normal CDFs for y (b).

P-box	$\overline{\underline{\mu}}$	$\overline{\underline{\sigma}}$	Distribution
x	$[1,\ 5]$	$[0.1,\ 0.6]$	Normal
y	$[-2,\ -0.5]$	$[0.6,\ 2]$	Normal

Table 5.5: Mean values and standard deviations for the definition of the p-box bounds

5.3.2 Numerical example

In this example, the p-boxes x and y of the performance function, $g = x^2\ y + e^x$, are obtained using the intervals shown in Table **??**. The p-boxes defined in Table **??** are represented in Figures 5.5a and 5.5b in terms of bounding CDFs.

The aim of this example is to identify the failure probability bounds and the corresponding realisations in the input space, i.e. those CDFs that yield the minimum and maximum failure probability.

Depending on how the input space of candidate solutions is searched for, the solution may be significantly different. In the next sections two different approaches of searching in the input space of candidate solutions are presented.

5.3.2.1 The Double Loop approach

In this simple case, the optimisation can be reduced to a one-dimensional search. In fact, the function of Eq. (5.7) is monotonically increasing in y, which permits to discharge $\overline{\underline{\mu}}_y$ from the list of candidates, as $\underline{\mu}_y$ and $\overline{\mu}_y$ corresponds to $\overline{p}_F$ and $\underline{p}_F$, respectively. Also, the standard deviations can be taken out of the optimisation as only four candidate solutions can be identified, which correspond to the four corners of the domain $\overline{\underline{\boldsymbol{\sigma}}} = \overline{\underline{\sigma}}_x \times \overline{\underline{\sigma}}_y$. Contour lines of the performance function are shown in Figure 5.6. The optimisation is, therefore, reduced to a search along the (upper and lower) x-edges. Given the shape of the limit state surface, we expect the maximum failure probability to be located somewhere near the peak of the limit sate surface. Minimum and maximum failure probabilities are obtained on the upper and lower edges of the μ_x domain respectively,

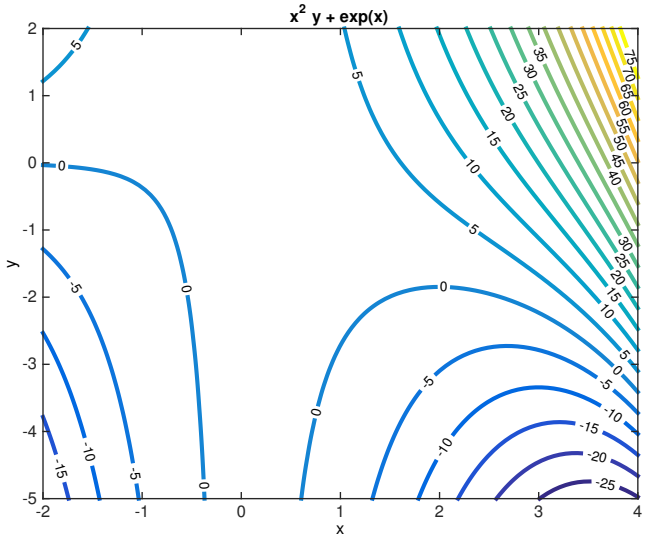

Figure 5.6: Limit state surface and box of mean values

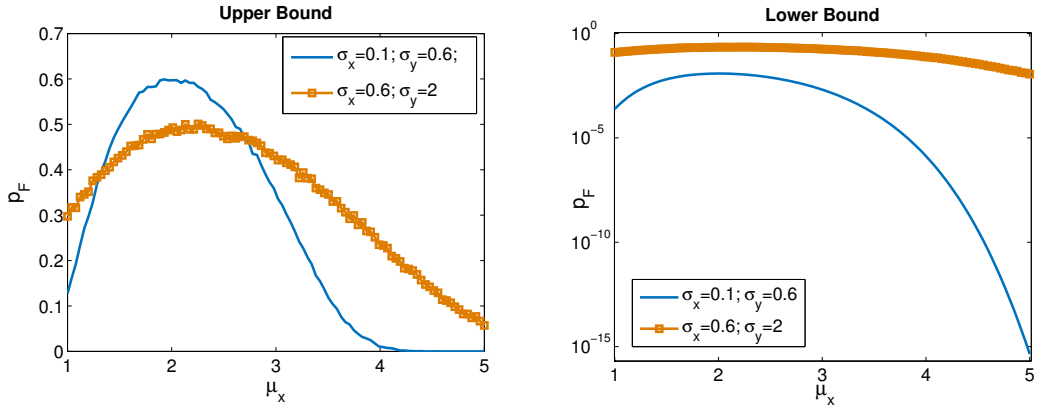

(a) Upper bound with $\mu_y = -2$ **(b)** Upper bound with $\mu_y = -0.5$

Figure 5.7: Failure probability values with Line Sampling fixing the mean value μ_y to $\mu_y = -2$ (a) and to $\mu_y = -0.5$ (b)

populating the space with 1000 realisations. On each realisation, the failure probability is estimated using MC simulation with 10^5 samples. Results from the edge optimisation are shown in Figure 5.7a, where it is shown that the maximum failure probability (unlike the minimum) is attained within the edge, thus not at the corners of the domain. Figure 5.7b shows that the minimum failure probability is held at the right endpoints of the domain, i.e. for $\mu_x = 5$.

The argument optima and corresponding failure probability extrema are reported in Table 5.6.

P-box	min p_F $4.4\ 10^{-16}$	max p_F 0.598
x	$(\mu_x)^{\min} =$ 5.0	$(\mu_x)^{\max} =$ 2.17
x	$(\sigma_x)^{\min} =$ 0.1	$(\sigma_x)^{\max} =$ 0.1
y	$(\mu_y)^{\min} =$ -0.5	$(\mu_y)^{\max} =$ -2.0
y	$(\sigma_y)^{\min} =$ 0.6	$(\sigma_y)^{\max} =$ 2.0

Table 5.6: Failure probability bounds with Line Sampling and corresponding extreme normal distributions

5.3.3 The Random Set approach

The failure probability bounds are obtained by generating a large number of samples or focal elements, and subsequently constructing the associated D-S structure of the response. The procedure for constructing the D-S structure of the response is briefly summarized as,

1. Draw a uniform random number, $\boldsymbol{\alpha}^{\{s\}}$, for each p-box, between 0 and 1;

2. Get the sample endpoints $\overline{\underline{\boldsymbol{x}}}^{\{s\}} = \overline{\underline{x}}^{\{s\}} \times \overline{\underline{y}}^{\{s\}}$ using the inverse bounding CDFs, $\overline{\underline{F}}^{-1}$ as;

$$\underline{\boldsymbol{x}}^{\{s\}} = \overline{F}^{-1}\left(\boldsymbol{\alpha}^{\{s\}}\right);\ \overline{\boldsymbol{x}}^{\{s\}} = \underline{F}^{-1}\left(\boldsymbol{\alpha}^{\{s\}}\right); \tag{5.11}$$

3. Identify minimum, $\underline{g}^{\{s\}}$, and maximum response, $\overline{g}^{\{s\}}$, within the search domain, $\overline{\underline{\boldsymbol{x}}}^{\{s\}}$. This step is also referred to as min-max propagation;

4. Repeat the above steps for $s = 1, \ldots, N_S$;

5. Collect samples and corresponding response extrema, $\tilde{\boldsymbol{x}}_{\min}^{\{s\}}$ and $\tilde{\boldsymbol{x}}_{\max}^{\{s\}}$.

Once the D-S structure of the response is obtained, the failure probability bounds are obtained from the D-S plausibility and belief as

$$\underline{p}_F = \lim_{N_s \to \infty} \frac{1}{N_s} \sum_{s=1}^{N_s} \mathcal{I}[\overline{g}^{\{s\}} < 0]; \tag{5.12}$$

$$\overline{p}_F = \lim_{N_s \to \infty} \frac{1}{N_s} \sum_{s=1}^{N_s} \mathcal{I}[\underline{g}^{\{s\}} < 0]; \tag{5.13}$$

where, $\mathcal{I} : \mathbb{R} \to \{0, 1\}$ is the indicator function. Most of the attention, in the above procedure, is usually given to the min-max propagation step. In fact, this can be troublesome, especially if the response is the output of a black-box model, where the propagation is performed by invoking global optimisation algorithms.

5.3.3.1 The min-max propagation

The performance function of Eq. (5.7) is monotonically increasing with respect to y, which is a great advantage as it excludes the presence of relative minima and maxima. Moreover, it implies that, for every value of x, as the variable y decreases/increases so does the performance function. This leads to the following relationships

$$\underline{g} = x_{\min}^2 \, \underline{y} + e^{x_{\min}}; \quad \overline{g} = x_{\max}^2 \, \overline{y} + e^{x_{\max}}; \tag{5.14}$$

where $x_{\min}$ and $x_{\max}$ are yet to be determined. On the other side, the performance function is not monotonic with respect to x. The sign of the first and second derivatives of g, says that the function is monotonically increasing with respect to x only in the portion where $y \in [-1.36, 0]$. Whereas, for $y \in (-\infty, -1.36) \cup (0, \infty)$ the function may have a minimum or maximum. Within the latter portion of domain, the minimum/maximum is identified solving for x the partial derivative $\partial g / \partial x$, and subsequently checking if the obtained value is smaller/greater than the values at the endpoints $\underline{x}$ and $\overline{x}$.

5.3.3.2 Solution to the back-propagation problem

The solution consists in collecting all those realisations in the input space that correspond to the response extrema. First the min-max propagation problem is solved and then all of the argument minima and maxima are collected back to the input space. These are also referred to as extreme realisations. The failure probability bounds,

$$\overline{p}_F = [\underline{p}_F, \ \overline{p}_F] = [0, \ 0.754],$$

are computed by means of direct Monte Carlo, i.e. using Eqs. (5.12) and (5.13) with 10^5 MC samples.

The strategy makes use the distributions of minima and maxima to reconstruct the corresponding upper and lower bounds of the failure probability. In Figures 5.8a and 5.8b the distribution of minima, corresponding to the upper failure probability, are compared with the extreme normal distributions of Table 5.6 for the maximum failure probability, obtained by solving the optimisation problem. In Figure 5.8b the normal distributions obtained using the parametric approach, that corresponds to the maximum failure probability of Table 5.6, are superimposed to the distributions of collected minima. The collected minima (Random Set approach) are not normally distributed and for the p-box of variable y (Figure 5.8b) they coincide with the left bounding CDF.

The solution to the back propagation problem can be found by searching the space of parental (normal) distribution functions for those hyper-parameters corresponding to the min/max failure probability. Within the non-parametric approach, this is done selecting the parental distribution functions that provide the best fit to the collected

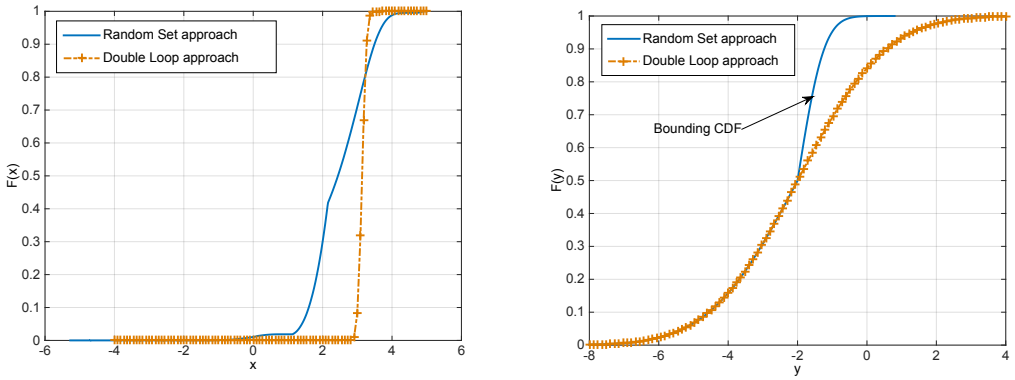

(a) x-CDFs **(b)** y-CDFs

Figure 5.8: Extreme realisations for the failure probability upper bound corresponding to Table 5.6 (Double Loop approach) and collected argument minima (Random Set approach)

P-box	$\min p_F^*$ $1.8\ 10^{-5}$	$\max p_F^*$ 0.468
x	$(\mu_x)^{\min *} =$ 4.97	$(\mu_x)^{\max *} =$ 2.43
x	$(\sigma_x)^{\min *} =$ 0.23	$(\sigma_x)^{\max *} =$ 0.60
y	$(\mu_y)^{\min *} =$ -0.51	$(\mu_y)^{\max *} =$ -1.98
y	$(\sigma_y)^{\min *} =$ 1.10	$(\sigma_y)^{\max *} =$ 1.07

Table 5.7: Failure probability bounds and corresponding extreme normal distributions obtained with the non-parametric approach

distributions of minima and maxima. Here, the normal distribution that best fits the extreme realisations is obtained using the Kolmogorov-Smirnov test, by minimizing the statistic (k-s distance) $D_{N_s} = \sup_x |F_{N_s}(x) - F(x)|$. The results from the k-s distance minimisation are shown in Table **??**. Figures 5.9a and 5.9b show the x and y extreme normal distributions that best fit the collected minima, which correspond to the failure probability upper bound. Note that the two normal distribution functions of extreme values obtained using the two approaches are quite similar. The failure probability bounds solution of the Random Set back propagation problem are shown in in Table **??**. These bounds appear to be included in the bounds of Table 5.6, therefore, they do not correspond to the normal distributions responsible for the minimum and maximum failure probability. By comparing the argument optima of Table 5.6 and **??**, variable x seems to be quite close to the optimal distribution, while for variable y only the mean value corresponding to maxp_F^* is close to the target of Table 5.6. Note, from Figure 5.9b, that the extreme realisations of variable y are distributed as the upper CDF, since the model is monotonic with respect to this variable.

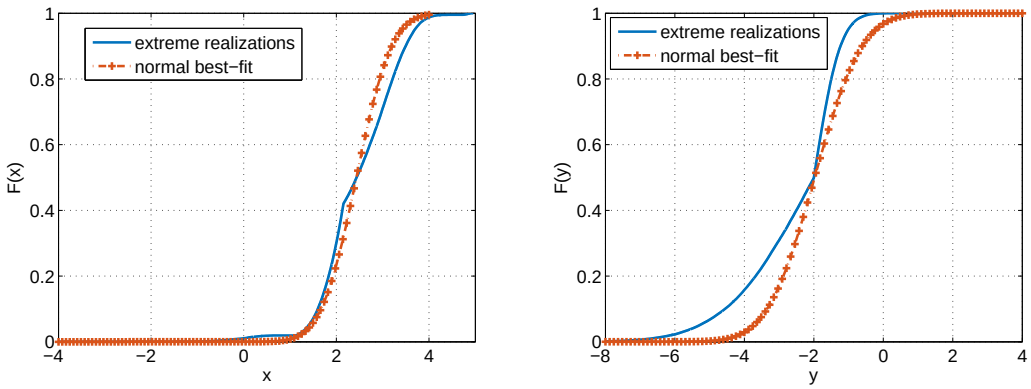

(a) x-normal distribution; best-fit obtained with a k-s distance of 0.11

(b) y-normal distribution; best-fit obtained with a k-s distance of 0.15

Figure 5.9: Extreme distributions for the failure probability upper bound obtained by fitting normal distributions to the collected minima

5.3.4 Final classification

From the analysis of the extreme realisations with both parametric and non-parametric approaches, it is possible to conclude that

- When the response is monotonic with respect to a p-box, the extreme realisations are distributed as the bounding CDFs of that p-box;
- When the response is not monotonic with respect to a p-box, the distribution function of the extreme realisations is enclosed in the bounding CDFs of that p-box and may have a complicated form;
- In general, the two reconstructed CDFs of the extreme realisations are not distributed as the parental model of probability;
- When the response is monotonic with respect to all p-boxes and when, for every p-box, the bounding CDFs are made of only two distribution functions (such as in the Beta model), the solution from the two approaches coincides.

5.4 Chapter summary

In this chapter, a novel Advanced Sampling strategy based on Line Sampling has been combined with the Random Set approach. The strategy has been tested on a simple numerical example, and further investigations on real engineering applications will be presented in the final chapter. The presented approach has shown not only to be very efficient, but also flexible as it can be adapted to any Advanced Sampling technique. The approach presented in this chapter and in Chapter 4, gained the IJAR silver award of ISIPTA15, targeted at young researchers who have demonstrated excellence in research

on imprecise probabilities. The results have been published in peer-reviewed conference papers (see, for example conference papers 3, 9 and 10 from the List of Publications), and have been presented at the 12th International Conference on Applications of Statistics and Probability in Civil Engineering (ICASP12), in July 2015.

Chapter 6

Forced Monte Carlo Strategy for the Robust Scheduling of Multiple Inspections with Random Sets

Advanced sampling techniques have demonstrated to be powerful tools to solve reliability problems with Random Sets. Another challenging problem in structural and system reliability, to be tackled with generalised uncertainty models, is the time dependent reliability problem. Every structure and system deteriorates with time and it is paramount to be able to assess the reliability at any given time. This extends to the challenging task of designing the optimal inspection schedule looking at the most economical solution, which can be found balancing the maintenance costs against the risk of failure.

The design of inspection schedules is a complex optimisation problem that requires the assessment of the system reliability. The solution to this problem can be found balancing the costs associated to inspection/repair activities against the benefits related to the faultless operation of the infrastructure. The objective is minimizing the total cost, obtained as the combination of maintenance costs and failure costs, while tuning some parameters, such as the number, time and quality of inspections.

The optimisation problem is formulated as a time-dependent reliability-based optimisation problem, where both objective and constraint functions require the evaluation of upper and lower reliability bounds. The solution to this problem represents a real technological challenge, as the reliability assessment by means of Random Set is a computationally intensive task, which may take up to a few days to be completed on common processing units. In this chapter, an efficient and generally applicable and efficient numerical technique is proposed. The technique, integrated in OpenCossan, combines an Importance Sampling method derived from the concept of forced Monte Carlo simulation, with an optimisation strategy, which makes the interval reliability estimation particularly efficient.

6.1 Introduction

Preventive maintenance practice can be extremely cost-effective for mitigating damage accumulation of civil infrastructures. In fact, inspection and repair activities may prevent loss of serviceability or even partial collapse. However, making decisions as to whether and when to perform inspections is a very complex task, especially on real-scale engineering systems [83]. In fact, the realistic quantification of costs associated with inspections, repair and failure (i.e. loss of serviceability), requires the explicit consideration of the unavoidable uncertainties arising from the damage-propagation process, and from the inspection and repair activities.

Uncertainties may come from the inherent variability of the damage-propagation process or from the lack of available knowledge about the process itself. Random Sets are used as a comprehensive means of representing such heterogeneous uncertainties. Such an uncertainty model is quite general, and permits to assess the reliability and sensitivity of the computational model with respect to the uncertainty. In other words, the use of Random Sets adds robustness to the reliability analysis, making the analyst more aware of the effects of the uncertainties on the model response.

Reliability-based optimisation methods and techniques, as described e.g. in [32], are invoked to solve the problem.

Due to the explicit consideration of uncertainties, the design of maintenance activities is an optimisation task that requires the assessment of reliability where number, times, and quality of inspections are the design variables and the total cost is the objective function. For the formulation and solution to time-dependent reliability-based optimisation problems see e.g. [55] and [70]. The assessment of reliability both in the objective and in the constraints functions, and the consideration of multiple inspections, make this a stochastic discrete optimisation problem, which can be quite challenging to solve [75].

In this chapter, a general methodology for the efficient solution of the time-variant reliability-based maintenance optimisation problem is proposed, which is applicable to any case where the damage propagation law is known as input-output relationship. No restrictions in terms of number of inspections and number of uncertain parameters can be found. The methodology is derived from the concept of forced Monte Carlo simulation, used to evaluate the availability of plants [82], and it is exploited to efficiently assess the time-variant reliability conditional to the inspection outcomes, requiring only the execution of computationally inexpensive functions.

Here, Genetic Algorithms are used to drive the global optimisation, as the cost and constraint functions are stochastic and therefore, no information about the derivatives can be efficiently used to converge to the minimum. This comes with quite some additional numerical burden, which, however, can be significantly alleviated resorting to code parallelization.

6.1.1 Advantages of the proposed methodology

Two main advantages are identified, which make the methodology particularly efficient:

- Only one full reliability analysis is required to estimate upper and lower failure probability bounds until the mission time (or time of interest). In practice, each failure probability bound can be estimated at any inspection time without repeating a full analysis, hence making use of the results obtained from the full reliability analysis. This turns out to be very useful, as reliability has to be assessed multiple times to find the optimum time point to perform the inspections.

- The proposed methodology can be easily parallelised allowing the efficient evaluation of the cost function.

6.2 Optimisation of maintenance costs

Given a system that evolves in time, a mission time, T_M, which is the time until when the system is required to function as specified, and a number of inspections, N, performed at times, $\boldsymbol{t}^{\text{insp}} \in \mathbb{R}^N$, the maintenance problem is formulated as an optimisation task, where both objective and constraints require the evaluation of the reliability, $r(t)$.

Three main different costs can be identified:

- manufacturing (or initial) costs, C_0,

- costs of inspection, C_I,

- costs of repair C_R

- costs of failure, C_F.

It is assumed that manufacturing costs are deterministic, as they are linked to construction and usage of materials. Note that, as pointed out in [71], the costs of repair and failure will be obtained as expected values, $E[\cdot]$, as they are linked to the repair and failure probability, respectively.

6.2.1 Costs due to inspections and repair

The cost due to inspections depends on inspection quality, q, and on the inspection times, $\boldsymbol{t}^{\text{insp}}$, and can be expressed as

$$E[C_I(q, \boldsymbol{t}^{\text{insp}})] = c_I \; q \; \eta(\boldsymbol{t}^{\text{insp}}); \tag{6.1}$$

where c_I is a fixed unit cost, and q, see Eq. (6.3), quantifies the quality of inspections. In the Eq. (6.1) the function

$$\eta(t) = \frac{1}{(1+s)^t}; \tag{6.2}$$

actualises the costs to the time of the analysis. As inspection activities do not reveal damage with certainty, the probability of repair, $p_R(q,t)$, is linked to the probability of detecting the damage within an inspection, POD, which in turns depends on the inspection quality, q, the level of damage, $D(t)$, and the technique used to spot the flaw. For example, as a means of controlling damage associated with crack propagation, in fatigue-prone metallic components, non-destructive inspection (NDI) techniques can be used. NDI techniques have an associated probability of detection [81], which can be modeled as

$$POD(t) = (1-p_0)\ (1 - \mathrm{e}^{\ q\ (f_1 - f_2\ D(t))}); \tag{6.3}$$

where, p_0, is the probability of not detecting a large crack, while f_1 and f_2 are parameters that depend on the specific NDI technique. Note the probability of detection is calculated based on two factors: the first one, $1-p_0$, measures the probability of detecting a large crack; while the second factor, $1 - \mathrm{e}^{\ q\ (f_1 - f_2\ D(t))}$, can be interpreted as a coefficient between 0 and 1 that is a function of the state of damage (or crack length for the specific case), $D(t)$. The expected cost of repair can be expressed as

$$E[C_R(q, \boldsymbol{t}^{\text{insp}})] = c_R\ p_R(q, \boldsymbol{t}^{\text{insp}})\ \eta(\boldsymbol{t}^{\text{insp}}); \tag{6.4}$$

where, c_R is a fixed unit cost, and p_R is, clearly, a function of the inspection times. Note that the unit cost of repair can be very small or sometimes negligible compared to the cost of inspection.

6.2.2 Costs of failure

The cost of failure depends on the state of damage, $D(t)$, as it is assumed proportional to the failure probability of the system, as well as on the inspection quality, q, . Here, failure cost is expressed as

$$E[C_F(q, \boldsymbol{t}^{\text{insp}}, t)] = c_F\ p_F(q, \boldsymbol{t}^{\text{insp}}, t); \tag{6.5}$$

where, c_F is a fixed unit cost associated with failure, partial collapse, or unavailability, and $p_F(q, \boldsymbol{t}^{\text{insp}}, t)$ is the failure probability, calculated as in Section 6.3. Note that the failure probability depends on both the inspection times, $\boldsymbol{t}^{\text{insp}}$, and on the time when the reliability is assessed, t, as will be explained in the next section.

6.2.3 Total costs

The expected total cost is the sum of all expected costs

$$E[C_T] = C_0 + C_I(q, \boldsymbol{t}^{\text{insp}}) + E[C_R(q, \boldsymbol{t}^{\text{insp}})] + E[C_F(q, \boldsymbol{t}^{\text{insp}}, t)]; \tag{6.6}$$

including the initial manufacturing cost C_0, for simplicity assumed to be deterministic. The remaining combination of costs, including repair, inspection and failure equalises the total cost of maintenance

$$E[C_M] = E[C_I(q, \boldsymbol{t}^{\text{insp}})] + E[C_R(q, \boldsymbol{t}^{\text{insp}})] + E[C_F(q, \boldsymbol{t}^{\text{insp}}, t)]. \tag{6.7}$$

6.2.4 Formulation of the optimisation problem

The maintenance problem is formulated as a constrained optimisation problem, where the constraint is the limit state safety level that the system has to comply with. Here, the following formulation of the optimisation problem is considered

$$\begin{aligned} \underset{q\in\mathbb{R}^+,\ \boldsymbol{t}^{\text{insp}}\in[0,T_M]^N}{\text{minimize}} \quad & E[C_M(q, \boldsymbol{t}^{\text{insp}}, t)] \\ \text{subject to} \quad & p_F(q, \boldsymbol{t}^{\text{insp}}, t) \leqslant p_F^{\text{critic}}; \end{aligned} \tag{6.8}$$

where, p_F^{critic} is determined by a prescribed limit state safety level. Eq. (6.8) is solved using the penalty function

$$\psi(c) = 1 - e^{\alpha|\min(0,c)|}; \tag{6.9}$$

which is a function of the constraint

$$c = -\log_{10}\left(p_F(q, \boldsymbol{t}^{\text{insp}}, t)\right) + \log_{10}\left(p_F^{\text{critic}}\right); \tag{6.10}$$

where, the constraint is satisfied if $c > 0$. The problem of Eq. (6.8) can, thus, be reformulated into an approximate unconstrained problem, as

$$\underset{q\in\mathbb{R}^+,\ \boldsymbol{t}^{\text{insp}}\in[0,T_M]^N}{\text{minimize}} \quad E[C_M(q, \boldsymbol{t}^{\text{insp}}, t)] + g\ \psi(c); \tag{6.11}$$

where, g is a penalty factor, whose value can be chosen knowing the order of magnitude of the minimum value of the objective function.

6.3 Efficient forced Monte Carlo for the estimation of time-variant reliability conditional to inspection

The computation of reliability is usually associated with quite a significant computational effort. Among the numerical methods proposed in literature, Monte Carlo (MC)

simulation methods [39] are generally applicable, but require a compromise between efficiency and accuracy. Many variants of the MC method can be found in literature [61,82], such as Line Sampling [21], Importance Sampling [8] and Subset simulation [9], which make the MC method more efficient and accurate. Advanced simulation is an essential component of the proposed development to ensure efficiency.

The present numerical strategy is derived from the concept of forced MC simulation described in [82]. The strategy is based on the computation of weights, w, which account for the probability of detection, and can be computed at any inspection time by reusing the results from the same reliability analysis.

6.3.1 Time-variant reliability and failure probability estimation

As the system, $S(t)$, evolves in time, so does the level of damage, D, of specific components. The damage can be expressed as a function, $D = D(\boldsymbol{\theta}, t) = D_{\boldsymbol{\theta}}(t)$, of some input parameters $\boldsymbol{\theta}$, that can be used to quantify the level of damage. For example, damage may manifest in the form of fatigue, where the model is represented by the Paris-Erdogan's law [48], and $\boldsymbol{\theta}$ includes the initial crack length (initial condition), the stress range, the shape factors, the crack length ratio and any other coefficients of the damage law. The time-variant reliability is obtained via definition of a critical threshold of damage, $D_{\boldsymbol{\theta}}^{\text{thres}}$, as

$$r(t) = 1 - P[D_{\boldsymbol{\theta}}(t) \geqslant D_{\boldsymbol{\theta}}^{\text{thres}}]; \tag{6.12}$$

where the threshold $D_{\boldsymbol{\theta}}^{\text{thres}}$, and the damage level, $D_{\boldsymbol{\theta}}(t)$, also represent, in an extended context, the capacity and the demand of the system, respectively. Both $D_{\boldsymbol{\theta}}^{\text{thres}}$ and $D_{\boldsymbol{\theta}}(t)$ are uncertain quantities with associated probability distribution functions. The time-variant reliability is obtained as

$$r(t) = 1 - \int_{D(\boldsymbol{\theta},t) \geqslant D^{\text{thres}}} h(\boldsymbol{\theta}) \, \mathrm{d}\boldsymbol{\theta}; \tag{6.13}$$

where h is the joint density function of the random parameters $\boldsymbol{\theta}$. For simplicity, the structural capacity, $D_{\boldsymbol{\theta}}^{\text{thres}}$, has been included in the vector of parameters, $\boldsymbol{\theta}$. By means of the Monte Carlo method, the time-variant failure probability, $p_F(t)$, can be calculated as

$$p_F(t) = \int_{-\infty}^{\infty} \cdots \int_{-\infty}^{\infty} \mathcal{I}(\boldsymbol{\theta}, t) \; h(\boldsymbol{\theta}) \, \mathrm{d}\boldsymbol{\theta}; \tag{6.14}$$

where, $\mathcal{I}(\boldsymbol{\theta}, t) \in \{0, 1\}$ is the indicator function, which is 1 only if $D(\boldsymbol{\theta}, t) \geqslant D^{\text{thres}}$.

6.3.2 Formulation of the maintenance problem

The maintenance problem requires the evaluation of the reliability, $r(t)$, over the period of time, $t \in [0, \; T_M]$. With no inspections ($N = 0$), the problem can be solved by assessing the reliability as in Eq. (6.13) or (6.14).

When inspections are considered, i.e. $N > 0$, the reliability of the system is conditional on the inspection outcomes. In fact, after an inspection, the system/component can be regenerated, as repair activities may take place. Therefore, the inspection outcomes and eventual repair need to be taken into account by computing the conditional reliability.

The optimal inspection time is naturally between the following two limiting cases. If inspections are performed too early, $\boldsymbol{t}^{\text{insp}} << T_M$, nearly no damage will be found, and hence no repair will take place. As a consequence, the reliability will only be improved marginally, or even not improved at all. On the other hand, if inspections are undertaken too late, $\boldsymbol{t}^{\text{insp}} \simeq T_M$, the probability of detection would be large, because directly related to the level of damage, but it is also very likely that the system will have already failed, making the inspection ineffective. The reliability is a function of two different times: the actual time t, when the reliability is assessed, and the inspection times $\boldsymbol{t}^{\text{insp}}$, when the inspections have been performed. In general, i.e. when N inspections are considered, the reliability is given by the conditional probability,

$$r(t) = 1 - P\left[D(t) \geqslant D^{\text{thres}} \mid t_1^{\text{insp}} < t_2^{\text{insp}} < ...t_N^{\text{insp}} < t\right]. \tag{6.15}$$

Here, the focus is on assessing the reliability at a fixed time point, i.e. for example at the mission time $t = T_M$.

6.3.2.1 Assumptions

In order to illustrate the procedure some working assumptions are considered for simplifying the discussion, but without restricting the generality of the approach:

1. Any inspection is followed by only two outcomes: either the flaw is detected or not. If a flaw is detected, repair takes place, and that action is assumed to be perfect, i.e. after repair $D(t^{\text{insp}}) = 0$. In other words, if a component is repaired, it is assumed that further chances of failure for that specific component are zero.

2. Only preventive maintenance is considered. If the critical threshold is exceeded at the time of inspection, the component cannot be repaired. That is, if failure has occurred, repair actions will not take place.

Both working assumptions can be removed with no additional computational cost. The first assumption can be removed simply by shifting the mission time backwards thus, without any additional computational cost, while removing the second assumption will lead to a change towards a corrective maintenance paradigm. Repair and failure events are closely related, as they are both linked to the state of damage. For instance, if the damage is close to the critical threshold, it is very likely that either the failure or the repair event occurs.

6.3.2.2 Classification of events and total failure probability

In order to calculate the reliability as defined in Eq. (6.15), mutually exclusive events are classified and combined together. Among all of the possible events, four main classes are identified:

- the failure events, $F_i = [D(t_i^{\text{insp}}) > D^{\text{thres}}]$, at the time of the i-th inspection,
- the failure event, $F_t = [D(t) > D^{\text{thres}}]$, at the evaluation time t,
- the repair/detection event, $R_i = [\delta(t_i^{\text{insp}}) = 1]$, at the time of the i-th inspection,
- the event $\overline{R_i} = [\delta(t_i^{\text{insp}}) = 0]$, i.e. the event of non-repair/non-detection;

where δ is a binary random variable to characterise the outcome of inspections, as it will be explained in the next section.

The failure event, F, given that N inspections are performed, can be expressed by means of operations of union and intersection among events.

The failure event is represented as a combination of mutually exclusive events

$$F = \bigcup_{j=1}^{N+1} \left(\left(F_{N-j+2} \cap \overline{F_{N-j+1}}\right) \cap \bigcap_{k=0}^{N-j+1} \overline{R_k} \right); \tag{6.16}$$

where, for simplified notation, the event, $F_{N+1} = F_t$, is put equal to the failure event at the evaluation time. In Eq. (6.16), the intersection of consecutive failure events is

$$F_{i+1} \cap \overline{F_i} = [D(t_{i+1}^{\text{insp}}) > D^{\text{thres}} \text{ AND } D(t_i^{\text{insp}}) < D^{\text{thres}}]. \tag{6.17}$$

In Eq. (6.16), it is assumed that any event, where the subscript is $\leqslant 0$, is the empty set, $\varnothing$. So, for example, the event $\overline{R_k}$, obtained for $k = 0$, is the empty set $\overline{R_0} = \varnothing$.

The consideration of mutually exclusive events, as shown in Eq. (6.16), leads to the general expression of the total failure probability

$$P[F] = \sum_{j=1}^{N+1} P\left[F_{N-j+2} \cap (\overline{F_{N-j+1}})\right] \prod_{k=0}^{N-j+1} P\left[(\overline{R_k})\right]; \tag{6.18}$$

where, again for simplicity, the summation goes from 1 to $(N+1)$ to include the failure event at the time of observation $F_t = F_{N+1}$.

Eq. (6.18) could be analytically solved, only if both the damage-propagation law of Eq. (6.3), and the detection probability function of Eq. (6.3), had a closed form solution. However, in general, this is not available, because the damage-propagation equation is often implicitly solved (for example using a step forward integration approach), thus, the probability of Eq. (6.18) has to be numerically calculated.

6.3.3 The direct Monte Carlo approach

One way to solve the problem formulated in Eq. (6.18) is by performing a direct MC simulation.

6.3.3.1 The direct MC approach with one inspection (N=1)

A binary variable, $\delta_{\boldsymbol{\theta}}(t)$, to characterise the outcomes of inspections is introduced. The variable has the following mass function

$$f_{\Delta}(\delta_{\boldsymbol{\theta}}(t)) = \begin{cases} \lambda_D & \delta_{\boldsymbol{\theta}}(t) = 1 \text{ (success)} \\ 1 - \lambda_D & \delta_{\boldsymbol{\theta}}(t) = 0 \text{ (failure)} \end{cases}; \tag{6.19}$$

where, $\lambda_D = POD(D_{\boldsymbol{\theta}}(t))$ is the likelihood of detecting the flaw during inspection.

The failure probability is computed by means of MC as

$$p_F(t) = \lim_{N_S \to \infty} \frac{1}{N_S} \sum_{s=1}^{N_S} \int_0^{+\infty} \left(\delta_{\boldsymbol{\theta}}(t_1)^{\{s\}} \, \mathcal{I}(\boldsymbol{\theta}, t_1) + (1 - \delta_{\boldsymbol{\theta}}(t_1)^{\{s\}}) \, \mathcal{I}(\boldsymbol{\theta}, t) \right) f_{\Theta}(\boldsymbol{\theta}) \, \mathrm{d}\boldsymbol{\theta}; \tag{6.20}$$

where, $t_1 = t_1^{\text{insp}}$, $f_{\Theta}(\boldsymbol{\theta})$ is the joint density function, and $\delta_{\boldsymbol{\theta}}(t_1)^{\{s\}} \in \{0,\ 1\}$ simulates the outcome of the first inspection for the $\{s\}$-th sample. The indicator function in Eq. (6.20) is

$$\mathcal{I}(\boldsymbol{\theta}, t) = \begin{cases} 1, & \text{if} \quad D_{\boldsymbol{\theta}}(t) \geqslant D^{\text{thres}} \\ 0, & \text{otherwise} \end{cases}; \tag{6.21}$$

An extract of the pseudo-code that computes the integrand of Eq. (6.20) is shown in Figure 6.1. The time-variant failure probability estimator is computed by averaging over a large number of samples, N_S, as

$$\hat{p}_F(t) = \frac{1}{N_S} \sum_{s=1}^{N_S} \left(\delta_{\boldsymbol{\theta}}(t_1)^{\{s\}} \, \mathcal{I}(\boldsymbol{\theta}^{\{s\}}, t_1) + (1 - \delta_{\boldsymbol{\theta}}(t_1)^{\{s\}}) \, \mathcal{I}(\boldsymbol{\theta}^{\{s\}}, t) \right). \tag{6.22}$$

6.3.3.2 The direct MC approach with multiple inspections (N>1)

The method can be extended to multiple inspections as a derivation of Eq. (6.18). Let $\boldsymbol{\delta}^{\{s\}} = \delta_{\boldsymbol{\theta}}(t_1)^{\{s\}}, ..., \delta_{\boldsymbol{\theta}}(t_N)^{\{s\}}$ be the vector of inspection outcomes for the $\{s\}$-th sample. The total failure probability can be calculated as

$$\begin{aligned} p_F(t) \quad = \quad & \lim_{N_S \to \infty} \frac{1}{N_S} \sum_{s=1}^{N_S} \int_0^{+\infty} \left(\sum_{i=1}^{N} \left(1 - \left(1 - \delta_i^{\{s\}} \right) \mathcal{I}(\boldsymbol{\theta}, t_i) \, \mathcal{I}(\boldsymbol{\theta}, t_{i+1}) \right) \prod_{k=0}^{i-1} \left(1 - \delta_k^{\{s\}} \right) \right. \\ & \left. + \mathcal{I}(\boldsymbol{\theta}, t) \prod_{k=1}^{N} (1 - \delta_k^{\{s\}}) \right) f_{\Theta}(\boldsymbol{\theta}) \, \mathrm{d}\boldsymbol{\theta}; \end{aligned} \tag{6.23}$$

begin
$D(t^{\text{insp}}) = D(\boldsymbol{\theta}, t^{\text{insp}})$ % compute crack length at inspection time
if $D(t^{\text{insp}}) \geqslant D^{\text{thres}}$ **then**
  $\mathcal{I} = 1$ % failure occurs before inspection
else
  $\lambda_D = POD(D(t^{\text{insp}}))$ % compute the likelihood of detection
  $\delta \sim \{0,\ 1\}_{\lambda_D}$ % simulate the outcome of inspection
  if $\delta = 0$ **then**
    $D(t) = D(\boldsymbol{\theta}, t)$ % compute crack length at the evaluation time
    if $D(t) \geqslant D^{\text{thres}}$ **then**
      $\mathcal{I} = 1$ % component has failed
    else
      $\mathcal{I} = 0$ % component has not failed
    end if
  end if
end if
end

Figure 6.1: Pseudocode for the failure probability estimator of Eq. (6.22), case with N=1

where, the time t_{N+1} coincides with the evaluation time as $t_{N+1} = t$, and for $k = 0$, the variable $\delta_{k=0}^{\{s\}} = 0$.

The integrand of Eq. (6.23) can be easily coded by means of nested "if" statements, as shown in the pseudo-code of Figure 6.2.

The time-variant failure probability estimator is computed, again, by averaging over a large, albeit finite, number of samples, N_S, as

$$\begin{aligned}\hat{p}_F(t) \quad = \quad & \frac{1}{N_S}\sum_{s=1}^{N_S}\left(\sum_{i=1}^{N}\left(1-\left(1-\delta_i^{\{s\}}\right)\ \mathcal{I}(\boldsymbol{\theta}^{\{s\}},t_i)\ \mathcal{I}(\boldsymbol{\theta}^{\{s\}},t_{i+1})\right)\prod_{k=0}^{i-1}\left(1-\delta_k^{\{s\}}\right)\right. \\ & \left.+\mathcal{I}(\boldsymbol{\theta}^{\{s\}},t)\prod_{k=1}^{N}\left(1-\delta_k^{\{s\}}\right)\right). \end{aligned} \tag{6.24}$$

6.3.4 The forced MC simulation approach

Here, we propose a numerical approach to calculate the reliability conditional to inspections without the need for contextually simulating the inspection outcomes. This constitutes a great advantage, as, unlike in the direct case, it is no longer necessary to run a full reliability analysis for every inspection time. Such an approach is also called forced MC simulation, as the inspection outcomes are simulated all at once, before the full simulation of the system takes place. In this way the simulation of the system is decoupled from the simulation of inspections, with the great computational advantage of having to run only one full system simulation (or reliability analysis).

```
begin
D(t^insp) = D(θ, t^insp)   %  compute crack length at inspection times
δ ~ {0, 1}_{λ_D}           %  simulate the outcome of inspections
I = 0                              %initialize indicator function
if D(t_1^insp) ⩾ D^thres then
  I = 1                    %   failure occurs before first inspection
else
  if δ_1 = 0 then
    if D(t_2^insp) ⩾ D^thres then
      I = 1                %   component has failed
    else
      if δ_2 = 0 then
        ...
        if δ_N = 0 then
          D(t) = D(θ, t)   %  compute crack length at the evaluation time
          if D(t) ⩾ D^thres then
            I = 1          %   component has failed
          else
            I = 0          %   component has not failed
          end if
        end if
        ...
      end if
    end if
  end if
end if
end
```

Figure 6.2: Pseudocode for the failure probability estimator of Eq. (6.22), for the case of multiple inspections (N>1).

6.3.4.1 The forced approach with one inspection (N=1)

The strategy can be derived from Eq. (6.20), noting that the random variable $\delta(t_1)^{\{s\}}$ can be averaged before the integral is calculated, as

$$p_F(t) = \int_0^{+\infty} \lim_{N_S \to \infty} \frac{1}{N_S} \sum_{s=1}^{N_S} \left(\delta(t_1)^{\{s\}} \, \mathcal{I}(\boldsymbol{\theta}, t_1) + (1 - \delta(t_1)^{\{s\}}) \, \mathcal{I}(\boldsymbol{\theta}, t) \right) f_\Theta(\boldsymbol{\theta}) \, \mathrm{d}\boldsymbol{\theta}; \tag{6.25}$$

which, is equivalent to averaging over the inspection outcomes before the reliability analysis is actually performed. Subsequently, we note that the limit is equal to the expected value of the detection probability as

$$w(t) = \lim_{N_S \to \infty} \frac{1}{N_S} \sum_{s=1}^{N_S} \delta(t)^{\{s\}} = POD\left(D(\boldsymbol{\theta}, t)\right). \tag{6.26}$$

By introducing the weight w, from Eq. (6.26), the time-variant failure probability can now be calculated as

$$p_F(t) = \int_0^{+\infty} \left(w(t_1) \, \mathcal{I}(\boldsymbol{\theta}, t_1) + (1 - w(t_1)) \, \mathcal{I}(\boldsymbol{\theta}, t) \right) f_\Theta(\boldsymbol{\theta}) \, \mathrm{d}\boldsymbol{\theta}; \tag{6.27}$$

The estimator of the failure probability, obtained by means of MC with a large sample size, is

$$\hat{p}_F(t) = \frac{1}{N_S} \sum_{s=1}^{N_S} \left(\hat{w}(t_1) \, \mathcal{I}(\boldsymbol{\theta}^{\{s\}}, t_1) + (1 - \hat{w}(t_1)) \, \mathcal{I}_M(\boldsymbol{\theta}^{\{s\}}, t) \right). \tag{6.28}$$

Note, from the pseudo-code of Figure 6.1, that the weight w is in fact, the relative frequency (relative to the number of runs N_S) by which the logical statement "if $\delta = 1$" returns true response. This relative frequency, when $N_S \to \infty$, converges to the likelihood of detection $\lambda_D(t_1) = POD\left(D(\boldsymbol{\theta}, t_1)\right)$.

6.3.4.2 The forced approach with multiple inspections (N>1)

The approach is generalized to multiple inspections, by computing the detection weights from Eq. (6.26), by referring to the i-th inspection as

$$w_i = \lim_{N_S \to \infty} \frac{1}{N_S} \sum_{s=1}^{N_S} \delta_i^{\{s\}} = POD(D(\boldsymbol{\theta}, t_i)). \tag{6.29}$$

Again, by averaging over the inspection outcomes before the integral, and substituting the weights of Eq. (6.29), Eq. (6.23) becomes

$$p_F(t) = \int_0^{+\infty} \left(\sum_{i=1}^{N} \mathcal{I}(\boldsymbol{\theta}, t_i) \left(1 - (1 - w_i)\, \mathcal{I}(\boldsymbol{\theta}, t_{i+1})\right) \prod_{k=0}^{i-1} (1 - w_k) + \mathcal{I}(\boldsymbol{\theta}, t) \prod_{k=1}^{N} (1 - w_k) \right) f_\Theta(\boldsymbol{\theta})\, \mathrm{d}\boldsymbol{\theta}; \tag{6.30}$$

where, for simplified notation $t_{N+1} = t$. The failure probability estimator is obtained by means of MC, with a large sample set, as

$$\hat{p}_F(t) = \frac{1}{N_S} \sum_{s=1}^{N_S} \left(\sum_{i=1}^{N} \mathcal{I}(\boldsymbol{\theta}^{\{s\}}, t_i) \left(1 - (1 - \hat{w}_i)\, \mathcal{I}(\boldsymbol{\theta}^{\{s\}}, t_{i+1})\right) \prod_{k=0}^{i-1} (1 - \hat{w}_k) + \mathcal{I}(\boldsymbol{\theta}^{\{s\}}, t) \prod_{k=1}^{N} (1 - \hat{w}_k) \right). \tag{6.31}$$

An alternative way to compute Eq. (6.31), which can be vectorized in a computer code, is

$$\hat{p}_F(t) = \frac{1}{N_S} \sum_{s=1}^{N_S} \left(\mathcal{I}(\boldsymbol{\theta}^{\{s\}}, t) \prod_{j=1}^{N} 1 - \hat{w}_j \left(1 - \mathcal{I}(\boldsymbol{\theta}^{\{s\}}, t_j)\right) \right); \tag{6.32}$$

where, as a matter of fact, and unlike Eq. (6.24) and Eq. (6.31), the latter equation can be computed without a "for" loop over the number of inspections.

6.3.5 Total and partial probability of repair

By means of the direct approach, the probability of repair can be calculated for the i-th inspection as

$$p_{R_i} = \lim_{N_S \to \infty} \frac{1}{N_S} \sum_{s=1}^{N_S} \prod_{k=1}^{i} \delta_k^{\{s\}}. \tag{6.33}$$

Again, by inverting the order of summation and product sequence, the probability of repair for the i-th inspection can be estimated as

$$p_{R_i} = \lim_{N_S \to \infty} \prod_{k=1}^{i} \frac{1}{N_S} \sum_{s=1}^{N_S} \delta_k^{\{s\}} = \prod_{k=1}^{i} E\left[w_k\right]. \tag{6.34}$$

The estimator for the total probability of repair, i.e. after all the inspections have been performed, is obtained with a finite sample set as

$$\hat{p}_R = \prod_{k=1}^{N} \hat{w}_k. \tag{6.35}$$

6.4 Chapter summary

In this chapter, a general and efficient methodology for the scheduling of multiple inspections has been presented. The maintenance of a system is a challenging engineering task, where the estimation of costs requires the consideration of heterogeneous uncertainties arising from the damage propagation process and from the inspection/repair activities. The cost of failure has to be quantified at any given time in order to be able to find an optimal inspection time. This requires the time dependent reliability function of the system to be invoked many times during the optimization process. It is thus, essential to be able to compute the reliability of the system in an efficient way. A forced Monte Carlo (MC) simulation strategy is proposed to enhance the efficiency, without reducing accuracy. The efficiency is increased using a strategy that simulates the inspection outcomes aside of the whole simulation, making it possible to simulate the system state at any time with no additional calculations. The two simulations are then put back together using a vector of weights analytically calculated to simulate the inspection outcomes. The strategy is named forced MC from the fact that the simulation of the inspection outcomes is force-performed aside of the full system simulation. The efficiency of the MC strategy has enabled an extension beyond the classical probabilistic modelling of uncertainties. The proposed strategy is capable of assessing failure probability upper and lower bounds, accounting for imprecision. By means of the developed methodology it is possible to keep aleatory and epistemic uncertainty separated. The epistemic uncertainty is propagated by looking at the maximum and minimum system response at any given time. Lower and upper reliability bounds are then obtained referring to the state of the system corresponding to the maximum and minimum response. In this way, it is possible to use Random Sets to define the input uncertainties. In terms of computational cost, only two full reliability analyses are required to assess upper and lower bounds at any given time and for any number of inspections. The efficiency, scalability and applicability of the proposed methodology will be demonstrated in the next chapter via an example involving twelve variables.

Chapter 7

Robust Scheduling of Multiple Inspections: Application to a Fatigue-prone Metallic Structure

In this chapter a welded connection of a bridge girder is analysed. Due to cyclic loading, metallic components tend to develop fatigue cracks. As these cracks propagate, the structural system accumulates damage that may lead to loss of serviceability or even to collapse, which are followed by considerable monetary losses.

The welded connection between a web stiffener and the girder's flange is taken from [37]. Welds are particularly weak to damage accumulation, as imperfections may form and grow under cyclic loading. The analysed weld with associated defect is shown in Figure 7.1. From the picture, it can be appreciated that the crack propagates from the weld toe towards the bottom, undermining the integrity of the structural connection. The crack propagation phenomenon is modelled using the Paris-Erdogan law, by means of

$$\frac{\mathrm{d}a}{\mathrm{d}N} = C\,(\Delta K)^m\,; \tag{7.1}$$

where, a is the crack length, N is the number of loading cycles, ΔK is the stress intensity factor range, and C and m are two material parameters. In this study, no threshold limits the ΔK values, thus, it is assumed that all loading cycles count on damage. Eq. (7.1) is solved implicitly by means of numerical integration. The stress intensity factor range is a function of the crack length

$$\Delta K = Y(a)\ M(a)\ \Delta S\ \sqrt{\pi a}; \tag{7.2}$$

where, $Y(a)$ is the stress intensity correction factor, and $M(a)$ is the stress concentration factor, which are also functions of the crack shape, a/c, the flange thickness, b, the flange width w, the weld height, h, and the weld angle, ϕ (see e.g. Figure 7.1). In order to

Table 7.1: Mission time and annual frequency

	Value	Unit	Description
$E[\nu]$	4.5	$[10^6$cycles/year$]$	Annual number of cycles
T_M	50	[years]	Mission time

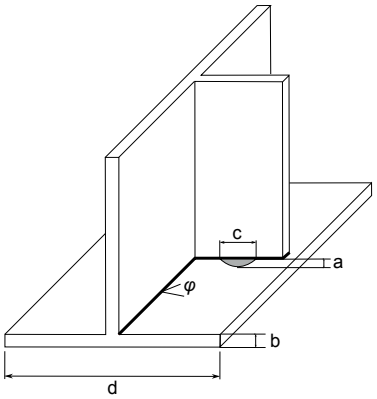

Figure 7.1: Illustration of structural detail and crack

solve Eq. (7.1) a target life time (or mission time), T_M, of the structural component has to be selected, as shown in Table 7.1. From the rain-flaw histogram (loading analysis) it is possible to derive the annual number of cycles, ν, which multiplied by the target life time, in years, provides the total number of cycles at the mission time. Thus, the number of cycles at the target life time is $N_{max} = \nu \cdot T_M$.

7.1 Estimation of total failure probability with one inspection

When one single inspection is performed, the problem of estimating the failure probability can be visualized, as shown in Figure 7.2. The failure probability is computed with one inspection performed at time $t^{\text{insp}} = 1.5 \cdot 10^6$ cycles. For the purpose of illustration, the uncertainty is assigned to the initial crack length, a_0, only. A bundle of curves (see Figure 7.2) is simulated during the reliability analysis, where each curve is obtained solving, for each sample, the crack-growth relationship of Eq. (7.1).

Figure 7.2 illustrates the procedure to calculate the weights, using the forced Monte Carlo simulation approach. The graph of Figure 7.2(a) shows the probability of detection (x-axis) as a function of the level of damage. For every sample of the reliability analysis a curve of the level of damage, a, is plotted as a function of time. At the end of the reliability analysis the graph in Figure 7.2(b) is obtained. In order to calculate the weights, a line is superimposed to both graphs corresponding to the POD at time

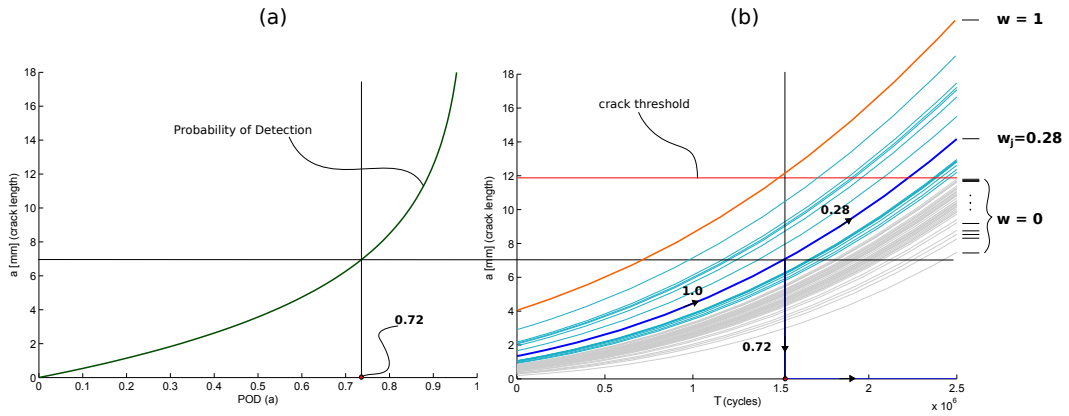

Figure 7.2: Diagram for the calculation of weights and failure probability conditional to the outcome of one inspection

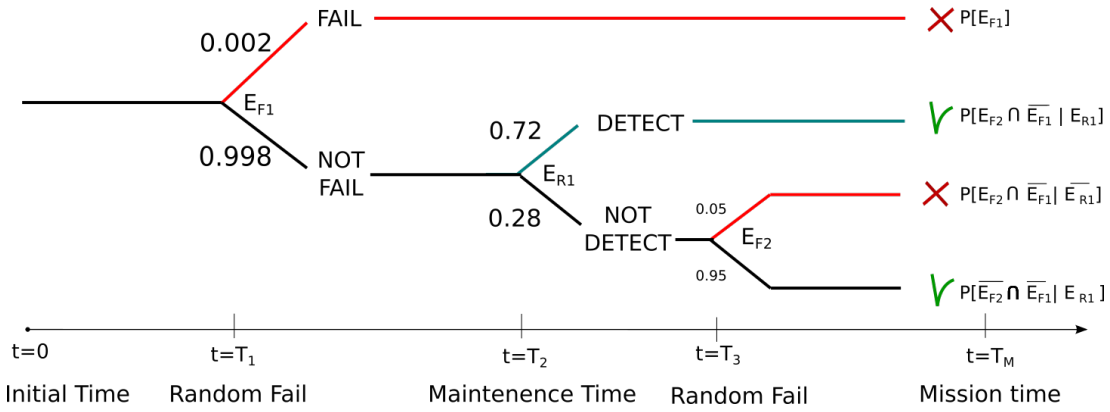

Figure 7.3: Tree chart for the calculation of the failure probability conditional to the outcome of one inspection

$t = 1.5 \cdot 10^6$ cycles. On the graph of Figure 7.2(b) the selected curve is tracked with probability 1 until inspection occurs. Following inspection we have two possible states with associated probabilities: either the detection is successful (with probability 0.72) and the damage is removed $a(t \geqslant t^{\text{insp}}) = 0$, or the detection fails and the damage keeps growing until the evaluation time $t = 2.5 \cdot 10^6$ cycles. The probability of non-detection (0.28) is the weight to be assigned to the sample under consideration. The procedure is then repeated for every curve that fails at the evaluation time ($t = 2.5\ 10^6$), except for those curves that have already failed at the inspection time, which samples are given weight $w = 1$. The chronological path pursued to calculate the weights and to obtain the conditional failure probability is represented in Figure 7.3. The total failure event at the time of observation, as shown in Figure 7.3, is obtained as

$$F = F_1 \cup ((F_t \cap \overline{F_1}) | \ \overline{R}); \tag{7.3}$$

and, consequently, the total failure probability can be calculated as

$$P[F] = P[F_1] + P\left[F_t \cap \overline{F_1}\right] \; P\left[\overline{R}\right]; \tag{7.4}$$

where, $P[\overline{R}] = 1-w$ is the probability of non-detection/non-repair, and $F_t = [a(t) > a_c]$ is the failure event at the evaluation time.

7.2 Design of maintenance strategies with one and two inspections

The optimization is formulated as in Chapter 6, where the inspection time, $\boldsymbol{t}^{\text{insp}}$, and the inspection quality, q, are the design variables of the problem.

Figure 7.4 shows how the total cost displays on graph as a function of the first inspection time, with fixed inspection quality. Although the cost of failure may appear quite smooth, every point of the curve is obtained by estimating the failure probability, and therefore it is associated with an estimation error. In this example, the achieved estimation error is quite small ($CoV < 10^{-3}$) thus the curves appear quite smooth. The curve of failure cost shows a typical concave shape. The minimum is approximately located at $t^{\text{insp}*} = 20$ years. The minimum total cost is slightly shifted, see Figure 7.4a, as the cost of inspection decreases with the inspection time. The cost of repair is very small, compared to the other costs, as shown in Figure 7.4a. The optimal inspection time moves slightly backward as the quality of inspection increases, as shown in Figure 7.4b, but at the same time the total cost of maintenance decreases. However, there seems to be no particular advantage in increasing the inspection quality beyond a certain level (70 or 80 for the case of Figure 7.4b) on the optimal cost of maintenance.

With two inspections, the total cost is represented on a time grid, where every point corresponds to a pair $(t_i^{\text{insp}}, t_j^{\text{insp}})$. The resulting graph is the surface in Figure 7.5.

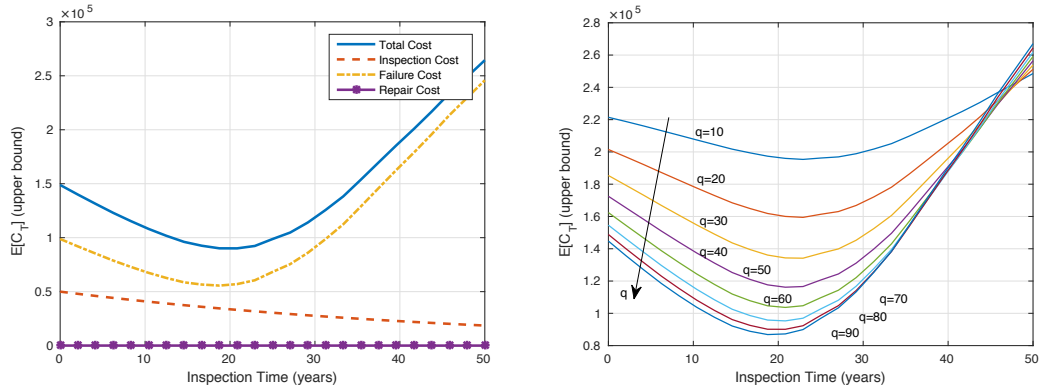

(a) combination of costs for q=70 **(b)** costs for different inspection qualities

Figure 7.4: Curves of costs with one inspection (N=1)

The minimum total cost identifies the pair $\boldsymbol{t}^{\text{insp}*} = (26.5,\ 16.8)$ years, when the two inspections should be performed. From Figure 7.5a it is also possible to note that the curve is symmetric as the time for first and second inspection are interchangeable.

7.3 Optimal inspection schedule without imprecision

In this section a numerical example, taken from literature [37], is solved within a reliability-based optimisation framework without considering imprecision, i.e. defining the uncertainty by means of CDFs only. This is presented to show the efficiency of the developed forced Monte Carlo methodology.

7.3.1 Definition of uncertainties

The input quantities are modelled with continuous probability distributions. The parental distributions are provided in Lukić and Cremona (2001) [37]. The uncertainty model is constructed from the nominal values of mean and standard deviation of Table 7.2. Note that the material quantities m and $\ln C$ show a strong negative Gaussian correlation, which is usually close to -0.99.

7.3.2 Definition of constraint and cost function

It is recalled that the inspection time vector, $\boldsymbol{t}^{insp}$, and the inspection quality, q, are the design variables of the optimisation task. The input unit costs of maintenance and failure are reported in Table 7.3.

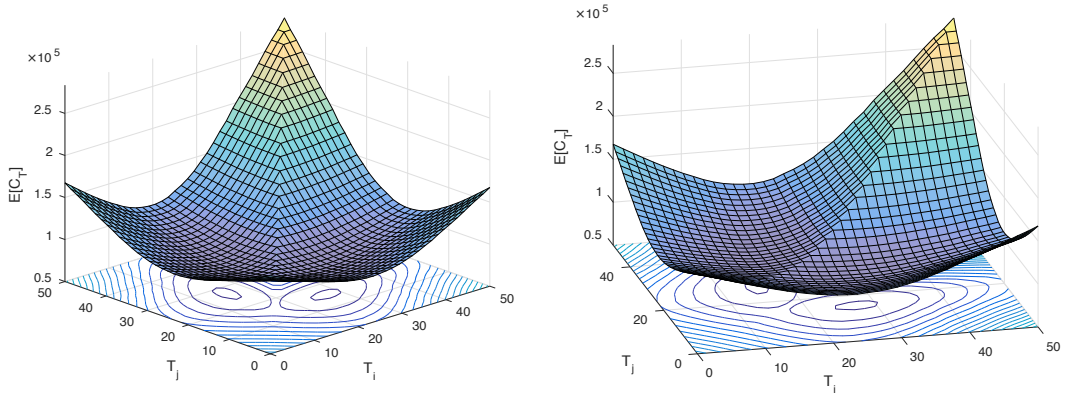

(a) **(b)**

Figure 7.5: Total costs surface with two inspections (N=2)

Table 7.2: Probability distributions for the input quantities of the structural example

Random variable		Mean, S.Deviation and C. of Variation		
θ_i	Distribution	E$[\theta_i]$	Std$[\theta_i]$	CoV$[\theta_i]$
a_0 [mm]	Lognormal	0.125	0.045	36.0
ΔS [MPa]	Gamma	7.800	0.100	1.3
C^* $\left[10^{-13}\text{ mm/cycles}\right]$	Lognormal	2.500	0.923	36.9
m^*	Normal	3.000	0.040	1.3
a_f [mm]	Gumbel	0.500	0.050	10.0
a/c	Lognormal	0.400	0.160	40.0
d [mm]	Gamma	812.0	8.100	10.0
b [mm]	Gamma	31.60	3.200	10.1
h [mm]	Gamma	8.400	0.700	8.3
ϕ [deg]	Gamma	35.00	2.000	5.7

*Correlation: $\tilde{\rho}\,(\ln C,\ m) = -0.99$

Table 7.3: Unit costs used for the structural example

Cost	Value	Description
c_I	10^4	Unit cost of inspection
c_R	10^2	Unit cost of repair
c_F	10^5	Unit cost of failure
s	0.01	Discount rate

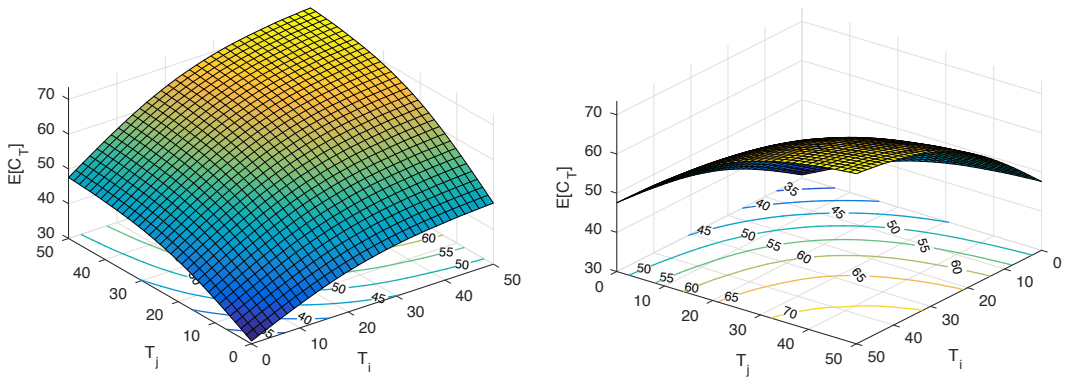

(a) **(b)**

Figure 7.6: Repair cost surface with two inspections (N=2)

Table 7.4: Minimum cost, failure probability and corresponding optimum inspection times

N	p_F	minC_M	q^*	$\boldsymbol{t}^{\text{insp}}$ years
6	10^{-3}	4.4 10^6	87.6	$\{0.7, 7.4, 13.9, 21.1, 31.6, 45.4\}$
7	10^{-3}	4.2 10^6	73.0	$\{0.7, 4.6, 11.4, 17.0, 24.8, 33.9, 49.0\}$
9	10^{-3}	3.9 10^6	51.2	$\{0.5, 4.0, 8.3, 11.4, 16.0, 20.8, 27.0, 32.7, 41.8\}$
11	10^{-3}	4.0 10^6	43.2	$\{0.7, 1.7, 5.5, 10.3, 13.9, 16.8, 20.9, 25.7, 31.6, 38.7, 45.4\}$
15	10^{-3}	4.1 10^6	33.5	$\{0.02, 1.5, 4.5, 7.3, 10.5, 12.3, 15.4, 18.8, 22.4, 24.8, ..., 50\}^*$
19	10^{-3}	4.0 10^6	25.4	$\{0.02, 1.0, 1.9, 4.6, 7.7, 9.3, 11.3, 13.9, 16.3, 18.7, 20.4..., 50\}^{**}$
*	$..., 29.2, 33.9, 41.8, 48.3, 50\}$			
**	$..., 22.9, 25.6, 29.1, 32.2, 37.0, 40.2, 47.8, 50\}$			

7.3.3 Solution to the constrained optimization with N inspections

Genetic Algorithm (GA) is used to find the optimum of the constrained optimization problem. The choice for GA is justified by the stochastic nature of the objective function and constraint, which make them noisy functions. As a consequence, information about the derivatives on both objective and constraint cannot be used. Results from the constrained optimization, as the number of inspections increases, are obtained by fixing a critical threshold of failure probability to $p_F^{\text{critic}} = 10^{-3}$. The variance of the failure probability estimator obtained for this problem is very small and approximately $Var[p_F] \simeq 5 \cdot 10^{-7}$. It is necessary to perform a number of inspections N>5 in order to find a suitable solution, as at least 6 inspections are needed to meet the required reliability constraint. With 5 inspections the failure probability at the optimum is $p_F^* > 10^{-3}$. Note from Table 7.4, that as the number of inspections increases, the minimum total cost does not necessarily have to increase, as the quality of every single inspection may decrease. About the inspection times, despite coming from the solutions of a stochastic optimization, the results are quite evenly distributed, although, it seems to be preferable to run more inspections within the first 10 years. Early inspection times shall be penalised as the chances of detecting a crack at the beginning of time are very small. However, from Table 7.4, when 15 or 19 inspections are performed, the first inspection time gets very close zero. Within this framework an inspection in the vicinity of zero is associated with very small chance of detection, which causes all the weights w to be approximately equal to one. Nonetheless, because of the crack initiation assumption, all the simulated components have to have (at time zero) an initial crack length, which can be of detectable size. When many inspections are performed, such as in the case of 15 or 19 inspections, performing very early and late inspections seems to be beneficial to the overall failure cost. This might suggest that when a large number of inspections is considered, what matters most is the time lag between inspections rather the individual inspection times, as the optimiser tries to find a solution selecting times from the whole available range of time.

Table 7.5: Central values and bounded intervals for the mean and standard deviation of the input p-boxes

P-box		Central values		Relative uncertainty: $e_I = 0.05$	
θ_i	Distribution	$\tilde{\mu}_i$	$\tilde{\sigma}_i$	$\underline{\mu}_i(5\%)$	$\overline{\sigma}_i(5\%)$
$\nu\,[10^6\text{cycles/year}]$	Lognormal	7.5	0.5	[7.125, 7.875]	[0.475, 0.525]
a_0 [mm]	Lognormal	0.125	0.045	[0.119, 0.131]	[0.043, 0.047]
ΔS [MPa]	Gamma	7.800	0.100	[7.410, 8.190]	[0.095, 0.105]
C^* $[10^{-13}$ mm/cycles$]$	Lognormal	2.500	0.923	[2.375, 2.625]	[0.877, 0.969]
m^*	Normal	3.000	0.040	[2.850, 3.150]	[0.038, 0.042]
a_f [mm]	Gumbel	1.000	0.050	[0.950, 1.050]	[0.019, 0.021]
a/c	Lognormal	0.400	0.160	[0.380, 0.420]	[0.152, 0.168]
d [mm]	Gamma	812.0	8.100	[771.4, 852.6]	[7.695, 8.505]
b [mm]	Gamma	31.60	3.200	[30.02, 33.18]	[3.040, 3.360]
h [mm]	Gamma	8.400	0.700	[7.980, 8.820]	[0.665, 0.735]
ϕ [deg]	Gamma	35.00	2.000	[33.25, 36.75]	[1.900, 2.100]

*Correlation: $\tilde{\rho}\,(\ln C,\ m) = -0.99, \quad \underline{\overline{\rho}}\,(\ln C,\ m) = [-0.995,\ -0.935]$

7.4 Optimal inspection schedule considering imprecision

In this section, a reliability-based optimization is performed, where the uncertainty is defined by means of distribution-free p-boxes. The distribution-free p-boxes are obtained introducing imprecision in the distributions of Table 7.2, as shown in the next section.

7.4.1 Definition of uncertainties

The uncertainty model is constructed from the nominal values of mean and standard deviation of Table 7.5, by adding increasing levels of imprecision to the input parameters. The material quantities $\ln(C)$ and m show a strong negative Gaussian correlation, which is usually close to 0.99. However, the correlation coefficient is never a precise number, and here it is assumed to range in the following bounded interval $\underline{\overline{\rho}} = [-0.995, -0.935]$. The relative uncertainty factor $e_I \in [0, 1]$ defines the level of imprecision for the uncertain quantities, so, for instance, the bounded interval of the mean value of quantity i is

$$\underline{\overline{\mu}}_i = [\tilde{\mu}_i\ (1 - e_I),\ \tilde{\mu}_i\ (1 + e_I)]; \tag{7.5}$$

where, $\tilde{\mu}_i$ is the central (nominal) mean value of quantity i. The Table 7.5 shows the bounded intervals for mean and standard deviation corresponding to two different levels of imprecision. With the above uncertainty definition, the analyst can remove the

assumption of using exact values for the probability distribution definition, which is always too strong at a design stage of the analysis. Moreover, by means of uncertainty propagation, it is possible to appreciate the output sensitivity to the amount of uncertainty. This helps recognizing the relative importance of the computational model parameters on the output uncertainty.

7.4.2 Failure probability sensitivity

A self-contained measure of global sensitivity can be extracted from the general uncertainty model by means of pinching. Pinching is a global sensitivity technique that makes use of min-max propagation. A global sensitivity metric is obtained by comparing the response uncertainty when the uncertain parameters are all intervals against the response uncertainty when the uncertain parameters are all intervals except one, which is the selected parameter. The selected parameter is collapsed into a single (crisp) value, which usually is assumed to be the nominal value. Here, pinching is performed replacing the input quantity with a precise distribution function corresponding to the nominal values of Table 7.2. The sensitivity measure is obtained as

$$S_{\theta_i} = \left| 1 - \frac{U(\theta_{\sim i})}{U(\boldsymbol{\theta})} \right|; \tag{7.6}$$

where, $U(\theta_{\sim i})$ is the amount of uncertainty outputted pinching parameter θ_i, and $U(\boldsymbol{\theta})$ is the total amount of uncertainty. The procedure is repeated for every input quantity, pinching the inputs one by one. The amount of uncertainty is computed as

$$U(\theta_{\sim i}) = \ln(\overline{p}_F(\theta_{\sim i})/\underline{p}_F(\theta_{\sim i})). \tag{7.7}$$

The global sensitivity analysis was performed choosing 4 different levels of imprecision to better explore the response of the model to the amount of uncertainty. The analysis led to the results shown in Figure 7.7, where clearly the most important input quantity is the material parameter, m, followed by the stress range ΔS, the annual number of cycles, ν, and the material parameter, C.

7.4.3 Definition of constraint and cost function

The input unit costs used here are reported in Table 7.3. When imprecision is considered there is an infinite number of cost function, ranging between a lower and upper bound. In this example the cost objective function is identified in the total cost upper bound. Upper and lower bounds of the total cost, obtained with 1% of imprecision in the input parameters, are displayed in Figure 7.8a, as a function of the first inspection time with fixed inspection quality. For the cost upper bound the minimum (cost) is located at approximately 30 years, while for the lower bound the minimum (cost) is at

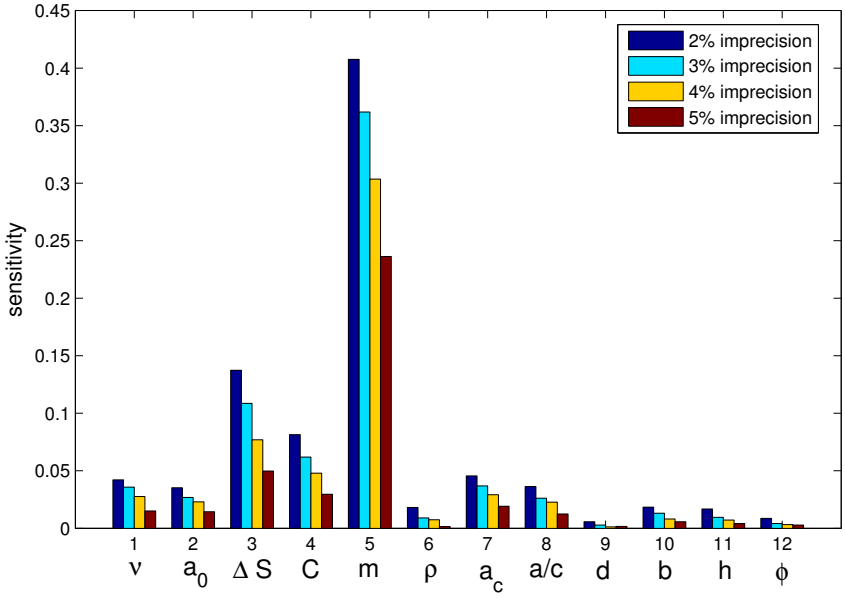

Figure 7.7: Global sensitivity on the failure probability is obtained pinching one input at a time

approximately 39 years. Equivalently, the failure probability has two different minima, one for the upper and one for the lower bound, as shown in Figure 7.8b.

7.4.4 Time variant failure probability

The failure probability increases with time as the damage accumulates. The effect of performing a different number of inspections is shown in Figure 7.9. The blue solid line shows the failure probability curve when no inspections are performed. The green line with square dots shows the same curve when 3 inspections are performed at year 5, 10

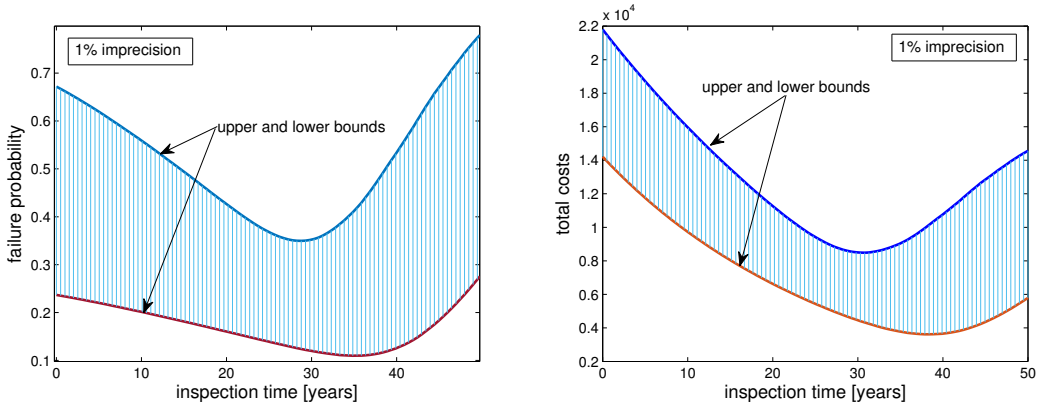

(a) Total costs **(b)** Failure probability

Figure 7.8: Upper and lower bounds define the set of possible states and candidate solutions

and 16. Equivalently the remaining two lines show the failure probability curve when 6 and 7 inspections are performed. From the graphs of Figure 7.9 it can be appreciated that, after inspection, the reliability changes the slope but does not produce a discontinuous jump to a different value. These results are coherent with the assumptions of preventive maintenance formulated in the previous Chapter. From Figure 7.9b, the magnitude of failure probability reduction with 7 inspections can be better appreciated.

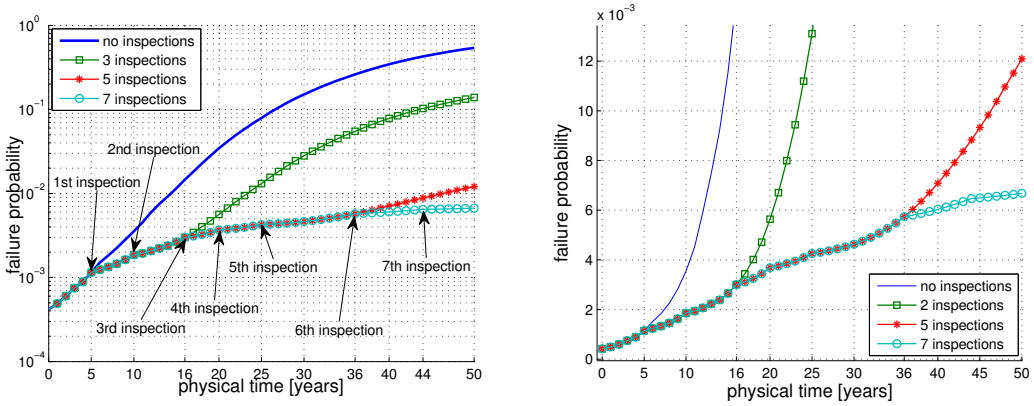

(a) y-axis on logarithmic scale **(b)** y-axis on normal scale

Figure 7.9: Failure probability curves obtained performing 0, 2, 5 and 7 inspections with fixed quality

7.4.5 Optimal inspection schedule

The optimisation problem considering imprecision is solved targeting the upper bound of the total cost only. The failure probability threshold is set to $p_F^{\text{critic}} = 10^{-3}$. Table 7.6 shows that there is no sensible decrease in the total cost of maintenance, as the number of inspections increases. However, the optimum quality decreases, which means that, at the same total cost, less expensive inspection techniques can be used. Performing 4 or less inspections in this case is not enough to meet the safety constraint requirement, as the failure probability cannot be decreased below the threshold of 10^{-3}, even for large inspection qualities. Early inspections are penalised by this framework, as the chances of detecting cracks are very small at the beginning of time. Nonetheless, when 15 inspections are performed the first inspection time gets very close to zero. Such an early inspection is associated with small chance of detection, which causes all the weights w to be approximately equal to one. When all the weights are equal to one, the conditional failure probability at the observation time coincides with the failure probability with no inspections, therefore, performing an inspection at time zero is approximately equivalent to not performing any inspection at all. However, because of the crack initiation assumption, all the simulated components have to have (at time zero) an initial crack length (see Figure 7.2), which can be of detectable size. On the other end, performing a late inspection causes all the weights to be approximately zero,

Table 7.6: Minimum total costs and corresponding candidate optimum as the number of inspections increases for the case $p_F^{\text{thres}=10^{-3}}$

N	$\hat{p}_F$	min C_M	q^*	$\boldsymbol{t}^{\text{insp}*}$ [years]
5	10^{-3}	3.86 10^6	88.6	$\{7, 14, 20, 30, 34\}$
7	10^{-3}	3.74 10^6	62.0	$\{4.5, 9, 14, 20, 27, 35, 42\}$
9	10^{-3}	3.68 10^6	47.5	$\{2, 7, 11, 14, 19, 24, 29, 36, 39\}$
12	10^{-3}	3.82 10^6	37.9	$\{1.5, 4.5, 9, 11, 18, 22, 26, 32, 37, 45, 50\}$
15	10^{-3}	3.82 10^6	30.3	$\{0.5, 4, 7, 9, 11, 14, 16, 19, 23, 25, 29, 34, 39, 46, 50\}$

* Candidate optima

except for those simulated scenarios that are already beyond the failure threshold that have weights equal to one. Therefore, if the inspection is performed very late most of the simulated components will have already failed, which causes the majority of the weights to be equal to one, and again the conditional failure probability at the observation time will coincide with the failure probability with no inspections. The cost of failure is maximum either at time zero or a the observation time and similarly the optimum is not expected to be located at the time edges. However, when many inspections are performed, such as in the case of 15 inspections, performing very early and late inspections seems to be beneficial to the overall failure cost. A possible explanation for this behaviour is that when a large number of inspections is performed it seems that the time lag between inspections count more than the individual inspection time.

7.5 Chapter summary

This chapter presents an application of the methodology developed in Chapter 6. The application focuses on the optimization of inspection schedules for preventive maintenance of a fatigue-prone component deploying multiple inspections. With this chapter, the efficiency and generality of the developed advanced Monte Carlo simulation method have been illustrated by means of a numerical example. It has been shown not only that the approach can be applied to problems involving a high number of parameters, but it can also be generalised to account for imprecision. The inclusion of imprecision is possible to the price of only one additional reliability analysis, and has allowed the identification of the most important input parameter with respect to the failure probability, as well as the identification of the sensitivity of the optimal schedules to imprecision.

The results presented in this chapter have been peer-reviewed and published on the proceedings of two conferences (see conference papers 1 and 2 from the List of Publications). The papers have been presented at the 23rd Conference on Structural Mechanics in Reactor Technology (SMIRT23), in August 2015, and at The European Safety and Reliability Conference (ESREL), in September 2015.

Chapter 8

The NASA Langley Multidisciplinary UQ Challenge

8.1 Introduction

The need to determine limitations and range of applicability of existing methodologies and of the state of practice in Uncertainty Quantification problems, has led to the development of a challenge, see Ref. [20]. The NASA challenge is divided into 5 different subproblems: subproblem A, for the uncertainty characterisation and reduction of epistemic uncertainty based on data collection; subproblem B, for the sensitivity analysis of the system function; subproblem C and D, for the uncertainty propagation and the extreme case analysis; and subproblem E, for the robust design. In this chapter, for brevity and coherence with previous chapters, results from subproblem B and E are intentionally not presented. The reader is referred to Ref. [49, 50] for a full description of the NASA UQ challenge solution.

A mathematical model that describes the dynamics of a remotely operated twin-jet aircraft developed by the NASA Langley Research Center is analysed (see Figure 8.1). The model, provided as a "Black Box", contains 21 parameters, $\boldsymbol{p}$, 16 design variables, $\boldsymbol{d}$ and 8 outputs, $\boldsymbol{g}$. Furthermore, a set of intermediate variables, $\boldsymbol{x}$, that can be interpreted as outputs of the so-called fixed discipline analysis, $\boldsymbol{x} = h(\boldsymbol{p})$, are the inputs of the cross discipline analysis $\boldsymbol{g} = f(\boldsymbol{x}, \boldsymbol{d})$. One of the main objectives of the proposed problem is to identify the design parameters, $\boldsymbol{d}$, that provide optimal worst case probabilistic performance in presence of the model parameters uncertainty, $\boldsymbol{p}$, with the ultimate goal of performing robust design.

In the following developments, the term "original model" will be used to describe the uncertainty model as provided in the challenge problem; while "reduced model" will refer to the model with reduced uncertainty after the solution of the subproblem A, while "improved model" will refer to the reduced model having four parameters, with the smallest ranges of uncertainty obtained from NASA. Only the main findings are

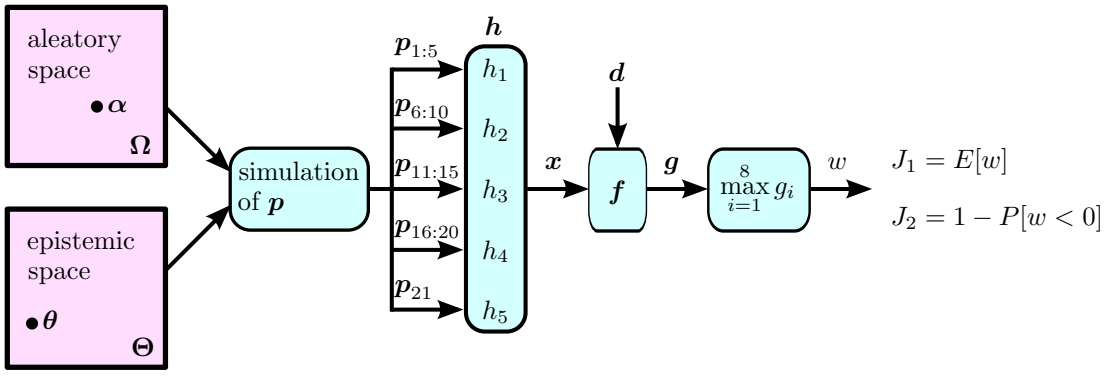

Figure 8.1: Relationship between the variables and functions of the NASA Langley multidisciplinary uncertainty quantification challenge problem [45].

reported, and the reader is referred to Ref. [49] for detailed results of the challenge problem.

Decomposition of variables p into its aleatory and epistemic components Table 8.1 lists all variables of vector $\boldsymbol{p}$ decomposed into an aleatory component and an epistemic component. Note that on the one hand, the aleatory component of a random variable or distributional p-box can be represented as a uniform random variable in $(0, 1]$; on the other hand, the epistemic component of a distributional p-box is given by the intervals that describe the parameters of the parental CDF; in this way, the aleatory $\boldsymbol{\Omega}$ and the epistemic $\boldsymbol{\Theta}$ spaces have respectively 17 and 31 dimensions.

Representation of variable p_1 The input variable p_1 is represented as a unimodal beta distribution whose mean μ and variance σ^2 are uncertain, but are known to lie in the intervals $[3/5,\ 4/5]$ and $[1/50,\ 1/25]$ respectively. Instead beta distributions are characterised by shape parameters a and b which are related to μ and σ^2 by:

$$\mu = \frac{a}{a+b} \qquad\qquad \sigma^2 = \frac{ab}{(a+b+1)(a+b)^2} \tag{8.1}$$

that is,

$$a = -\frac{\mu(\sigma^2 + \mu^2 - \mu)}{\sigma^2} \qquad\qquad b = \frac{(\mu-1)(\sigma^2 + \mu^2 - \mu)}{\sigma^2} \tag{8.2}$$

The required unimodality implies that a and b are greater than 1. For shape parameters lower than 1, the beta distribution assume the U-shaped bimodal distributions.

Representation of variables p_4 and p_5 The copula that relates variables p_4 and p_5 has an interval parameter, namely I_8, which models the correlation $\rho(p_4, p_5)$. Variables p_4 and p_5 are modelled using the following formulation, which permits to split uncer-

Table 8.1: Aleatory and epistemic components of the input variables p_i.

Var.	**Cat.**	**Aleatory component**	**Epistemic component**	**Descr.**
p_1	III	$\alpha_1 \sim \text{Unif}(0,1]$	$I_1 = [3/5,\ 4/5]$	Interval of $\text{E}[p_1]$
		(distribution type:	$I_2 = [1/50,\ 1/25]$	Interval of $\text{Var}[p_1]$
		unimodal Beta)		
p_2	II		$I_3 = [0,\ 1]$	Interval
p_3	I	$\alpha_2 \sim \text{Unif}(0,1]$		Random variable
p_4, p_5	III	$\alpha_3 \sim \text{Unif}(0,1]$	$I_4 = [-5,\ 5]$	Interval of $\text{E}[p_4]$
		$\alpha_4 \sim \text{Unif}(0,1]$	$I_5 = [1/400,\ 4]$	Interval of $\text{Var}[p_4]$
		(distribution type:	$I_6 = [-5,\ 5]$	Interval of $\text{E}[p_5]$
		multivariate Gaussian)	$I_7 = [1/400,\ 4]$	Interval of $\text{Var}[p_4]$
			$I_8 = [-1,\ 1]$	Interval of $\rho(p_4, p_5)$
p_6	II		$I_9 = [0,\ 1]$	Interval
p_7	III	$\alpha_5 \sim \text{Unif}(0,1]$	$I_{10} = [0.982,\ 3.537]$	Interval of a
		(distribution type: Beta)	$I_{11} = [0.619,\ 1.080]$	Interval of b
p_8	III	$\alpha_6 \sim \text{Unif}(0,1]$	$I_{12} = [7.450,\ 14.093]$	Interval of a
		(distribution type: Beta)	$I_{13} = [4.285,\ 7.864]$	Interval of b
p_9	I	$\alpha_7 \sim \text{Unif}(0,1]$		Random variable
p_{10}	III	$\alpha_8 \sim \text{Unif}(0,1]$	$I_{14} = [1.520,\ 4.513]$	Interval of a
		(distribution type: Beta)	$I_{15} = [1.536,\ 4.750]$	Interval of b
p_{11}	I	$\alpha_9 \sim \text{Unif}(0,1]$		Random variable
p_{12}	II		$I_{16} = [0,\ 1]$	Interval
p_{13}	III	$\alpha_{10} \sim \text{Unif}(0,1]$	$I_{17} = [0.412,\ 0.737]$	Interval of a
		(distribution type: Beta)	$I_{18} = [1.000,\ 2.068]$	Interval of b
p_{14}	III	$\alpha_{11} \sim \text{Unif}(0,1]$	$I_{19} = [0.931,\ 2.169]$	Interval of a
		(distribution type: Beta)	$I_{20} = [1.000,\ 2.407]$	Interval of b
p_{15}	III	$\alpha_{12} \sim \text{Unif}(0,1]$	$I_{21} = [5.435,\ 7.095]$	Interval of a
		(distribution type: Beta)	$I_{22} = [5.287,\ 6.945]$	Interval of b
p_{16}	II		$I_{23} = [0,\ 1]$	Interval
p_{17}	III	$\alpha_{13} \sim \text{Unif}(0,1]$	$I_{24} = [1.060,\ 1.662]$	Interval of a
		(distribution type: Beta)	$I_{25} = [1.000,\ 1.488]$	Interval of b
p_{18}	III	$\alpha_{14} \sim \text{Unif}(0,1]$	$I_{26} = [1.000,\ 4.266]$	Interval of a
		(distribution type: Beta)	$I_{27} = [0.553,\ 1.000]$	Interval of b
p_{19}	I	$\alpha_{15} \sim \text{Unif}(0,1]$		Random variable
p_{20}	III	$\alpha_{16} \sim \text{Unif}(0,1]$	$I_{28} = [7.530,\ 13.492]$	Interval of a
		(distribution type: Beta)	$I_{29} = [4.711,\ 8.148]$	Interval of b
p_{21}	III	$\alpha_{17} \sim \text{Unif}(0,1]$	$I_{30} = [0.421,\ 1.000]$	Interval of a
		(distribution type: Beta)	$I_{31} = [7.772,\ 29.621]$	Interval of b

tainty into the aleatory and the epistemic spaces while representing the dependence with an independent copula that does not have any epistemic component:

- The aleatory part of the joint probability box is given by α_3 and α_4 which are independent and uniform random variables on $(0, 1]$. Note that $z_3 = \Phi^{-1}(\alpha_3)$ and $z_4 = \Phi^{-1}(\alpha_4)$ where Φ represents the standard normal CDF.

- The epistemic part of the joint distribution is given by the 5-dimensional box $\times_{i=4}^{8} I_i$.

A simulation from variables p_4 and p_5 can be performed by using the vector $\boldsymbol{z} = [z_3,\ z_4]^T$ and a parameter vector $\boldsymbol{\theta} \in \times_{i=4}^{8} I_i$; the simulation uses the standard procedure for sampling from a multivariate normal PDF. This method employs the Cholesky decomposition of the covariance matrix.

Consequently, the joint distribution-free probability box formed by variables p_4 and p_5 can be represented as the random set $\Gamma : (0, 1]^2 \to \mathcal{F}, \boldsymbol{\alpha} \mapsto \Gamma(\boldsymbol{\alpha})$ where $\boldsymbol{\alpha} = (\alpha_3, \alpha_4)$, $\mathcal{F}$ is the system of focal elements given by the preimages of $\{\alpha_3 \times \alpha_4 \times I_4 \times I_5 \times \cdots \times I_8 : (\alpha_3,\ \alpha_4) \in (0, 1]^2\}$ through $F_{p_4 p_5}$. Since α_3 and α_4 are independent uniform random variables in $(0, 1]$, they can be considered as the realisation of a bidimensional product copula, defined on $(0, 1]^2$. For the interpretation of α_3, α_4, I_4, ..., I_8 the reader is referred to Table 8.1.

8.2 Proposed approach for uncertainty management and quantification

8.2.1 Model updating

The aim of model updating is to reduce the epistemic uncertainty on the output of the model $x = \mathcal{H}(\boldsymbol{\alpha}; \boldsymbol{\theta})$ based on the availability of a limited set of data (observations) $\mathcal{D}_e := \{x_k^e : k = 1, 2, \ldots, n_e\}$. These observations of the "true uncertainty model" $\boldsymbol{\theta}^* \in \boldsymbol{\Theta}$, i.e. that ideal model that generates the observation, can be used to improve the uncertainty model, i.e. to reduce the original intervals of the epistemic uncertainties by excluding those combinations of parameters that fail to describe the observations. Two different approaches will be used for model updating: a non-parametric method based on goodness-of-fit tests and a Bayesian method. In this chapter, hats ($\hat{F}$) and tildes ($\tilde{F}$) will be used for referring to the empirical CDFs and the kernel density estimations of CDFs, respectively.

8.2.1.1 Non-parametric statistic method based on Kolmogorov-Smirnov test

A simple and fast approach to improve the uncertainty model is based on the comparison of the CDFs of the observations of the true uncertainty model and those obtained by means of random combinations of the input parameters, in order to identify tighter intervals which form a reduced epistemic space and which are in agreement with the observations.

Let us consider the epistemic space $\boldsymbol{\Theta}$ of the involved variables. Random realisations $\boldsymbol{\theta}_i$ in the epistemic space $\boldsymbol{\Theta}$ are generated assuming, for example, a uniform PDF on $\boldsymbol{\Theta}$ (in agreement with the Laplace's principle of indifference). Thereafter the points $\{\boldsymbol{\alpha}_j, j = 1, 2, \ldots, n\}$ are sampled from the aleatory space $\boldsymbol{\Omega}$ according to the copula C (Nelsen [46] provides methods to do it), in order to simulate n observations from the system $\mathcal{H}$ as $x_j^i = \mathcal{H}(\boldsymbol{\alpha}_j, \boldsymbol{\theta}_i)$. For a single realisation $\boldsymbol{\theta}_i$, the Kolmogorov-Smirnov statistic, which is defined as

$$D_i = \sup_x |\hat{F}(x|\boldsymbol{\theta}_i) - \hat{F}_e(x)|, \tag{8.3}$$

is used to measure the similarity between the CDFs obtained with the sampled set $\{x_j^i,\ j = 1, 2, \ldots, n\}$ and the set of observations $\mathcal{D}_e$. Here $\hat{F}(\cdot|\boldsymbol{\theta}_i)$ and $\hat{F}_e$ are the empirical CDFs obtained using the random samples drawn according to the epistemic parameters $\boldsymbol{\theta}_i$ and the provided experimental data, respectively.

The Kolmogorov-Smirnov test is used to obtain confidence limits on $\hat{F}(\cdot|\boldsymbol{\theta}_i)$ by choosing different critical values of the test statistic D. This implies that a band of width $\pm D$ around $\hat{F}_e(x)$ will entirely contain $\hat{F}(\cdot|\boldsymbol{\theta}_i)$ with probability $1 - c$. This enables the identification of those combinations of epistemic parameters, such that $P(D_i > D) = c$. $c = 0$ means that all the CDFs $\hat{F}(\cdot|\boldsymbol{\theta}_i)$ are accepted and the refinement of the input intervals is not possible, whereas $c = 1$ is a limit case that implies that $\hat{F}(\cdot|\boldsymbol{\theta}_i)$ comes from the same model that has generated the target distribution $\tilde{F}_e(x)$, i.e. no epistemic uncertainty is present.

The selection of D is a critical task and generally depends on the amount of available information (i.e. number of observations). A practical approach is to use two different data sets that come from the same process to estimate the critical level of the measure of similarity $D_{\hat{v}}$, using Eq. (8.3). The computed validation distance $D_{\hat{v}}$ can be used to set the required confidence level, accepting all the combinations of epistemic parameters with $D_i < D_{\hat{v}}$. When an independent validation data set is not available, a cross validation data set can be constructed to test the model in order to limit problems such as over-fitting. This cross validation data set can be obtained by means of re-sampling techniques [10]. Cross-validation is important to protect against hypotheses suggested by the data [44] specially where further samples are costly or simply impossible to

collect.

The non-parametric approach based on the Kolmogorov-Smirnov test is a fast method for performing uncertainty characterisation (and model updating). However, it is important to keep in mind the limitations of the approach. In fact, the method assumes that the measure of similarity D_i is distributed according to the Kolmogorov distribution [35], which is strictly true only for large sample sets. It is possible to use some smoothing techniques such as the Gaussian kernel density estimation to overcome this limitation. Gaussian kernel density estimates for the CDF of $\mathcal{D}_e$ are given by

$$\tilde{F}_e(x) = \frac{1}{n_e \sigma \sqrt{2\pi}} \int_{-\infty}^{x} \sum_{j=1}^{n_e} \exp\left(-\frac{1}{2} \left(\frac{x' - x_j^e}{\sigma} \right)^2 \right) \mathrm{d}x'; \tag{8.4}$$

here σ stands for the standard deviation of the Gaussian kernels that represents the smoothing parameter, proportional to the so-called bandwidth, while n_e is the number of experimental data. Assuming that x is a continuous random variable, for $n_e \to \infty$ the Gaussian kernel density estimate converges to the true underlying density. The support of the associated PDFs $\tilde{f}_e(x)$ (i.e. $\{x : \tilde{f}_e(x) > 0\}$) and the bandwidth of the kernel have strong influence on the resulting estimate. We suggest to use the approach in Ref. [57] to estimate the support of the PDF and Silverman's rule of thumb [66] to estimate the bandwidth of the kernels. Using realisations from Eq. (8.4), the measure of similarity can be calculated via Eq. (8.3) where $\hat{F}_e(x)$ is replaced by $\tilde{F}_e(x)$. Please note that the Gaussian kernels can be used to define a new critical measure level indicated with $D_{\tilde{v}}$.

To summarise, the following pseudo-algorithm is used:

1. Estimate the parameters σ and the Gaussian kernel CDF $\tilde{F}_e$ using Eq. (8.4);
2. Estimate $D_{\hat{v}}$ and $D_{\tilde{v}}$;
3. Generate realisations in the epistemic space, $\boldsymbol{\theta}_i$;
4. Draw n points from the aleatory space $\boldsymbol{\Omega}$, using copula C; we will call these samples $\{\boldsymbol{\alpha}_j : j = 1, \ldots, n\}$;
5. Evaluate the model $x_j^i := \mathcal{H}(\boldsymbol{\alpha}_j; \boldsymbol{\theta}_i)$ for $j = 1, \ldots, n$;
6. Estimate the empirical CDF $\hat{F}(\cdot|\boldsymbol{\theta}_i)$ of the set of samples $\{x_j^i, j = 1, 2, \ldots, n\}$;
7. Using Eq. (8.3), compute the measure of similarity D_i;
8. If $D_i < D_{\tilde{v}}$ (or $D_i < D_{\hat{v}}$) collect $\boldsymbol{\theta}_i$. The set of collected points identifies a reduced space in the original epistemic space.

8.2.1.2 Bayesian updating in the epistemic space

Bayesian inference is a statistical method in which the Bayes' rule is used to update the probability estimate for a hypothesis, as additional information is available.

Suppose we are given a set of observed data points $\mathcal{D}_e := \{x_k^e : k = 1, 2, \ldots, n_e\}$ called the *evidence*, and which are sampled from a PDF $p(\cdot; \boldsymbol{\theta}^*)$ which belongs to a certain family of PDFs $\{p(\cdot; \boldsymbol{\theta}) : \boldsymbol{\theta} \in \boldsymbol{\Theta}\}$ called the *parametric model*. The idea of Bayesian inference is to update our belief about the vector of parameters $\boldsymbol{\theta}$ provided that $\boldsymbol{\theta}^*$, the true set of parameters of the PDF, is unknown. Bayes' theorem updates that belief using two antecedents:

- a *prior* PDF $p(\boldsymbol{\theta})$, which indicates all available knowledge about $\boldsymbol{\theta}^*$ before the evidence $\mathcal{D}_e$ is observed;

- and the *likelihood function* $P(\mathcal{D}_e|\boldsymbol{\theta})$, which is a function related to the probability of observing the samples $\mathcal{D}_e$ assuming that the true parameter underlying the model PDF $p(x; \boldsymbol{\theta})$ is $\boldsymbol{\theta}$; it is defined as

$$P(\mathcal{D}_e|\boldsymbol{\theta}) = \prod_{k=1}^{n_e} p(x_k^e; \boldsymbol{\theta}), \tag{8.5}$$

  when a set of independent and identically distributed observations $\mathcal{D}_e$ is available.

The updated belief about the vector of parameters $\boldsymbol{\theta}$ after observing the evidence $\mathcal{D}_e$, is modelled by the so-called *posterior* PDF $p(\boldsymbol{\theta}|\mathcal{D}_e)$ which is calculated by:

$$p(\boldsymbol{\theta}|\mathcal{D}_e) = \frac{P(\mathcal{D}_e|\boldsymbol{\theta})p(\boldsymbol{\theta})}{P(\mathcal{D}_e)}; \tag{8.6}$$

where the probability of the evidence,

$$P(\mathcal{D}_e) = \int_{\boldsymbol{\Theta}} P(\mathcal{D}_e|\boldsymbol{\theta})p(\boldsymbol{\theta})\mathrm{d}\boldsymbol{\theta} \tag{8.7}$$

can be understood as a normalising constant. Bayesian updating hopes that after using the evidence $\mathcal{D}_e$ the posterior PDF $p(\boldsymbol{\theta}|\mathcal{D}_e)$ is sharply peaked about the true value of $\boldsymbol{\theta}^*$. We will update our belief about the true set of parameters $\boldsymbol{\theta}^* \in \boldsymbol{\Theta}$ propagating the evidence through the Bayes' equation numerically. Samples of the posterior PDF can be generated without the necessity to evaluate $p(\boldsymbol{\theta}|\mathcal{D}_e)$, using an algorithm called Transitional Markov Chain Monte Carlo (TMCMC) [17].

As prior PDF, we will use a uniform distribution on the epistemic space $\boldsymbol{\Theta}$, that is $\boldsymbol{\theta} \sim \mathrm{Unif}(\boldsymbol{\Theta})$, in accordance to the Laplace's principle of indifference (or principle of maximum entropy).

Different likelihood functions can be used, based on different mathematical assumptions. In the following, two methods will be proposed: a Bayesian method that uses a kernel density estimator to represent the posterior, $p(\cdot|\boldsymbol{\theta}_i)$, and an approximate Bayesian computational method.

Bayesian computational method In this case, the likelihood is estimated using a kernel density function. Assuming that the samples $\mathcal{D}_e$ are drawn from $p(x;\boldsymbol{\theta}_i)$, the likelihood $P(\mathcal{D}_e|\boldsymbol{\theta}_i)$ is defined in the following way:

1. Draw n points, $\{\boldsymbol{\alpha}_j : j = 1,\dots,n\}$, from the aleatory space $\boldsymbol{\Omega}$, using copula C;
2. Calculate $x_j^i := \mathcal{H}(\boldsymbol{\alpha}_j;\boldsymbol{\theta}_i)$ for $j = 1,\dots,n$;
3. Using kernel density estimation and the samples $\{x_j^i : j = 1,\dots,n\}$, estimate the CDF $\tilde{F}(\cdot|\boldsymbol{\theta}_i)$ and its associated PDF $\tilde{p}(x|\boldsymbol{\theta}_i) \equiv p(x;\boldsymbol{\theta}_i)$. This step is required because $\tilde{p}(x|\boldsymbol{\theta}_i)$ cannot be obtained analytically;
4. Calculate the likelihood function $P(\mathcal{D}_e|\boldsymbol{\theta}_i)$ as in Eq. (8.5).

Approximate Bayesian computational method The likelihood calculated by means of the "Bayesian computational method" applies Bayes' theorem directly and without strong assumptions. However it requires a large number of model evaluations and a relatively large data set to converge [49]. Recently, approximate Bayesian computational methods have been proposed to reduce the computational costs of the expensive or intractable likelihood function [11, 16]. The likelihood can be for instance approximated with the following expression:

$$P(\mathcal{D}_e|\boldsymbol{\theta}_i) = \prod_{k=1}^{n_e} \frac{1}{\sqrt{2\pi}\sigma} \exp\left(-\frac{1}{2}\left(\frac{\delta_k}{\sigma}\right)^2\right) \tag{8.8}$$

where δ_k is the absolute value of the difference between the empirical CDF $\hat{F}(\cdot|\boldsymbol{\theta}_i)$ obtained for an individual realisation $\boldsymbol{\theta}_i$ of the epistemic space $\boldsymbol{\Theta}$, evaluated at each point $\{x_k^e, k = 1,2,\dots,n_e\}$ and the empirical CDFs of the experimental dataset $\mathcal{D}_e$, that is:

$$\delta_k = \left|\hat{F}(x_k|\boldsymbol{\theta}_i) - \hat{F}_e(x_k^e)\right| \tag{8.9}$$

for $k = 1,2,\dots,n_e$. Please note that the Bayesian updating approach is generally applied to identify a fixed estimate of $\boldsymbol{\theta}$ as close as possible to $\boldsymbol{\theta}^*$. Here, the approach has been used to identify a reduced epistemic space containing the sought values of the unknown parameters. If a constant σ is used, the Bayesian updating formulation, here introduced, is equivalent to a minimisation in the least square sense of the distance between the CDFs $\hat{F}(\cdot|\boldsymbol{\theta}_i)$ and $\hat{F}_e$. However the value of σ is unknown, and hence it represents an additional parameter that needs to be estimated [12].

This last approach is indeed based more on practical considerations than on a sound mathematical basis, and is open to criticisms, since the differences δ_k are assumed to be independent and normally distributed with zero mean and unit variance; and that even though δ_k is normally distributed, it will only take values in the interval $[0,1]$ since the CDF ranges between 0 and 1.

Using the above defined prior PDF and likelihood functions, the TMCMC algorithm [17] is employed in order to find samples of the posterior $p(\boldsymbol{\theta}|\mathcal{D}_e)$. The likelihood $P(\mathcal{D}_e|\boldsymbol{\theta}_i)$ is calculated, using the approximate Bayesian computational method, by the following procedure:

1. Draw n points ($\{\boldsymbol{\alpha}_j : j = 1, \ldots, n\}$) from the aleatory space $\boldsymbol{\Omega}$, using copula C;
2. Calculate $x_j^i := \mathcal{H}(\boldsymbol{\alpha}_j; \boldsymbol{\theta}_i)$ for $j = 1, \ldots, n$;
3. Using the samples $\{x_j^i : j = 1, \ldots, n\}$, estimate the empirical CDF $\hat{F}(\cdot|\boldsymbol{\theta}_i)$;
4. Compute $\delta_k = \left|\hat{F}(x_k^e|\boldsymbol{\theta}_i) - \hat{F}_e(x_k^e)\right|$ at each point $x_k^e \in \mathcal{D}_e$;
5. Calculate the likelihood function $P(\mathcal{D}_e|\boldsymbol{\theta}_i)$ as in Eq. (8.8).

8.2.2 Uncertainty Propagation

The focus of the uncertainty propagation analysis is to quantify the effect of the uncertain model parameters on quantities of interest, such as the mean, variance and quantiles of the system's response or its failure probability. The generalized probabilistic model makes the UQ a rather challenging task in terms of computational cost. The challenge is to compute the lower and upper bounds of the quantities of interest. Monte Carlo method remains the most versatile and simple tool to propagate epistemic and aleatory uncertainty.

8.2.2.1 Optimisation in the epistemic space (Double Loop approach)

In this approach, the quantity of interest (e.g. mean or failure probability estimation) defines the objective function; and the bounds on that objective function are calculated by means of a global search in the epistemic space $\boldsymbol{\Theta}$. On one hand, the lower and upper bounds of the mean are obtained as:

$$\underline{\mu} = \min_{\boldsymbol{\theta}\in\boldsymbol{\Theta}} \mu(\boldsymbol{\theta}) \qquad\qquad \overline{\mu} = \max_{\boldsymbol{\theta}\in\boldsymbol{\Theta}} \mu(\boldsymbol{\theta}) \tag{8.10}$$

where the mean of the response model is given by:

$$\mu(\boldsymbol{\theta}) = \int_{\boldsymbol{\Omega}} \mathcal{H}(\boldsymbol{\alpha}; \boldsymbol{\theta}) \mathrm{d}C(\boldsymbol{\alpha}). \tag{8.11}$$

On the other hand, the lower and upper bound of the failure probability, defined as the excedance of a critical threshold level $\mathcal{H}^{crit}$ of the model response, are obtained as

$$\underline{P_f} = \min_{\boldsymbol{\theta}\in\boldsymbol{\Theta}} P_f(\boldsymbol{\theta}) \qquad\qquad \overline{P_f} = \max_{\boldsymbol{\theta}\in\boldsymbol{\Theta}} P_f(\boldsymbol{\theta}); \tag{8.12}$$

here $P_f(\boldsymbol{\theta})$ stands for the failure probability, that is,

$$P_f(\boldsymbol{\theta}) := \int_{\boldsymbol{\Omega}} \mathcal{I}[\mathcal{H}(\boldsymbol{\alpha};\boldsymbol{\theta}) > \mathcal{H}^{crit}]\mathrm{d}C(\boldsymbol{\alpha}); \tag{8.13}$$

where, $\mathcal{I}$ is the indicator function. The Double Loop approach is used to calculate the bounds Eq. (8.10) and Eq. (8.12), by means of Monte Carlo simulation as:

- The outer loop drives an optimisation/search process in the epistemic space $\boldsymbol{\Theta}$ to identify the lower and upper bounds Eq. (8.10) and Eq. (8.12). This search is performed either by Monte Carlo sampling, taking into account that this optimisation method is very inefficient when many epistemic parameters are involved, or by means of optimisation methods such as Genetic Algorithms, as shown in Sections 8.4 and 8.5.

- The inner loop propagates the aleatory uncertainty and estimates the statistical quantities of interest (e.g. expected value, failure of probability, CDF, etc). In this way, several $\boldsymbol{\alpha}_j$ are sampled from copula C in order to estimate integrals of Eq. (8.11) and Eq. (8.13). It should be taken into account that this Monte Carlo integration in the aleatory space $\boldsymbol{\Omega}$ is insensitive to the dimensionality of the problem, although it can be inefficient when the integral of Eq. (8.13) is computed, as the probability of failure can be very small. The estimation of the integrals can be sped up by adopting the so called Advanced Monte Carlo methods, such as Importance Sampling, Subset Simulation and Line Sampling [21], as it has been shown in the previous chapters.

8.2.2.2 Propagation of focal sets (Random Set approach)

The second approach for uncertainty propagation, which is described in Refs. [3–5] and in Chapter **??**, is based on the propagation of focal sets through a function. The aleatory space $\boldsymbol{\Omega}$ contains the regions $F_{LP} := \{\boldsymbol{\alpha} \in \boldsymbol{\Omega} : \Gamma(\boldsymbol{\alpha}) \subseteq F, \Gamma(\boldsymbol{\alpha}) \neq \varnothing\}$ and $F_{UP} := \{\boldsymbol{\alpha} \in \boldsymbol{\Omega} : \Gamma(\boldsymbol{\alpha}) \cap F \neq \varnothing\}$ which are correspondingly formed by all those points whose respective focal elements are completely contained in the failure set $F = \{\boldsymbol{x} \in \mathcal{X} : g(\boldsymbol{x}) > \mathcal{H}^{crit}\}$ or have in common at least one point with F respectively. Note that the set F is defined in the space of input variables $\mathcal{X}$; in this case, the lower and upper probability measures of F can be calculated by:

$$\underline{\underline{P_f}} = \int_{\boldsymbol{\Omega}} \mathcal{I}\left[\boldsymbol{\alpha} \in F_{LP}\right] \mathrm{d}C(\boldsymbol{\alpha}), \quad \overline{\overline{P_f}} = \int_{\boldsymbol{\Omega}} \mathcal{I}\left[\boldsymbol{\alpha} \in F_{UP}\right] \mathrm{d}C(\boldsymbol{\alpha}); \tag{8.14}$$

provided that F_{LP} and F_{UP} are μ_C-measurable sets. Failure probability lower and upper bound calculated with the Random Set approach, Eq. (8.14), are denoted with a double line to distinguish them from the bounds calculated with the Double Loop approach of Eq. (8.12).

Eq. (8.14) can be evaluated by means of simple Monte Carlo method sampling n points from the copula C, namely $\boldsymbol{\alpha}_1, \boldsymbol{\alpha}_2, \ldots, \boldsymbol{\alpha}_n \in \boldsymbol{\Omega}$, and then retrieving the corresponding focal elements $\gamma_j := \Gamma(\boldsymbol{\alpha}_j), j = 1, \ldots, n$ from $\mathscr{F}$. Afterwards, integrals Eq. (8.14) are computed by the unbiased estimators $\hat{\underline{\underline{P_f}}}$ and $\hat{\overline{\overline{P_f}}}$, which are given by:

$$\hat{\underline{\underline{P_f}}} = \frac{1}{n} \sum_{j=1}^{n} \mathcal{I}\left[\boldsymbol{\alpha}_j \in F_{LP}\right], \quad \hat{\overline{\overline{P_f}}} = \frac{1}{n} \sum_{j=1}^{n} \mathcal{I}\left[\boldsymbol{\alpha}_j \in F_{UP}\right]. \tag{8.15}$$

The image of $\Gamma(\boldsymbol{\alpha}_i)$ through the function $\mathcal{G}$ can be computed using the optimisation method, as described by Eq. (2.9). Since, $\mathcal{I}\left[\mathcal{G}\left(\Gamma\left(\boldsymbol{\alpha}_i\right)\right) \subseteq F\right] = \mathcal{I}\left[\overline{\mathcal{G}}(\boldsymbol{\alpha}_i) > \mathcal{H}^{crit}\right] = \mathcal{I}\left[\boldsymbol{\alpha}_i \in F_{LP}\right]$ and $\mathcal{I}[\mathcal{G}\left(\Gamma(\boldsymbol{\alpha}_i)\right) \cap F \neq \varnothing] = \mathcal{I}\left[\underline{\mathcal{G}}(\boldsymbol{\alpha}_i) > \mathcal{H}^{crit}\right] = \mathcal{I}\left[\boldsymbol{\alpha}_i \in F_{UP}\right]$ it follows that Eqs. (8.15) can be written as:

$$\hat{\underline{\underline{P_f}}} = \frac{1}{n} \sum_{i=1}^{n} \mathcal{I}\left[\overline{\mathcal{G}}(\boldsymbol{\alpha}_i) > \mathcal{H}^{crit}\right], \quad \hat{\overline{\overline{P_f}}} = \frac{1}{n} \sum_{i=1}^{n} \mathcal{I}\left[\underline{\mathcal{G}}(\boldsymbol{\alpha}_i) > \mathcal{H}^{crit}\right]. \tag{8.16}$$

Note that this approach operates by inverting the order of loop execution of the Double Loop approach described above:

- the outer loop propagates the aleatory uncertainty by sampling the points $\boldsymbol{\alpha}_1, \boldsymbol{\alpha}_2, \ldots, \boldsymbol{\alpha}_n \in \boldsymbol{\Omega}$ using copula C.

- the inner loop drives an optimisation/search process in $\Gamma(\boldsymbol{\alpha}_i)$ in order to find the image of the input focal element through the system $\mathcal{G}$; this step is performed when evaluating Eq. (2.9).

One of the main advantages of the random set theory is that it can be used for problems where inputs are defined using any possible imprecise probability framework, such as CDFs, intervals, distribution-free probability boxes, possibility distributions, Dempster-Shafer structures and so on. In case the calculation of very small probability bounds is requested, the plain Monte Carlo simulation described here is not efficient. Advanced Monte Carlo methods can be used instead to estimate small probabilities of failure as described in Chapters 3,4 and 5.

It is worth noting that although the random set theory cannot model distributional p-boxes, the Random Set approach can still be used as far as the bounding CDFs of the input p-boxes can be identified. However, applying this approach to distributional p-boxes treats those p-boxes as distribution-free ones. This inevitably leads to loss of information which results in the underestimation and overestimation of the lower and upper bounds respectively, when compared to the Double Loop approach (or method of optimisation in the epistemic space).

8.3 Subproblem A

The aim of the uncertainty characterisation, called subproblem A, is to reduce the epistemic uncertainty components of category II (p_2) and III (p_1, p_4, p_5) given some experimental data. The subsystem provides a scalar output x_1 as a function of the following five uncertain parameters,

$$x_1 = h_1(p_1, p_2, p_3, p_4, p_5). \tag{8.17}$$

In this subproblem, the vector $[p_1, \dots p_5]$ is the output of the function $\mathcal{W}$, while the function h_1 is the equivalent of the performance function $\mathcal{G}$ already encountered in previous chapters. The epistemic space is the Cartesian product $\boldsymbol{\Theta} := \times_{i=j}^{8} I_j$ and the aleatory space, which models variables α_1 to α_4, is defined by $\boldsymbol{\Omega} := (0, 1]^4$ (see Table 8.1).

Two sets of 25 observations of the "true" uncertainty model $\boldsymbol{\theta}^* \in \boldsymbol{\Theta}$ are available to reduce the uncertainty in $\boldsymbol{\Omega}$. Here, the uncertainty model is characterised as "true" when it is free of epistemic uncertainty, representing an hypothetical situation where an infinite amount of experimental data is available.

A major challenge of subproblem A is the limited available information (25 observation points for each dataset) and the relatively large dissimilarity of the empirical CDFs associated with those datasets as shown in Figure 8.2.

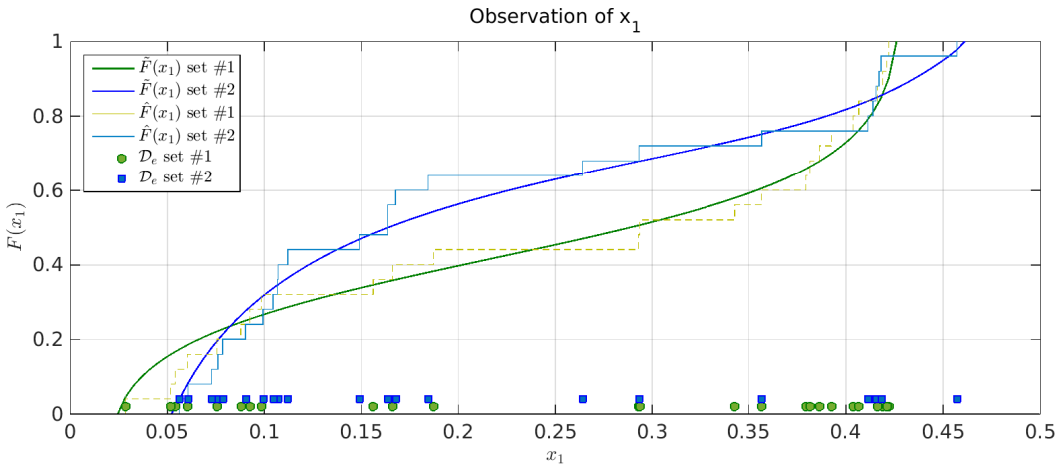

Figure 8.2: Empirical CDF, $\hat{F}$, of the two set of observation points and CDF obtained adopting the Gaussian kernel density of Eq. (8.4), $\tilde{F}$. The dots and squares show the two datasets $\mathcal{D}_e$, respectively.

8.3.1 Non-parametric statistic method based on the Kolmogorov-Smirnov test

The procedure presented in Session 8.2 has been used to solve subproblem A. First, the validation similarity level has been calculated after using a Gaussian KDE to compute the CDF $\tilde{F}_e$ for the observation sets. A validation similarity level $D_{\tilde{v}} = 0.18$ has been obtained calculating the maximum distance between the two KDEs adjusted to the two datasets respectively $\tilde{F}_e$ (i.e. using Eq. (8.3)). The measure of similarity obtained comparing the two empirical CDFs, $\hat{F}_e$, of the datasets is $D_{\hat{v}} = 0.24$ is shown in Figure 8.3. This enables identification of those points $\boldsymbol{\theta}_i \in \boldsymbol{\Theta}$ that conform with the observations such that $D_i < D_v$.

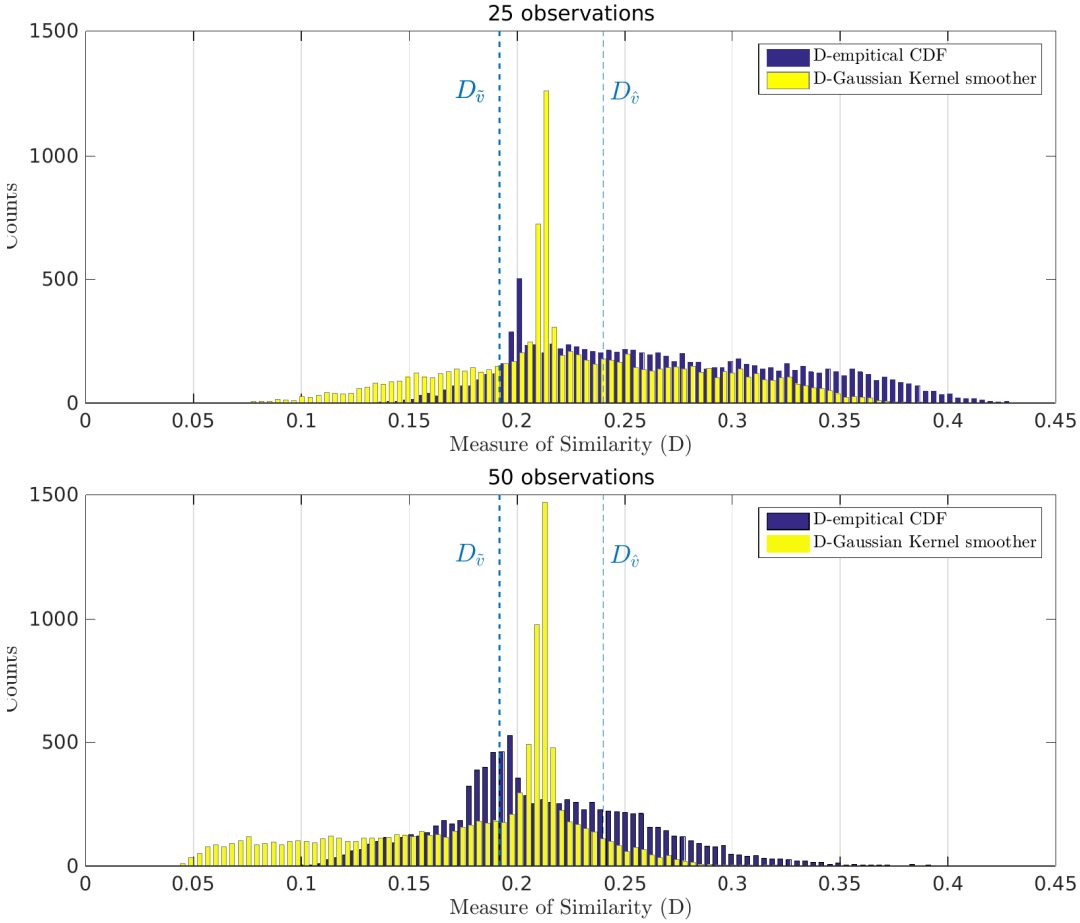

Figure 8.3: Histogram of the measure of similarity, D_i, between the CDF calculated sampling randomly in the epistemic space and the observations, for 25 (top panel) and 50 (bottom panel) observations ($\mathcal{D}_e$)

Assuming a uniform distribution on $\boldsymbol{\Theta}$, 10000 samples $\boldsymbol{\theta}_i$ are drawn, and for each $\boldsymbol{\theta}_i$, $n = 5000$ samples from the aleatory space $\boldsymbol{\Omega}$ are used to propagate the aleatory uncertainty through the model (using the function `p_to_x1`). Finally, using the empirical CDF of x_1 ($\hat{F}(x_1|\boldsymbol{\theta}_i)$), the measure of similarity D_i is calculated against $\tilde{F}_e$ according to

Eq. (8.3) (i.e. $D_i = \sup_x |\hat{F}(x|\boldsymbol{\theta}_i) - \tilde{F}_e(x)|$). Please note that due to the large number of samples used it holds $\hat{F}_i(x_1|\boldsymbol{\theta}_i) \approx \tilde{F}_i(x_1|\boldsymbol{\theta}_i)$. The histograms of the measure of similarity D_i are shown in Figure 8.3 computed for the dataset of 25 and 50 observations, respectively. It is possible to see that D_i is smaller when the KDE $\tilde{F}_i(x_1|\boldsymbol{\theta}_i)$ and all 50 observations are used. The smoothing effect of the Gaussian kernels can be appreciated in Figure 8.3, where the yellow histograms present higher peaks than the histograms obtained with empirical data.

The measure of similarity $D_{\tilde{v}} = 0.18$ identifies model outputs, x_1 obtained from the realisations in the epistemic space, $\boldsymbol{\theta}_i$, that are in agreement with the observations (represented in Figure 8.3 by the bars on the left of $D_{\tilde{v}}$). In Figure 8.3 the measure of similarity, D_i, has been computed using the empirical CDF of the experimental data (blue bars) and the CDF obtained using Gaussian kernel smoother functions (yellow bars). The figure also shows the values of the measure of similarity between the two sets of observation data computed using Gaussian kernel smoother techniques, $D_{\tilde{v}}$, and empirical CDF, $D_{\hat{v}}$, respectively. Calculating $P(D_i > D_{\tilde{v}}) = c$, two confidence levels have been obtained: $c_{\tilde{v}(25)} = 0.803$ and $c_{\tilde{v}(50)} = 0.547$ when D_i is calculated against the $\tilde{F}_e$ obtained using 25 and 50 observations, respectively. Figure 8.4 shows the parallel coordinate plot of the epistemic realisations. Please note that for readability purposes, only 1000 realisations are shown. In a parallel plot a multi-dimensional quantity is shown graphically and represented as a polyline with vertices on the parallel axes. The vertex on the m-axis corresponds to the i-th realisation of the m-coordinate (i.e. $\theta_m^{(i)}$). The axes of the plot have been normalised, between 0 and 1. The top panel of Figure 8.4 shows combination of epistemic realisations for different level of similarity measure computed against $\tilde{F}_e$ constructed from 25 observations. The Figure shows all the combinations of all epistemic realisations ($c = 0$), those with a similarity measure $D_i < D_{\hat{v}}$ (i.e. $c = 0.547$) and $D_i < D_{\tilde{v}}$ (i.e. $c = 8031$), respectively. The top panel of Figure 8.4 shows the parallel plot with measures of similarity calculated using all the 50 observations. $c = 0.0547$ corresponds to a similarity measure $D_i < D_{\tilde{v}}$ while $c = 0.0547$ corresponds to an arbitrary level $D_i < 0.1$.

The parallel coordinate plot enables identification of the epistemic uncertainty that can subsequently be reduced. For instance, all of the realisations of $\mathrm{E}[p_5]$ with similarity level lower D_v are in the normalised interval $[0, 0.6]$ while $\mathrm{E}[p_1]$ is in the normalised interval $[0, 0.7]$. On the contrary, the intervals of $\mathrm{Var}[p_1]$, p_2,$\mathrm{E}[p_4]$, $\mathrm{Var}[p_4]$, $\mathrm{Var}[p_5]$ and $\rho(p_4, p_5)$ cannot be improved based on the current available data. Figure 8.4 shows only 1000 realisations (over a total sample of 10000) of the epistemic space for different significant levels c of the Kolmogorov-Smirnov test. $c = 0$ represents all the realisations, $c_{\tilde{v}}$ represents realisations of θ with a measure of similarity $D_i < D_{\tilde{v}}$, $c_{\hat{v}}$ represents realisations of θ with a measure of similarity $D_i < D_{\hat{v}}$, and $c_{D=0.1}$ represents realisations with a measure of similarity $D_i < 0.1$. The results are summarised in Table 8.2.

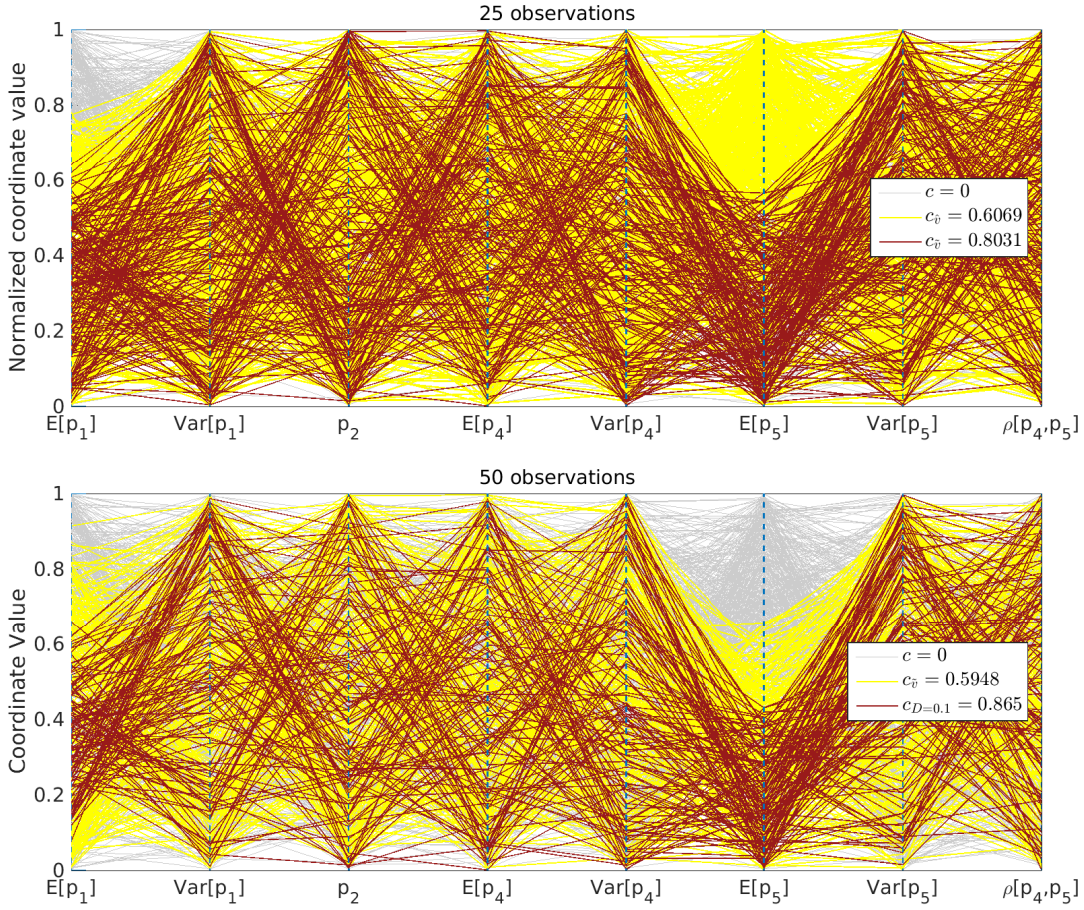

Figure 8.4: Parallel coordinates plot of the 8 category II and III parameters of the input factors of h_1 (i.e. $p_i, i = 1, \cdots, 5$) for 25 (top panel) and 50 (bottom panel) observations ($\mathcal{D}_e$)

8.3.2 Bayesian updating in the epistemic space

Bayesian inference has been performed as an alternative method to reduce the epistemic uncertainty as explained in Sections 8.2.1. In this method, Transitional Monte Carlo Markov Chains have been used to sample 1000 realisations from the posterior PDF $p(\boldsymbol{\theta}|\mathcal{D}_n)$. Two strategies have been deployed to estimate the likelihood $P(\mathcal{D}_e|\boldsymbol{\theta}_i)$: the standard Bayesian and an approximate Bayesian computational method.

Bayesian computational method (BC) In this case, the likelihood is computed using Eq. (8.5) and $p(x|\boldsymbol{\theta}_i)$ is estimated by means of a KDE, computed with $n = 1000$ points from the aleatory space. The posterior distributions are sampled using TMCMC with 25 and 50 observation points as evidence, respectively. Histograms of the posterior samples are normalised, assigning a value of 1 to the number of counts in the bin containing the majority of samples. After normalising the histograms, it is possible to set a general limit of normalised counts used to exclude outliers of the TMCMC algorithm, and indicated by the horizontal red lines in Figures 8.5.

Approximate Bayesian computational method (ABC) In this case, 200 samples are used to evaluate $\hat{F}(\cdot|\boldsymbol{\theta}_i)$ and the quantities δ_k by means of Eq. (8.9). Thereafter, the likelihood (8.8) is computed, and a normalised histogram of the posterior samples is obtained, which is slightly different from the one shown in Figure 8.5.

Results The proposed method has enabled the identification of a reduced epistemic space associated to $\mathrm{E}[p_1]$ and $\mathrm{E}[p_5]$ but no conclusions can be drawn for the other input parameters. The updated ranges of the epistemic uncertainties are summarised in Table 8.2. The Bayesian updating procedure successfully managed to reduce the uncertainty associated to the output x_1 as shown for example in Figure 8.6, for the approximate Bayesian computational method. Figure 8.6 shows different p-boxes of x_1 obtained with the updated epistemic uncertainty parameters, using the first set of 25 observations and the full set of 50 observations, respectively. The approximated p-boxes have been obtained using the following procedure. First, 10000 samples $\boldsymbol{\theta}_i$ of the epistemic variable are drawn from uniform distributions defined by the full range of the updated bounds (light grey) and by the updated bounds obtained excluding the outliers (dark gray). Then, the CDF $\hat{F}(\cdot|\boldsymbol{\theta}_i)$ is computed for each epistemic realisation. Finally the curves enveloping all the CDFs are obtained and shown in Figure 8.6.

It is possible to notice that the updated p-box of x_1 is tighter when all the 50 experimental observations are used. Additionally, the experimental CDFs of the calibration data set are fully contained in the light grey area (i.e. the p-boxes obtained excluding the outliers). However, the validation data lay inside the updated p-box only when the full intervals of updated parameters are considered.

The reduced uncertainty model identified by the non-parametric approach and by the Bayesian inference approach are summarised in Table 8.2, respectively. Although only the uncertainty of parameters p_1 and p_5 can be significantly reduced, the results produced by the proposed approaches are in agreement, as they provide a cross validation of the developed procedures used to solve the subproblem A.

Table 8.2: Reduced uncertainty model using the non-parametric approach ($c = 0.547$) or 25 observations and $c = 0.803$ for 50 observations and the Bayesian inference, respectively. The double dash – means that the method could not reduce the epistemic uncertainty for the referred variable.

Variable	Original interval	Nonparametric method	Bayesian methods BC	Bayesian methods ABC
		25 observations		
E[p_1]	[0.6000, 0.80]	[0.6000, 0.72]	[0.6000, 0.73]	[0.6030, 0.755]
Var[p_1]	[0.0200, 0.04]	–	–	–
p_2	[0.0000, 1.00]	–	–	–
E[p_4]	[-5.0000, 5.00]	–	–	–
Var[p_4]	[0.0025, 4.00]	–	–	–
E[p_5]	[-5.0000, 5.00]	[-5.0000, 0.78]	–	[-5.0000, 4.50]
Var[p_5]	[0.0025, 4.00]	–	–	–
$\rho(p_4, p_5)$	[-1.0000, 1.00]	–	–	–
		50 observations		
E[p_1]	[0.6000, 0.80]	[0.63, 0.76]	[0.60, 0.75]	[0.618, 0.791]
Var[p_1]	[0.0200, 0.04]	[0.0260, 0.04]	–	–
p_2	[0.0000, 1.00]	–	–	–
E[p_4]	[-5.0000, 5.00]	[-4.50, 4.80]	–	–
Var[p_4]	[0.0025, 4.00]	–	–	[0.097, 3.943]
E[p_5]	[-5.0000, 5.00]	[-4.90, 0.30]	–	[-5.00, 4.45]
Var[p_5]	[0.0025, 4.00]	–	–	–
$\rho(p_4, p_5)$	[-1.0000, 1.00]	–	–	–

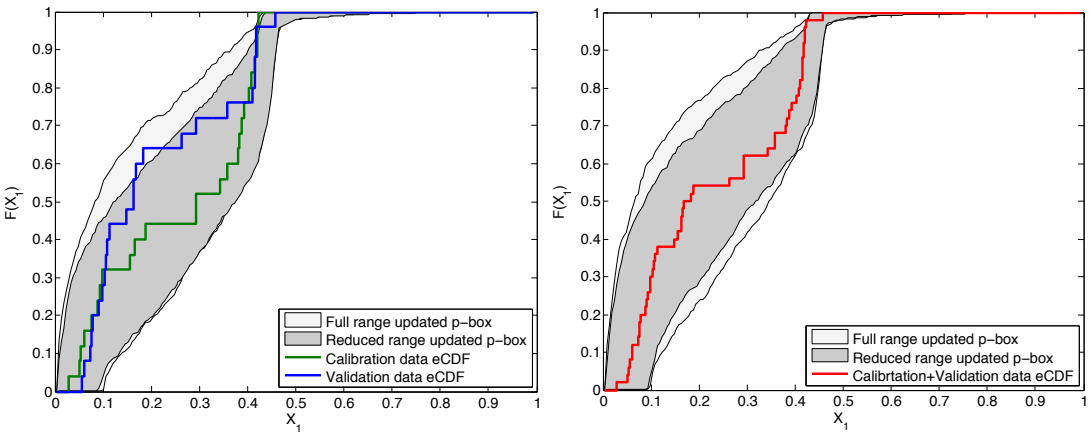

(a) 25 observations. **(b)** 50 observations.

Figure 8.6: P-boxes of x_1 and the empirical CDFs of the experimental data. The p-boxes have been obtained using the full range of the posterior parameters and using the range that excludes the outliers, respectively.

8.4 Subproblem C

For this subproblem, we were asked to find the range of the metrics $J_1 = E[w(\boldsymbol{p}, \boldsymbol{d}_{\text{baseline}})]$ and $J_2 = 1 - P[w(\boldsymbol{p}, \boldsymbol{d}_{\text{baseline}}) < 0]$, both with the reduced and

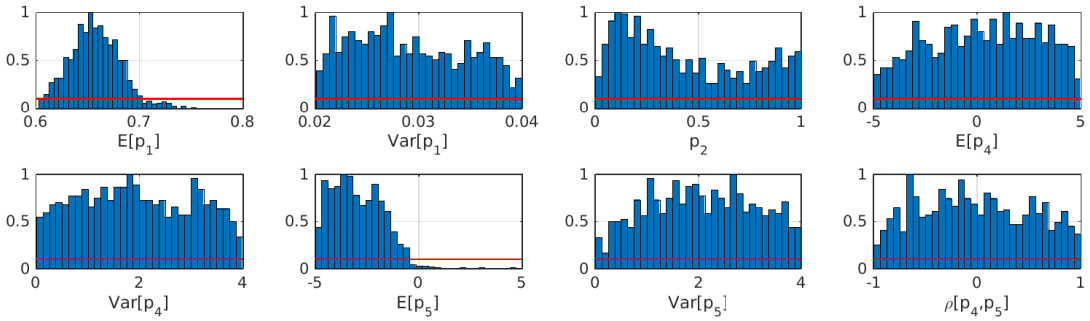

(a) 25 observations.

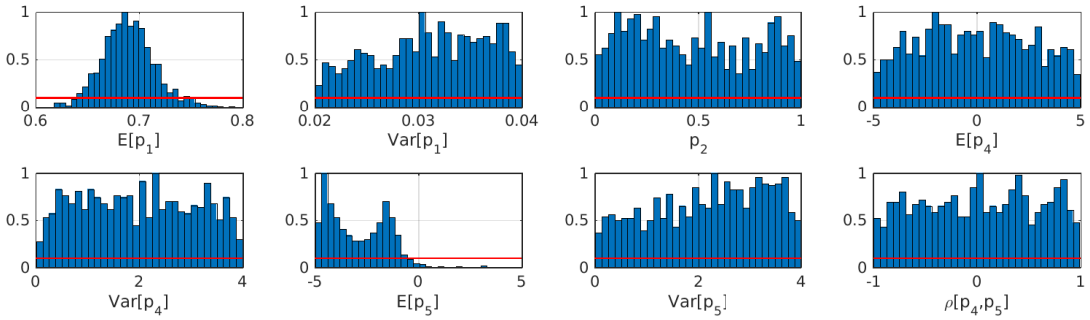

(b) 50 observations.

Figure 8.5: Normalised histogram of $p(\boldsymbol{\theta}|\mathcal{D}_e)$ obtained using Approximate Bayesian Computational method with (a) 25 experimental observations and (b) 50 experimental observations (b) of x_1, respectively. The normalization assigns a value of 1 to the bin with the highest number of counts. The red line represent the cut-off value to determine the updated range.

with the improved uncertainty models. The metric J_1 is the expected value of the worst-case requirement metric w, while the metric J_2 represents the failure probability of the system. For solving this subproblem the two strategies introduced in Section 8.2 have been used.

8.4.1 Optimisation in the epistemic space (Double Loop approach)

A global optimisation is performed in the epistemic space $\boldsymbol{\Theta} \equiv \times_{i=1}^{31} I_i$, in order to find those points in $\boldsymbol{\Theta}$ that produce the upper and lower bounds on J_1 and J_2. For any candidate solution provided by the optimisation algorithm , i.e. $\boldsymbol{\theta}_i \in \boldsymbol{\Theta}$, a set of $n = 1000$ random points $\{\boldsymbol{\alpha}_j, j = 1, 2, \ldots, n\}$ are drawn from the aleatory space $\boldsymbol{\Omega} \equiv (0, 1]^{17}$ to estimate the metrics J_1 and J_2. The number of samples from the aleatory space has been selected after performing a convergence test. More specifically, in this test, both J_1 and J_2 are estimated with increasing values of n (i.e. 100, 500, 1000, 5000 and 10000) for 5 representative realisations of the epistemic space, as shown in Figure 8.7. From the figure, it can be seen that $n = 1000$ points are sufficient for estimating J_1 and J_2, with a C.o.V. of 0.1 and 0.05 respectively. The confidence of these estimates can be improved by using a larger sample size at the expense of much more computational cost. The

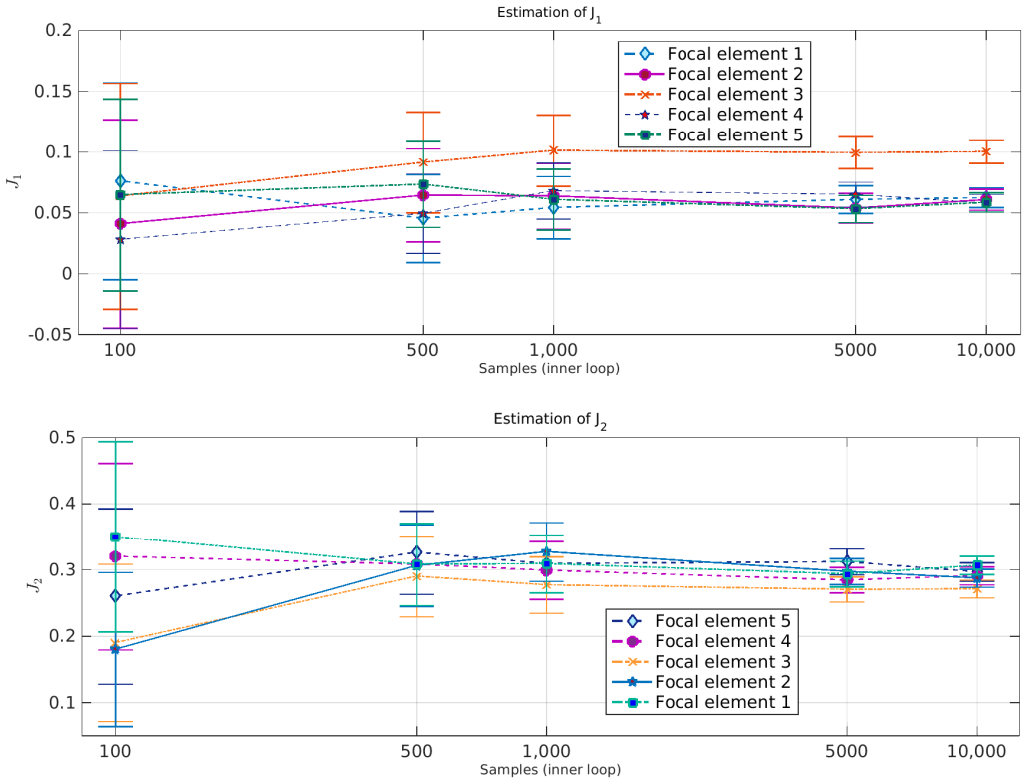

Figure 8.7: Effect of the number of samples generated in the aleatory space for the inner loop estimation of J_1 and J_2.

search for lower and upper bounds is performed by means of Monte Carlo optimisation using Latin Hypercube sampling, with approximately 50000 samples. A total of 5×10^7 evaluations of the function `x_to_g` (model $\boldsymbol{f}$) are thus required to complete the analysis. Here, Monte Carlo is a convenient method to solve the optimisation, as the objective functions J_1 and J_2 can be quite noisy, varying approximately between $\mp 10\%$ of the true value. In order to take into account of the estimation error introduced by using finite sample sets, the objective functions *maximum* and *minimum* of $J_{i=1,2}$, are redefined as lower J_i $(1 - t_{\alpha/2}\,\mathrm{C.o.V.})$ and upper J_i $(1 + t_{\alpha/2}\,\mathrm{C.o.V.})$ estimations, respectively, where $\alpha = 0.14$ and $t_{\alpha/2} = 1.48$ is the 86th t-Student percentile (see also [59]).

Note that, in order to run the analysis within a reasonable time, parallelisation lies at the foundations of this approach. On a common dual-core personal computer, a single estimation of J_i takes approximately 3.4 minutes, thus a total of ∼120 days for a complete analysis. By means of a double parallelisation, it has been possible to reduce the running time by two orders of magnitude, making it possible to complete the analysis in just $\sim$ 80 hours. A double parellelisation strategy, unlike a standard parallelisation, makes use of both local processors and cluster units to process the jobs. In other words, the jobs are first sent in parallel to the cluster units and subsequently distributed to every processing units on each cluster machine. In this way, approximately one hundred

percent of the computing power available on the cluster machines is used.

8.4.2 Propagation of focal sets (Random Set approach)

Using the propagation of focal sets method, $n = 1000$ random vectors $\{\boldsymbol{\alpha}_j, j = 1, 2, \ldots, n\}$ are drawn from the aleatory space $\boldsymbol{\Omega} \equiv (0, 1]^{17}$. In order to evaluate equations (2.8) and (2.9), genetic algorithms with a population of 125 individuals and 50 generations are adopted requiring a total computational cost of 5×10^6 evaluations of w. Figure 8.8 shows the convergence of the genetic algorithms for two representative focal elements. The convergence is achieved using 30 generations for the identification of the minimum/maximum of the Eq. (2.9).

For this approach, parallelisation is also essential. In fact, approximately 5×10^6 evaluations of the function `x_to_g` are required to complete a full analysis. Although, in this case, the use of GA makes the parallelisation a little more articulated (jobs need to be sent at any iteration of the algorithm), it is still possible to significantly reduce the running time by approximately one or two orders of magnitude (as in the standard approach).

Results The results of the reduced uncertainty model and the improved model are summarised in Table 8.3.

Using the proposed methods, it has been possible to bound the actual solution for the targeted metrics. As expected, the improved uncertainty model is far more informative than the reduced model, which is shown by a sensible reduction in the upper bound of J_1. An even more significant difference is documented for the range of J_2 (see Table 8.3), where the model of uncertainty from being totally uninformative, $J_2 \in [0,\ 1]$, is reduced to $J_2 \in [0.20,\ 0.41]$. In Table 8.3, the bounds of J_1 and J_2 are obtained by means of the two proposed approaches, i.e. optimisation in the epistemic space and propagation of focal sets, respectively. Note also that the optimisation in the epistemic space (standard approach) provided tighter bounds than the propagation of focal sets (counter approach). This result was expected in as much as, the random set methodology cannot cope with distributional probability boxes, and has to treat them as distribution-free p-boxes.

Computation using the optimisation approach in the epistemic space is less intensive than the propagation of focal sets, since only four optimisation tasks are required to find the lower and upper bounds of J_1 and J_2; while the counter (Random Set) approach requires a pair of optimisation tasks for each focal element and for each quantity of interest (i.e. J_1 and J_2). On the other end, the Random set approach performs an optimisation on a deterministic objective function which increases the chances to find the global optima.

Table 8.3: Bounds of the statistics J_1 and J_2 for the reduced and improved uncertainty model

Reduced Uncertainty model	Improved Uncertainty model	Approach
$J_1 = [1.37 \times 10^{-2},\ 4.97]$	$J_1 = [2.88 \times 10^{-2},\ 1.11]$	Double Loop
$J_2 = [6.4 \times 10^{-2},\ 0.82]$	$J_2 = [0.24,\ 0.38]$	
$J_1 = [-1.57 \times 10^{-4},\ 54.05]$	$J_1 = [-1.10 \times 10^{-4},\ 3.05]$	Focal Sets
$J_2 = [0,\ 1]$	$J_2 = [0.20,\ 0.41]$	

Both approaches are based on global optimisation strategies and hence, they both suffer from the curse of dimensionality. The approaches proposed require an increasingly larger sample size (number of individuals and generations) in order to explore properly the optimisation domain. In consequence, it may not be guaranteed that the calculated optima are actually the global optima. In forward uncertainty propagation, missing the global optima may means computing ranges of the targeted variables that are narrower than the sought ones. In this case, the methods result in an under(inner)-estimation of the actual solution, which may lead to an under-prediction of the targeted metric.

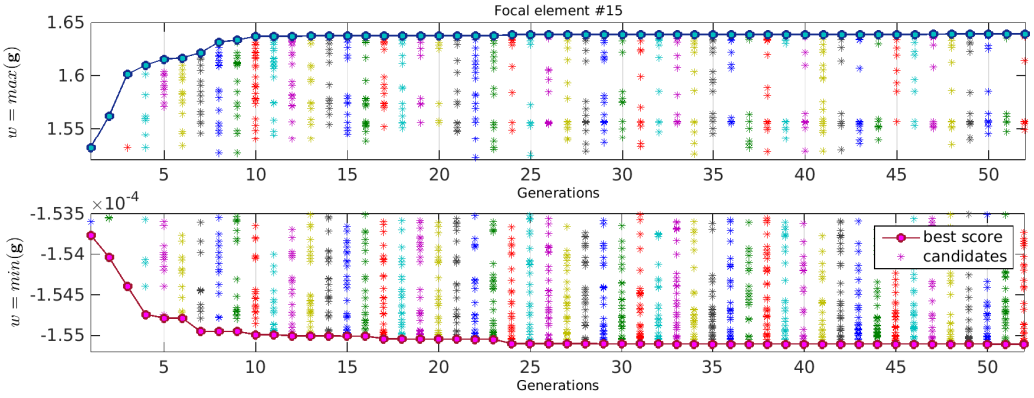

Figure 8.8: Convergence of the objective function, w, to the *minimum* and *maximum* for a representative focal element. Genetic Algorithms have been used with a population of 1000 individuals converging after 53 iterations.

8.5 Subproblem D

Subproblem D aims at identifying the epistemic realisations that lead to the smallest and largest values of J_1 (task D1) and J_2 (task D2). The extreme case analysis has been performed both for the reduced uncertainty model and the improved uncertainty model, as requested. However, for conciseness, only results from the improved model will be presented.

The extreme case analysis in presence of uncertainty is an ill-posed inverse problem. The direct identification of the epistemic realisations, $\boldsymbol{\theta}$, leading to the maximum/minimum of J_1 and J_2 from the forward simulation has not been possible. Further, due to the complexity of the problem (in terms of nonlinearity and computational costs), a specific strategy has been developed as explained in the following section.

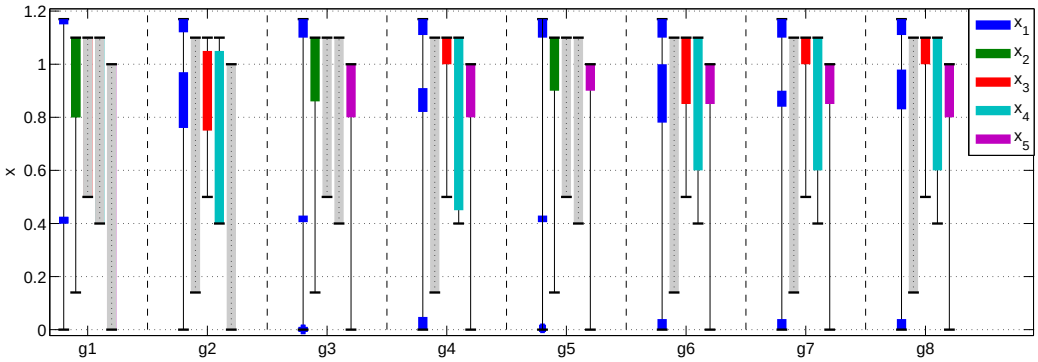

Figure 8.9: Analysis of the performance function $\boldsymbol{g}$ with respect to the output of the subdisciplines, $\boldsymbol{x}$. In the plot the ranges of $x_{i=1:5}$ leading to large positive values of $g_{i=1:8}$ are shown using coloured bars. Grey bars (and dashed lines) indicate variables that are not important for the maximum of the corresponding performance g_i)

8.5.1 Extreme values of J_1 (task D1)

In this task we are focusing on $J_1 = E[w]$ that is the expectation (mean) of the worst-case requirement metric: $w = \underset{i=1:8}{max}(g_i)$. In order to be able to identify the realisations of the inputs $\boldsymbol{p}$ that produce the extreme values of J_1, the relationships among intermediate variables, $\boldsymbol{g}$, $\boldsymbol{x}$ and $\boldsymbol{p}$ are analysed.

Dependence of J_1 on w The extreme values of J_1 depend on the presence of very large (but rare) values of w (hereafter indicated as *outliers* of w). The outliers of w can assume values $w > 1000$, while the most probable values of w are limited to values around 0. Two very distinct classes for w have been identified. A first class identifies values where $w < 3$, and a second class identifies the outliers, where $w > 100$ and have values as high as 1000. Hence, J_1 may assume its smallest value only if no outliers are present. On the other hand, the more outliers are present, the larger the value of J_1.

Dependence between $\boldsymbol{g}$ and $\boldsymbol{x}$ Next, the dependence between the performance functions of the system $\boldsymbol{g}$ and the output of subdisciplines $\boldsymbol{x}$ is analysed. The interest is to identify values (and ranges) of $\boldsymbol{x}$ that produce the maxima of the performance functions $\boldsymbol{g}$.

This study is performed by means of an optimisation procedure where $g_{i=1:8}$ are the objective functions to be maximised and $\boldsymbol{x}$ are the search variables. A Genetic Algorithm with 243 individuals and 50 generations is used for analysing each performance function g_i. The results are shown in Figure 8.9. The analysis of the function x_to_g (i.e. the model f) has revealed that only the performance functions $g_{i=3:8}$ yield values $w > 100$, while g_1 and g_2 are always lower than 1 and 2.8, respectively.

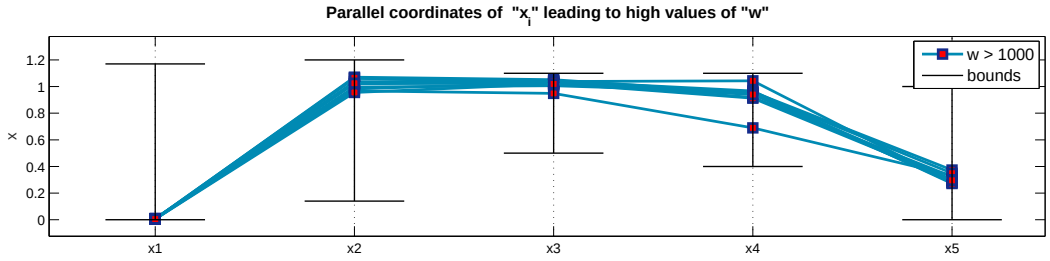

Figure 8.10: Parallel coordinates of $x_{i=1:5}$ leading to the outliers of w. The plot shows also the bounds of the variables $x_{i=1:5}$ identified for the improved uncertainty model.

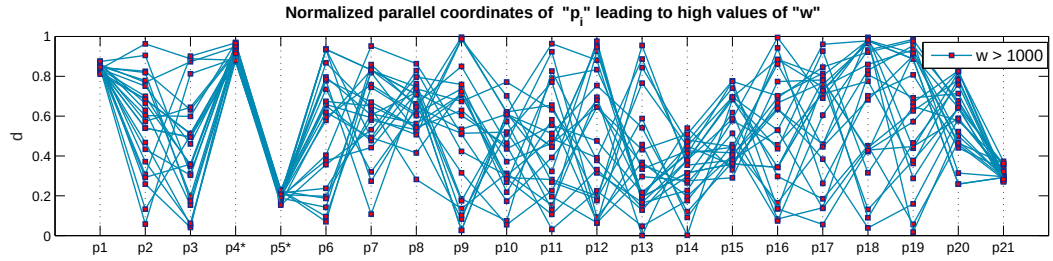

Figure 8.11: Parallel coordinates of the inputs $p_{i=1:21}$ leading to values of $w > 1000$ and $J_1 > 1.0$. The y-axis has been normalised between the lower and upper bound of the inputs $p_{i=1:3,6:21}$. p_4 while p_5 have been normalised to the interval $[-5,\ 5]$.

Then, the individuals that produce $g_1 > 0.1$, $g_2 > 0.1$ and $g_{i=3:8} > 100$ are collected and shown in Figure 8.9 using coloured bars. Some variables, shown in the Figure using grey color and dashed line, do not influence the maximum of the performance functions (i.e. they can assume any value within their bounds).

From Figure 8.9 critical sets (or regions) for each variable x_i can be identified. For instance, there are three sets of x_1 able to produce values of $g_4 > 100$, namely $x1 \in [0,\ 0.05] \cup [0.82,\ 0.91] \cup [1.11,\ 1.17]$. However, these sets have been found without taking into account the probability distributions associated to the inputs $p_{i=1:5}$. The most probable regions of $\boldsymbol{x}$ have been identified by means of the double loop Monte Carlo simulation used in Section 8.4. Interestingly, the most probable realisations of $\boldsymbol{x}$ that produce outliers of w belong to a very clear pattern of coordinates, as shown in Figure 8.10.

Dependence between $\boldsymbol{x}$ and $\boldsymbol{p}$ Once the regions of $\boldsymbol{x}$ that produce the outliers of w have been identified, it is necessary to establish if such critical sets can be produced by any feasible realisations of inputs $\boldsymbol{p}$. This analysis has been performed by studying the functions p_to_x (i.e. the model h) by using a double loop Monte Carlo approach, with an outer loop of 10000 Latin Hypercube samples (for the epistemic uncertainty, $\boldsymbol{\theta}$) and an inner loop (for the aleatory uncertainty, $\boldsymbol{\alpha}$) of 1000 samples.

Table 8.4: Epistemic realisations of p_4 and p_5 leading to the maximum of J_1

	$\pi_{p_i}^{\max}$	Critical range (R_c)	Epistemic real.		
p_4	0.9912	$3.72 < p_4 < 4.70$	$E(p_4) = 4.21$	$V(p_5) = \underline{V}(p_4)$	$\rho = 0$
p_5	0.9912	$-3.46 < p_5 < -2.70$	$E(p_5) = -3.04$	$V(p_5) = \underline{V}(p_5)$	$\rho = 0$

Table 8.5: Epistemic realisations of p_1, p_{14}, p_{15} and p_{21} leading to the maximum of J_1

	$\pi_{p_i}^{\max}$	Critical range (R_c)	Epistemic real.	
p_1	0.141	$0.81 < p_1 < 0.9$	$E(p_1) = \overline{E}(p_1)$	$V(p_1) = \underline{V}(p_1)$
p_{14}	0.854	$0.00 < p_{14} < 0.54$	$a(p_{14}) = \underline{a}(p_{14})$	$b(p_{14}) = \overline{b}(p_{14})$
p_{15}	0.940	$0.29 < p_{15} < 0.78$	$a(p_{15}) = \overline{a}(p_{15})$	$b(p_{15}) = 6.498$
p_{21}	0.077	$0.27 < p_{21} < 0.45$	$a(p_{21}) = \overline{a}(p_{21})$	$b(p_{21}) = \underline{b}(p_{21})$

Epistemic realisations that produce maximum of J_1 Figure 8.11 shows the identified realisations of $\boldsymbol{p}$ that produce critical values of $\boldsymbol{x}$ (as shown in Figure 8.9). Only some inputs can lead unequivocally to the critical values of $\boldsymbol{x}$, namely p_1, p_4, p_5, p_{14}, p_{15} and p_{21}. In the matter of p_4 and p_5, only values in the region where $3.72 < p_4 < 4.70$ and $-3.46 < p_5 < -2.70$ can produce x_1 in the critical set, and hence leading to large values of w. Since p_4 and p_5 are normally distributed, it is possible to select distributions peaked around the identified region as shown in Table 8.4. The epistemic realisations of Table 8.4 are calculated by maximizing the joint probability $\pi_{p_4p_5} = P[3.72 < p_4 < 4.70,\ -3.46 < p_5 < -2.70]$. Using the distribution parameters reported in Table 8.4, such target maximum probability is $\max_{\Theta}(\pi_{p_4p_5}) = 0.9912$. The parameters of the multivariate distribution are calculated maximizing the probability π_{p_i} of being inside the specified ranges (i.e. Critical range R_c).

Epistemic realisations corresponding to parameters p_1, p_{14}, p_{15} and p_{21} are also calculated in a similar way. Table 8.5 shows the epistemic realisations of these inputs corresponding to the critical values, and the second column shows the corresponding values of the maximum probabilities π_{p_i}. These realisations maximise the probability of the input parameter π_{p_i} of being inside the specified ranges (R_c).

p_1 and p_{21} are somehow problematic inputs in the determination of the epistemic realisation. By analysing the realisations from the input parameters p_1 and p_{21}, it can be seen that critical values of $\boldsymbol{x}$ are obtained when $0.805 < p_1 < 0.902$ and $0.27 < p_{21} < 0.45$, respectively. However, from the p-boxes associated to these inputs (see Figures 8.12 and 8.13), it is not possible to select any CDF within the p-box of p_1 and p_{21} that permits it to exclude (or include) completely the critical realisations (shown as round dots in Figures 8.12 and 8.13). The Epistemic realisations of the remaining parameters $\boldsymbol{p}$, which do not appear to have influence on the generation of the critical values of w (see Figure 8.11), have been obtained by maximizing the probability $\nu_c = P[w > 1000 \mid p_i \in R_c(p_i)]$ for $i = 1, 4, 5, 14, 15, 21$. A random search for the maximum values of the mean of p_i has been performed. 1000 aleatory samples have been used to calculate the above conditional probability. The results are reported in Table 8.6. The

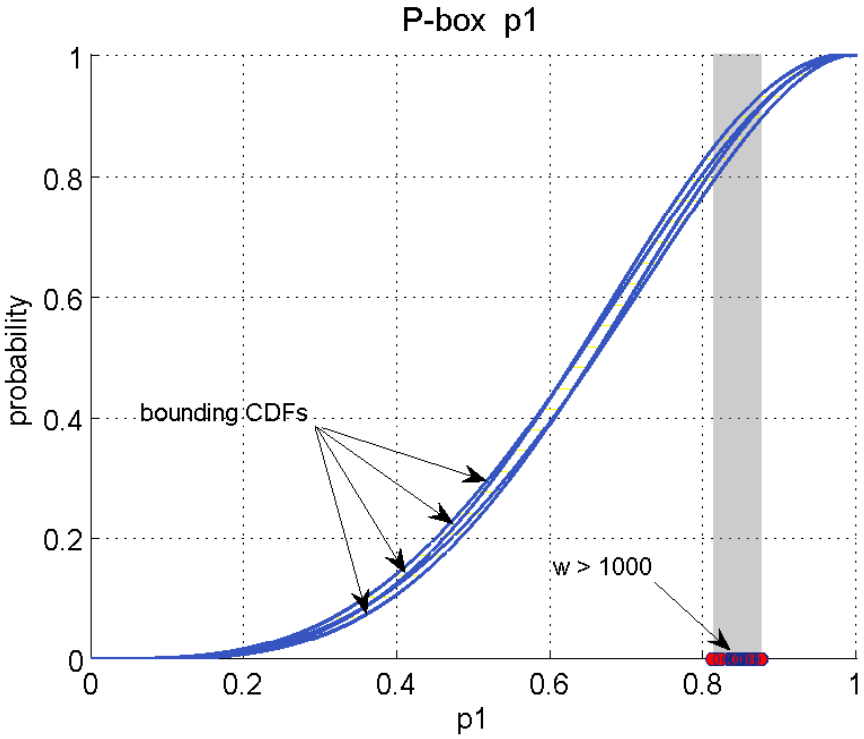

Figure 8.12: P-box representation of parameter p_1 . The grey area shows the range of p_1 that produces critical values of $\boldsymbol{x}$ and in turn large values of w

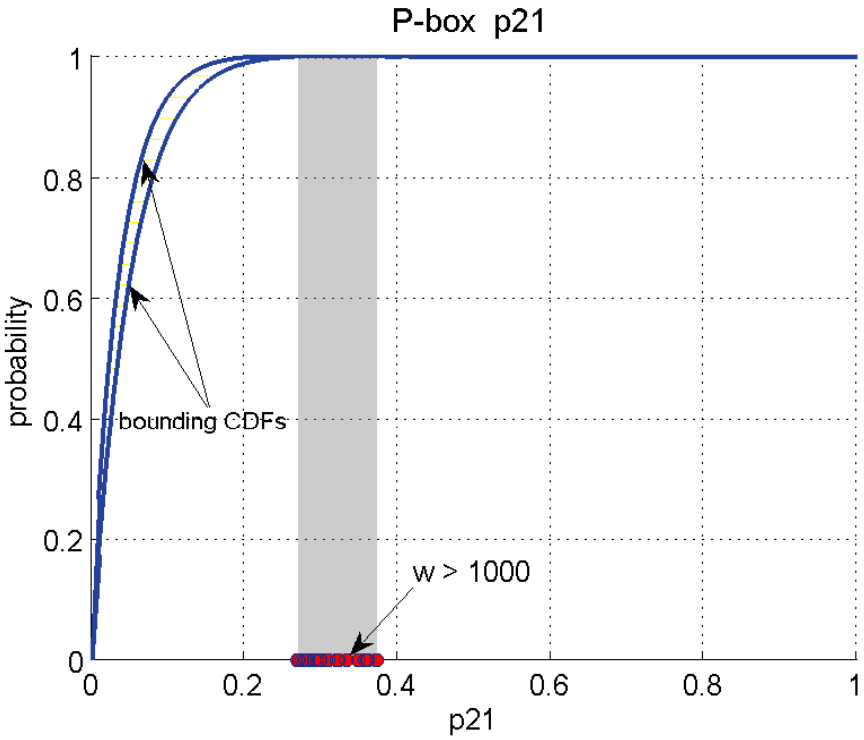

Figure 8.13: P-box representation of parameter p_{21}, respectively. The grey area shows the range of p_21 that produces critical values of $\boldsymbol{x}$ and in turn large values of w

Table 8.6: Epistemic realisation that are very likely to produce the maximum of J_1. The realisation has been identified maximizing the probability ν_c.

Parameter	Epistemic real.	Parameter	Epistemic real.
p_2	0.719	p_{12}	$\underline{p_{12}}$
p_6	0.760	p_{13}	$a = 0.45, b = \overline{b}$
p_7	$a = \underline{a}$, $b = 0.73$	p_{16}	0.590
p_8	$a = \overline{a}$, $b = \underline{b}$	p_{17}	$a = \underline{a}$, $b = 1.32$
p_{10}	$a = 3.55$, $b = \overline{b}$	p_{18}	$a = 3.26$, $b = \underline{b}$
p_{12}	$\underline{p_{12}}$	p_{20}	$a = 10.68, b = \overline{b}$

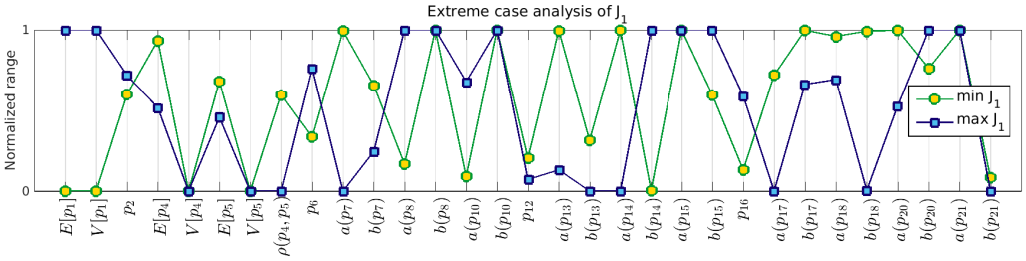

Figure 8.14: Extreme case analysis of J_1: parallel plot of the epistemic parameters. The y-axis represents normalised values of the epistemic variables.

maximum identified frequencies is $\nu_c^{\max} = 0.572$ and minimum $\nu_c^{\min} = 0.261$. These values are quite close meaning that the epistemic uncertainty may play a secondary role for the extreme value of J_1.

The parameters of the p-boxes have been calculated using the identified values of $E[p_i]$ and the maximum admissible value for $V[p_i]$.

The realisation leading to the minimum of J_1 can be directly identified from results of task C1 (see Section 8.4). The results are summarised in Figure 8.14.

8.5.2 Extreme values of J_2 (task D2)

The task D2 asks to identify the extreme case for metric J_2, where $J_2 = P[w \geqslant 0]$ is the failure probability of the worst-case requirement metric $w = \underset{i=1:8}{max}(g_i)$. Differently from J_1, this metric is not sensitive to the largest values of w. A double loop Monte Carlo approach has been adopted to solve this problem. 1000 aleatory samples have been used to compute the failure probability J_2. It is known from Section 8.4 that both lower and upper bounds of J_2 are greater than 10^{-1}, hence 1000 samples are enough for a sufficiently robust estimation of J_2 in the analysis.

The realisations of the input parameters $\boldsymbol{p}$ that produce the extreme values of J_2 are shown in Figure 8.15. Results from this analysis show, as expected, that realisations leading to the maximum (minimum) of J_2 are generally different from those leading to the maximum (minimum) of J_1. It is also noted that many realisations are very close to the bounds of the epistemic domain.

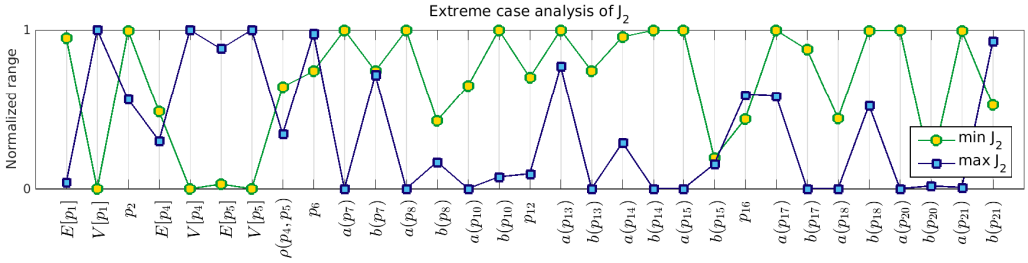

Figure 8.15: Extreme case analysis of J_2: parallel plot of the epistemic parameters. The y-axis represents normalised values of the epistemic variables.

8.5.3 Solution of task D3

In task D3, it is asked to identify some representative realisations of $\boldsymbol{x}$ that typify different failure scenarios.

The results of this task have already been discussed in Section 8.5 and visualised in Figure 8.9. Overall, the following failure scenarios have been identified:

- Values of $x_{i=1:5}$ close to their upper bounds lead to large values of $g_{i=1:8}$;
- Small values of x_1 combined with large values of $x_{i=2,3,4,5}$, lead to values of $g_{i=3,4,5,6,7,8} > 1000$;
- Values of $x_1 \in [0.84,\ 0.9]$ combined with large values of $x_{i=2,3,4,5}$, lead to values of $g_{i=4,6,7,8} > 1000$
- Values of $x_1 \in [0.4,\ 0.425]$, combined with large values of $x_{2,3,4,5}$, lead to values of $g_1 > 0.1$ and $g_{i=3,5} > 1000$.

Analysing the results of the simulations used in Section 8.4 (Genetic Algorithm with 125 individuals and 45 generations), it is also possible to study the relationship between $\boldsymbol{x}$ and $\boldsymbol{g}$. For example, large positive values of g_5, whose maximum is $g_5^{\max} = 1021$, are insensitive to x_3 and x_4. This can be appreciated in Figure 8.16, where the evolution of the objective function g_5 and search variables x_i are represented. During the optimisation the values of variables x_3 and x_4 change frequently, despite the value of the objective remaining the same. This suggests that the maximum value of the target function g_5 is insensitive to variables x_3 and x_4. Analogously, for the other targets, it is found that large positive values of g_4, g_6, g_7 and g_8 are totally insensitive to x_2 and slightly insensitive to x_4.

8.6 Chapter summary

In this chapter, most of the results obtained for the solution of the NASA Langley Multidisciplinary UQ Challenge [20] have been presented. The model provided by the challengers, describes the dynamics of a remotely operated twin-jet aircraft developed by

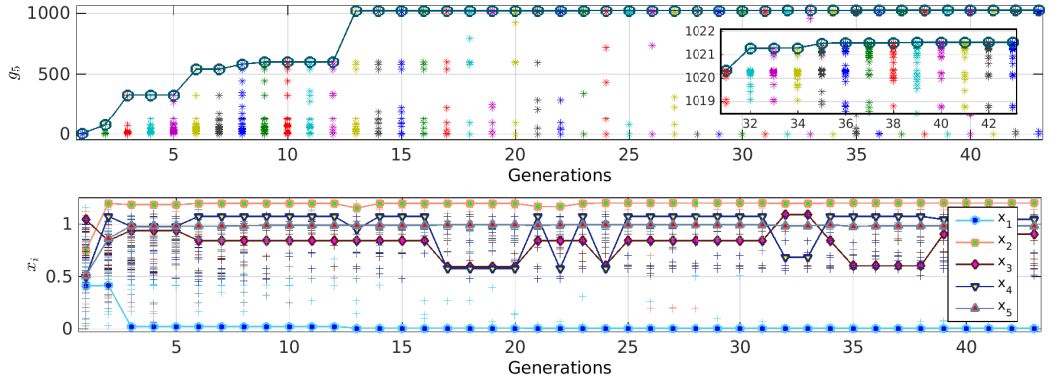

Figure 8.16: Evolution of the objective function g_5 and search variables x_i

NASA Langley Research Center. Being able to control the aircraft from ground stations, beyond the normal flying envelope, using a set of control parameters, and accounting for all the uncertainties represents a real challenge, as the functions describing the vehicle stability and performance characteristics are obtained from a "Black Box" model. The challenge is organised in 5 subproblems, which are: uncertainty characterisation, sensitivity analysis, uncertainty propagation, extreme case analysis and robust design, arranged to increasing levels of detail and required computational power. In uncertainty characterisation, data limitation is assessed and decisions are made as to whether and to what extent more data needs to be collected. The sensitivity analysis identifies the most and least important parameters to track and to disregard, respectively, in subsequent investigations. The uncertainty propagation computes the mean, variance and failure probability of the system response, whereas the extreme case analysis identifies the epistemic realisations responsible for the lower and upper bounds of the computed mean, variance and failure probability. Eventually, the robust design makes use of the uncertainty propagation to perform an optimisation in the space of the design parameters, in the attempt to minimise the upper bound of the mean value and the upper bound of the failure probability.

The efficiency of the presented uncertainty quantification techniques have been put to test in this case study. In fact, despite the extensive parallelisation and the efficient sampling methods, some subproblems still required from two to three days of computations to be completed. The complexity and dimensionality of the system functions make pattern identification extremely difficult, preventing the use of targeted sampling for the computation of failure probability. To the author's best of knowledge, the rigorous focal set propagation on "Black Box" models, performed without resorting to empirical global optimisation techniques, thus giving proof of the obtained global optima, remains an open problem.

The results presented in this chapter have been peer-reviewed and published in Ref. [50] (see also journal paper 2 from the List of Publications).

Chapter 9

Conclusions and Recommendations

9.1 Concluding remarks and summary

The doctoral investigation presented in this dissertation has developed novel methods to enhance the efficiency of uncertainty quantification, being able to deal with both aleatory and epistemic uncertainty. While Random Sets are well established tools for generalised uncertainty quantifications, at the same time they still appear to be used by a limited number of researchers. Among the many reasons why Random Sets are not embraced by most of the scientific engineering community, are that the computational cost represents a major limitation, which can be discouraging for application to engineering practice. Quantification of uncertainty in engineering, to deal with subjectivity and, in general, with epistemic uncertainty, seems to be oriented to Bayesian methods. However, the computational costs associated with Bayesian analyses can be cumbersome too, and it is often incompatible with industry pace.

Beyond philosophical reasoning, there appear to be no reasons as to why the Bayesian should be preferred to the Random Set approach, as long as the two approaches share equivalent computational cost. As we enter an era of high performance computing, where parallelisation on a large scale becomes widely accessible, the Random Set approach gains a lot of ground over the Bayesian one, since it can be implemented as a combination of Monte Carlo strategies and Global Optimisation methods, as has been illustrated in this work. On the contrary, Bayesian methods still strongly rely on sequential sampling algorithms, such as Metropolis Hastings or Gibbs sampling, which benefit a little from extensive parallelisation.

The development and implementation of efficient Random Set methodologies may eventually give rise to a new era of uncertainty quantification to encompass subjectivity and epistemic uncertainty on a systemic basis. Random Sets add robustness to the reliability analysis and design of new systems, and can be seen as the new frontier of uncertainty quantification.

In this dissertation, computational strategies have been developed to combine Random Sets with Advanced Sampling methods in the direction of robust reliability analyses. While, on one side, Random Sets allow for the inclusion of imprecision to provide a robust measure of reliability; on the other hand, Importance Sampling methods accelerate the analysis, as they significantly reduce the number of samples required to estimate upper and lower reliability bounds. More specifically, Line Sampling has been presented as a method for efficient probability estimations, which has been demonstrated to be more efficient than standard Monte Carlo implementation by many orders of magnitude. This happens because, contrary to standard Monte Carlo, the efficiency of Line Sampling is independent of the magnitude of the probability target.

Naive applications of Line Sampling to estimate probability intervals are possible using a Double Loop approach, but to the price of a little loss of generality. This is because the Double Loop approach is limited to include only parametric p-boxes and intervals, whereas Random Sets comprise a wider range of uncertainty objects, such as distribution-free p-boxes, Dempster-Shafer structures and fuzzy possibility distributions. However, we note that in the majority of applications where imprecision is accounted for, the Double Loop approach still represents a potent tool for estimating upper and lower reliability bounds.

The combination of Line Sampling with the Random Set approach has shown two great advantages. First, it allows for a general uncertainty quantification, as any class of Random Set can be included in the analysis. Second, it is independent from the magnitude of the probability target, allowing for estimation of small lower failure probability bound.

In this work, Advanced Sampling methods have gone beyond the implementation of Line Sampling. An Advanced Sampling strategy has been developed in OpenCossan, using the Double Loop approach, to allow for re-sampling from previous simulations during the outer loop optimisation. This increases the confidence of the estimator during the optimisation, as a new simulation starts with a more accurate initial important direction. Moreover, an advanced Monte Carlo strategy, derived from the concept of forced simulation, has been developed to estimate time-variant failure probabilities conditional to the inspection outcomes. This strategy has allowed the implementation in OpenCossan of a reliability-based optimisation for the scheduling of multiple inspections of a damage-prone structural component. The combination of the strategy with Random Sets has led to the design of robust maintenance schedules, where imprecision has been systematically included in the optimisation process.

The capabilities and limitations of the presented uncertainty quantification tools have been shown in the NASA Langley UQ Challenge. The efficiency of the proposed methods have been put to the test on a "Black Box" non-linear system response function. The results, obtained with OpenCossan for the solution of the challenge problems, are

encouraging, but some limitations, such as difficulty in interpreting non-linear high-dimensional responses and vast running time, are still to be resolved.

9.2 Recommendations

The efficiency and generality of the developed methods are very promising, and have been well received by the academic community, via conference presentations and journal articles. Uncertainty quantification represents the fundamental tool for risk analysis in any area of engineering applications. Beyond the philosophical digressions, aimed at identifying the most appropriate mathematical framework, this doctoral study has been oriented to provide a practical answer to the need for quantifying the uncertainty in all its complexity. Until now, Imprecise Probability appears to be the most general theory to quantify such uncertainty, as it can be used to describe a vast range of different situations; for example in decision theory, game theory, financial maths, risk, reliability and availability analysis, model updating, surrogate modelling, reliability-based optimisation, non-stationary stochastic processes, power spectra estimations, and many more. Imprecise Probability extends the notion of classical probability to include set-valued descriptors. However, applications of Imprecise Probability to real-scale engineering problems, so far, has been possible only in very limited cases. Among the reasons for this, the efficiency is certainly predominant. In the doctoral study, the use of Advanced Sampling techniques has allowed surmounting this issue, thus linking Imprecise Probability ever closer to the community of practitioners.

A novel and progressive step towards the systematic use of general uncertainty quantification has been made by integrating the presented methods in an existing open suite. The integration of the developed methods in the general framework for risk analysis and uncertainty quantification, OpenCossan, significantly widens the spectrum of potential applications. In OpenCossan, a collection of predefined scripts and solution sequences is available to facilitate connecting the new methods to real-scale problems. This makes the developments presented in this thesis of huge impact on future research.

Future directions lead towards the identification of opportunities for applying these developments to a large number of applications in different areas of research. This will not only facilitate the spread and adoption of tools for general uncertainty quantification, which benefits both academia and industry, but will also increase the confidence of practitioners in using Imprecise Probability. Therefore, this research can seek to serve as a means to promote the use of novel numerical methods for general uncertainty quantification, recently developed in the research community, as a practical tool for engineering analyses.

Bibliography

[1] http://cossan.co.uk/software/open-cossan-engine.php. *The OpenCossan Engine, Website.*

[2] https://en.wikipedia.org/wiki/yield_surface#tresca_yield_surface. *Wikipedia the Free Encyclopedia*, 2015.

[3] D.A. Alvarez. On the calculation of the bounds of probability of events using infinite random sets. *International Journal of Approximate Reasoning*, 43:241–267, 2006.

[4] D.A. Alvarez. *Infinite random sets and applications in uncertainty analysis.* PhD thesis, Innsbruck, Austria, 2007. Available at `https://sites.google.com/site/diegoandresalvarezmarin/RSthesis.pdf`.

[5] D.A. Alvarez. A Monte Carlo-based method for the estimation of lower and upper probabilities of events using infinite random sets of indexable type. *Fuzzy Sets and Systems*, 160:384–401, 2009.

[6] Hurtado J. E. Alvarez, D.A. and F. Uribe. Estimation of the lower and upper probabilities of failure using random sets and subset simulation. In *Vulnerability, Uncertainty, and Risk: Quantification, Mitigation, and Management*, pages 905–914. ASCE, 2014.

[7] J. Arora (Ed.). *Optimization of Structural and Mechanical Systems.* World Scientific, 2007.

[8] S.-K. Au and J. L. Beck. A new adaptive importance sampling scheme for reliability calculations. *Structural Safety*, 21(2):135–158, 1999.

[9] S.-K. Au and J. L. Beck. Estimation of small failure probabilities in high dimensions by subset simulation. *Probabilistic Engineering Mechanics*, 16(4):263–277, 2001.

[10] Efron B. and R.J. Tibshirani. *An Introduction to the Bootstrap.* Chapman & Hall, New York, 1993.

[11] S. Barber, J. Voss and M. Webster The rate of convergence for approximate bayesian computation. *Electronic Journal of Statistics* 80-105, 2015.

[12] J.L. Beck and L. S. Katafygiotis. Updating models and their uncertainties. i: Bayesian statistical framework. *Journal of Engineering Mechanics, ASCE*, 124(4):455–461, 1998.

[13] Y. Ben-Haim. A non-probabilistic concept of reliability. *Structural Safety*, 14(4):227–245, 1994.

[14] Y. Ben-Haim. A non-probabilistic measure of reliability of linear systems based on expansion of convex models. *Structural Safety*, 17(2):91–109, 1995.

[15] K. Breitung. Asymptotic approximations for multinormal integrals. *Journal of Engineering Mechanics*, 110(3):357–366, 1984.

[16] Chiachio, M., J. Beck, J. Chiachio and G. Rus. Approximate bayesian computation by subset simulation. *SIAM Journal on Scientific Computing* 36.3: A1339-A1358, 2014.

[17] J. Ching and Y. Chen. Transitional markov chain monte carlo method for bayesian model updating, model class selection, and model averaging. *Journal of Engineering Mechanics*, 133(7):816–832, 2007.

[18] F.P.A. Coolen and L.V. Utkin. Imprecise reliability: A concise overview. *Risk, reliability and societal safety*, pages 1959–1966, 2007.

[19] F.P.A. Coolen and L.V. Utkin. Imprecise reliability. In *International Encyclopedia of Statistical Science*, pages 649–650. Springer, 2011.

[20] L.G. Crespo, S.P. Kenny and D.P. Giesy. The nasa langley multidisciplinarty uncertainty quantification challenge, 2013.

[21] de Angelis, M., E. Patelli and M. Beer. Advanced line sampling for efficient robust reliability analysis. *Structural safety*, 2014.

[22] B. De Finetti. Theory of probability. a critical introductory treatment. 1979.

[23] A.P. Dempster. Upper and lower probabilities induced by a multivalued mapping. *Annals of Mathematical Statistics*, 38:325–339, 1967.

[24] A. Der Kiureghian. Analysis of structural reliability under parameter uncertainties. *Probabilistic engineering mechanics*, 23(4):351–358, 2008.

[25] A. Der Kiureghian and O. Ditlevsen. Aleatory or epistemic? Does it matter? *Structural Safety*, 31(2):105–112, 2009.

[26] Ditlevsen O., P. Bjerager, R. Olesen and A.M. Hasofer. Directional simulation in Gaussian processes. *Probabilistic Engineering Mechanics*, 3(4):207–217, 1988.

[27] D. Dubois and H. Prade. *Possibility Theory*. Plenum Press, New York, 1988.

[28] D. Dubois and H. Prade. Random sets and fuzzy interval analysis. *Fuzzy Sets and Systems*, 42(1):87–101, 1991.

[29] S. Ferson, V. Kreinovich L. Ginzburg D.S. Myers and K. Sentz. Constructing probability boxes and Dempster-Shafer structures. Report SAND2002-4015, Sandia National Laboratories, Albuquerque, NM, January 2003. Available at `http://www.ramas.com/unabridged.zip`.

[30] A.M. Freudenthal and M. Shinozuka. Structural safety under conditions of ultimate load failure and fatigue. Technical report, DTIC Document, 1961.

[31] D.E. Goldberg et al. *Genetic algorithms in search, optimization, and machine learning*, volume 412. Addison-wesley Reading Menlo Park, 1989.

[32] H.A. Jensen. Reliability-based optimization of uncertain systems in structural dynamics. *AIAA journal*, 40(4):731–738, 2002.

[33] C. Kai-Yuan. Fuzzy reliability theories. *Fuzzy Sets and Systems*, 40(3):510–511, 1991.

[34] G.J. Klir. *Uncertainty and Information : Foundations of Generalized Information Theory*. John Wiley and Sons, New Jersey, 2006.

[35] A. Kolmogorov. Sulla determinazione empirica di una legge di distribuzione (in italian). *Giornale dell'Istituto Italiano degli Attuari*, 4:83–91, 1933.

[36] P.S. Koutsourelakis, H.J. Pradlwarter and G.I. Schuëller. Reliability of structures in high dimensions, part i: algorithms and applications. *Probabilistic Engineering Mechanics*, 19(4):409–417, 2004.

[37] M. Lukic and C. Cremona. Probabilistic assessment of welded joints versus fatigue and fracture. *Journal of Structural Engineering*, 127(2):211–218, 2001.

[38] R.E. Melchers. Importance sampling in structural systems. *Structural safety*, 6(1):3–10, 1989.

[39] N. Metropolis and S. Ulam. The monte carlo method. *Journal of the American statistical association*, 44(247):335–341, 1949.

[40] D. Moens and D. Vandepitte. A survey of non-probabilistic uncertainty treatment in finite element analysis. *Computer methods in applied mechanics and engineering*, 194(12):1527–1555, 2005.

[41] B. Möller, W. Graf and M. Beer. Fuzzy structural analysis using α-level optimization. *Computational Mechanics*, 26(6):547–565, 2000.

[42] R.E. Moore. *Interval analysis*, volume 4. Prentice-Hall Englewood Cliffs, 1966.

[43] R.E. Moore, R.B. Kearfott, and M.J. Cloud. *Introduction to Interval Analysis*. Society for Industrial and Applied Mathematics, Philadelphia, PA, USA, 2009.

[44] F. Mosteller. A k-sample slippage test for an extreme population. *Annals of Mathematical Statistics*, 19(1):58–65, 1948.

[45] NASA. Standard for models and simulations. Technical Report NASA-STD-7009, National Aeronautics and Space Administration (NASA), 2013.

[46] R.B. Nelsen. *An introduction to copulas*. Springer Series in Statistics. Springer, New York, 2 edition, 2010.

[47] M. Oberguggenberger and W. Fellin. Assessing the sensitivity of failure probabilities: a random set approach. *Safety and reliability of engineering systems and structures, ICOSSAR*, pages 1755–1760, 2005.

[48] P.C. Paris and F. Erdogan. A critical analysis of crack propagation laws. *Journal of Fluids Engineering*, 85(4):528–533, 1963.

[49] E. Patelli, D.A. Alvarez M. Broggi and M. de Angelis. An integrated and efficient numerical framework for uncertainty quantification: application to the nasa langley multidisciplinary uncertainty quantification challenge. In *16th AIAA Non-Deterministic Approaches Conference (SciTech 2014)*, AIAA SciTech. American Institute of Aeronautics and Astronautics, 2014.

[50] E. Patelli, D.A. Alvarez M. Broggi and M. de Angelis Uncertainty management in multidisciplinary design of critical safety systems. *Journal of Aerospace Information Systems*, pages 1–30, 2014.

[51] E. Patelli and H.J. Pradlwarter. Monte carlo gradient estimation in high dimensions. *International journal for numerical methods in engineering*, 81(2):172–188, 2010.

[52] H.J. Pradlwarter Patelli, E. and G.I. Schuëller. On multinormal integrals by importance sampling for parallel system reliability. *Structural Safety*, 33(1):1–7, 2011.

[53] E. Patelli, H.M.Panayirci, M. Broggi, B. Goller, P. Beaurepaire and H. J. Pradlwarter and G. I. Schuëller. General purpose software for efficient uncertainty management of large finite element models. *Finite Elements in Analysis and Design*, 51:31–48, 2012.

[54] E. Patelli, M. Broggi, M. de Angelis and M. Beer. OpenCossan: An efficient open tool for dealing with epistemic and aleatory uncertainties. In Ivan S.K. Au & Jim W. Hall Michael Beer, editor, *Vulnerability, Uncertainty, and Risk: Analysis, Modeling, and Management*. American Society of Civil Engineers, 2014.

[55] M.A. Valdebenito Patelli, E. and G.I. Schuëller. General purpose stochastic analysis software for optimal maintenance scheduling: application to a fatigue-prone structural component. *International Journal of Reliability and Safety*, 5(3):211–228, 2011.

[56] M. J.D. Powell. The bobyqa algorithm for bound constrained optimization without derivatives. *Cambridge NA Report NA2009/06 (2009), University of Cambridge, Cambridge*, 2009.

[57] H.J. Pradlwarter and G.I. Schuëller. The use of kernel densities and confidence intervals to cope with insufficient data in validation experiments. *Computer Methods in Applied Mechanics and Engineering*, 197(29-32):2550–2560, 2008.

[58] L. J. Savage. *The foundations of statistics*. Courier Corporation, 1972.

[59] J.J. Schneider and S. Kirkpatrick. *Stochastic optimization*. Springer, 2006.

[60] G.I. Schuëller. Efficient monte carlo simulation procedures in structural uncertainty and reliability analysis - recent advances. *Journal of Structural Engineering and Mechanics*, 32:1–20, 2009.

[61] G.I. Schuëller and H.J. Pradlwarter. Benchmark study on reliability estimation in higher dimensions of structural systems–an overview. *Structural Safety*, 29(3):167–182, 2007.

[62] P.S. Koutsourelakis, H.J. Pradlwarter and G.I. Schuëller. A critical appraisal of reliability estimation procedures for high dimensions. *Probabilistic Engineering Mechanics*, 19(4):463–474, 2004.

[63] K. Sentz and S. Ferson. *Combination of evidence in Dempster-Shafer theory*, volume 4015. Citeseer, 2002.

[64] G. Shafer. *A Mathematical Theory of Evidence*. Princeton University Press, Princeton, 1976.

[65] M. Shinozuka. Basic analysis of structural safety. *Journal of Structural Engineering*, 109(3):721–740, 1983.

[66] B.W. Silverman. *Density Estimation for Statistics and Data Analysis*. Chapman & Hall/CRC, 1998.

[67] F. Tonon. Using random set theory to propagate epistemic uncertainty through a mechanical system. *Reliability Engineering & System Safety*, 85(1):169–181, 2004.

[68] L.V. Utkin and F.P.A. Coolen. Imprecise reliability: an introductory overview. In *Computational intelligence in reliability engineering*, pages 261–306. Springer, 2007.

[69] M.A. Valdebenito, H.J. Pradlwarter, and G.I. Schuëller. The role of the design point for calculating failure probabilities in view of dimensionality and structural nonlinearities. *Structural Safety*, 32(2):101–111, 2010.

[70] M.A. Valdebenito and G.I. Schuëller. Design of maintenance schedules for fatigue-prone metallic components using reliability-based optimization. *Computer Methods in Applied Mechanics and Engineering*, 199(33):2305–2318, 2010.

[71] M.A. Valdebenito and G.I. Schuëller. A survey on approaches for reliability-based optimization. *Structural and Multidisciplinary Optimization*, 42(5):645–663, 2010.

[72] P. Walley. *Statistical reasoning with imprecise probabilities*, volume 42. Peter Walley, 1991.

[73] K. Weichselberger. The theory of interval-probability as a unifying concept for uncertainty. *International Journal of Approximate Reasoning*, 24(2):149–170, 2000.

[74] D. Weimin and H. C. Shah. Vertex method for computing functions of fuzzy variables. *Fuzzy Sets and Systems*, 24(1):65 – 78, 1987.

[75] S.J. Wright and J. Nocedal. *Numerical optimization*, volume 2. Springer New York, 1999.

[76] L.A. Zadeh. Fuzzy sets. *Information and control*, 8(3):338–353, 1965.

[77] M. Zaffalon. The naive credal classifier. *Journal of statistical planning and inference*, 105(1):5–21, 2002.

[78] H. Zhang, H. Dai, M. Beer and W. Wang. Structural reliability analysis on the basis of small samples: an interval quasi-monte carlo method. *Mechanical Systems and Signal Processing*, 37(1):137–151, 2013.

[79] M.Q. Zhang, M. Beer and C.G. Koh. Interval analysis for system identification of linear mdof structures in the presence of modeling errors. *Journal of Engineering Mechanics*, 138(11):1326–1338, 2012.

[80] R.L. Mullen Zhang, H. and R.L. Muhanna. Interval monte carlo methods for structural reliability. *Structural Safety*, 32(3):183–190, 2010.

[81] R. Zheng and B.R. Ellingwood. Role of non-destructive evaluation in time-dependent reliability analysis. *Structural Safety*, 20(4):325–339, 1998.

[82] E. Zio and M. Marseguerra. Basics of the monte carlo method with application to system reliability. *LiLoLe, Hagen*, 2002.

[83] E. Zio, P. Baraldi and N. Pedroni. Optimal power system generation scheduling by multi-objective genetic algorithms with preferences. *Reliability Engineering & System Safety*, 94(2):432–444, 2009.